Conceptual Design Report
for the
Neutron Electric Dipole Moment Project
(nEDM)

Project MIE #71RE

at
Los Alamos National Laboratory
Los Alamos, New Mexico
managed by
Los Alamos National Security, LLC
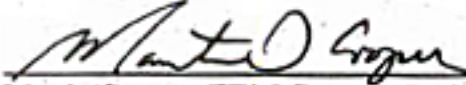
For the U.S. Department of Energy
Office of Science
Office of Nuclear Physics (SC-26)

Date approved:

February 2007
revision 0

Conceptual Design Report
for
A New Search for the Neutron Electric Dipole Moment (EDM)
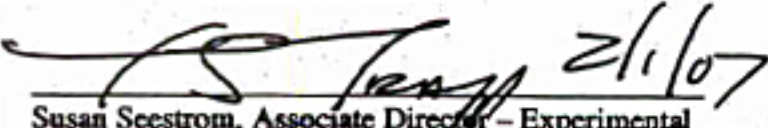
At the Spallation Neutron Source located at
Oak Ridge National Laboratory
Managed by Los Alamos National Laboratory

February, 2007

CONCURRENCES:

Martin Cooper   2/1/2007

Martin Cooper, EDM Contract Project Manager
Los Alamos National Laboratory

Jack Shlachter   2/1/07

Jack Shlachter, Physics Division Leader
Los Alamos National Laboratory

Susan Seestrom   2/1/07

Susan Seestrom, Associate Director – Experimental
Physical Sciences Directorate
Los Alamos National Laboratory

APPROVED:

Eugene Colton   2/1/2007

Eugene Colton, EDM Federal Project Director
Los Alamos Site Office

Terry Wallace   2/1/2007

Terry Wallace, Principal Associate Director for
Science, Technology, and Engineering
Los Alamos National Laboratory

A New Search for
The Neutron Electric Dipole Moment

Conceptual Design Report
submitted to the
The Department of Energy
prepared by
The EDM Collaboration

R. Alarcon, L. Baron-Palos
Arizona State University, Tempe, AZ, USA
D. Budker, A. Sushkov
University of California at Berkeley, Berkeley, CA 94720, USA
R. Carr, B. Filippone, R. McKeown, B. Plaster, R. Schmid
California Institute of Technology, Pasadena, CA 91125, USA
W. Chen, D. Dutta, H. Gao, K. Kramer, X. Qian, Q. Ye, X. F. Zhu, X. Zong
Duke University, Durham NC 27708, USA
F. Mezei
Hahn-Meitner Institut, D-14109 Berlin, Germany
C.-Y. Liu, J. Long, H.-O. Meyer, M. Snow
Indiana University, Bloomington, IN 47405, USA
D. Beck, A. Esler, D. Hertzog, P. Kammel, J.-C. Peng, S. Williamson, J. Yoder
University of Illinois, Urbana-Champaign, IL 61801, USA
W. Korsch
University of Kentucky, Lexington KY 40506, USA
P. Barnes, J. Boissevain, <u>M. Cooper</u>, M. Espy, T. Ito, A. Matlachov, W. Sondheim, J. Torgerson,
S. Wilburn
Los Alamos National Laboratory, Los Alamos, NM 87545, USA
K. Dow, D. Hassel, E. Ihloff, J. Kelsey, R. Milner, R. Redwine
Massachusetts Institute of Technology, Cambridge, MA 02139, USA
F. Dubose, R. Golub, C. Gould, D. Haase, P. Huffman, E. Korobkina, C. Swank, A. Young
North Carolina State University, Raleigh, NC 27695, USA
V. Cianciolo, S. Penttila
Oak Ridge National Laboratory, Oak Ridge, TN 37831, USA
M. Hayden
Simon-Fraser University, Burnaby, BC, Canada V5A 1S6
C. Crawford, G. Greene
The University of Tennessee, Knoxville, TN 37996, USA
<u>S. Lamoreaux</u>, D. McKinsey
Yale University, New Haven, CT 06520, USA

February 2007

A New Search for the Neutron Electric Dipole Moment

Contents

A New Search for the Neutron Electric Dipole Moment

Summary

The possible existence of a nonzero electric dipole moment (EDM) of the neutron is of great fundamental interest in itself and directly impacts our understanding of the nature of electro-weak and strong interactions. The experimental search for this moment has the potential to reveal new sources of time reversal (*T*) and charge conservation and parity (*CP*) violation and to challenge calculations that propose extensions to the Standard Model. In addition, the small value for the neutron EDM continues to raise the issue of why the strength of the *CP*-violating terms in the strong Lagrangian are so small. This result seems to suggest the existence of a new fundamental symmetry that blocks the strong *CP*-violating processes.

The goal of the current experiment is to significantly improve the measurement sensitivity to the neutron EDM over what is reported in the literature. The experiment has the potential to

a) measure the magnitude of the neutron EDM or
b) lower the current experimental limit by one to two orders of magnitude.

Achieving these objectives will have major impact on our understanding of the physics of both weak and strong interactions.

The experiment is based on the magnetic-resonance technique of rotating a magnetic dipole moment in a magnetic field. Polarized neutrons and polarized ^{3}He atoms coexist in a bath of superfluid ^{4}He at a temperature of ~500 mK. When placed in an external magnetic field, both the neutron and ^{3}He magnetic dipoles precess in the plane perpendicular to the magnetic field. The measurement of the neutron EDM comes from a measurement of the difference in the precession frequencies of the neutrons and the ^{3}He atoms when a strong electric field parallel to the magnetic field is reversed. In this comparison measurement, the neutral ^{3}He atom is assumed to have a negligible electric dipole moment.

In principle, this new type of EDM experiment can achieve more than two orders of magnitude improvement in the experimental limit for the neutron EDM in conjunction with the Spallation Neutron Source (SNS). This factor results from the possibility of an increased electric field (a factor of ~5) due to the excellent dielectric properties of superfluid ^{4}He, an increase in total number of ultracold neutrons (UCNs) stored (~100 fold improvement that leads to factor of 10 gain in sensitivity) and an increased storage time (~5 times, which produces a factor of 2 in sensitivity) due to the low temperature of the walls. The current experimental EDM bound, however, is nearly limited by magnetic-field systematics. With the proposed experiment, an EDM limit of 10^{-28} e·cm is possible; the use of ^{3}He as a volume comagnetometer is crucial to the elimination of the magnetic-field systematics.

The organization of this conceptual design report (CDR) begins with a brief history of the subject, including the scientific motivation and a status report on other neutron and atomic EDM experiments. This introduction is followed by a high-level description of the experimental technique and includes a discussion of both the sensitivity of the measurement and its systematic limitations. This part also contains the project specification for Critical Decision 4 and for achieving the ultimate sensitivity of the measurement. Demonstrating the feasibility of this new technique involves considerable research and development (R&D), and both previous successes as well as future work to mitigate uncertainties are described. The balance of the CDR contains detailed descriptions of the subsystems identified in the work breakdown structure (WBS) described in the preliminary project execution plan (PPEP).

The CDR is one of a collection of documents prepared for the Critical Decision 1 review. The companion documents include the preliminary hazard analysis, the preliminary acquisition

strategy, the PPEP, and preliminary risk-management plan. These documents are supported by a resource-loaded WBS.

The physics goals of this experiment are timely and of unquestioned importance to modern theories of electroweak and strong interactions. The technique seeks to improve the current EDM limit by a factor of 100.

I.   Scientific Motivation

A. General Introduction

Precision measurements of the properties of the neutron present an opportunity to search for violations of fundamental symmetries and to make critical tests of the validity of the Standard Model (SM) of electroweak (EW) interactions. These experiments have been pursued with great energy and interest since Chadwick [1] discovered the neutron in 1932.

Searches for the electric dipole moment (EDM) of the neutron (nEDM) date back to a 1957 paper of Purcell and Ramsey [2]. This paper led to an experiment using a magnetic-resonance technique at Oak Ridge National Laboratory (ORNL), where they established a value of $d_n = (-0.1 \pm 2.4) \times 10^{-20}$ $e{\cdot}$cm [3]. In the intervening 30 years, a series of measurements of increasing precision have culminated in the current best limit of $d_n < 3 \times 10^{-26}$ $e{\cdot}$cm (90% C.L.) obtained in measurements at the Institute Laue-Langevin (ILL) reactor at Grenoble [4].

The physics motivation for these measurements has been widely discussed. A search for a nonzero value of the nEDM is a search for a violation of time-reversal (*T*) invariance. To date, there is only one measurement (a comparison of neutral *K* and $\overline{K}$ meson decay) in which *T* violation has been seen directly [5]. The asymmetry in these rates is found to be $(6.6 \pm 1.3 \pm 1.0) \times 10^{-3}$ and is consistent with the SM.

The SM prediction for the nEDM is at the 10^{-31} $e{\cdot}$cm level, below the reach of current measurements by six orders of magnitude [6]. The only violation of the SM that has been observed is the recent measurements of the neutrino mass. There are many proposed models of the EW interaction that are extensions beyond the SM and that raise the predicted value of the nEDM by up to seven orders of magnitude. Some of these are already excluded by the current limit on the nEDM. The proposed experiment has the potential to reduce the acceptable range for predictions by two orders of magnitude and to provide a significant challenge to these extensions to the SM. Conversely, if a new source of *T* violation is present in nature, that is relevant to this hadronic system, this experiment offers an intriguing opportunity to measure a nonzero value of the nEDM. Observation of a violation of *T* invariance through measurement of the nEDM would be of fundamental significance.

This project invokes a new technique for searching for the EDM of the neutron which offers unprecedented sensitivity. It is based on the traditional magnetic-resonance technique in which the magnetic dipole moment of a neutron is placed in a plane perpendicular to parallel magnetic and electric field. The magnetic field is quite weak and the electric field is as strong as possible. The impact of the electric field on the precession of the neutron is characterized by the first moment of the neutron charge distribution, d_n, its EDM. All experiments to date have assigned a zero value to the nEDM. There has been an impressive reduction, with time, of the experimental limit for d_n as illustrated in Fig I-1.

The nEDM provides a very sensitive test of the SM. A nEDM measurement, with two orders of magnitude improvement over the current experimental limits, presents an excellent opportunity to challenge the extensions beyond the SM and to search for new physics in nonstrange systems in the *T* sector.
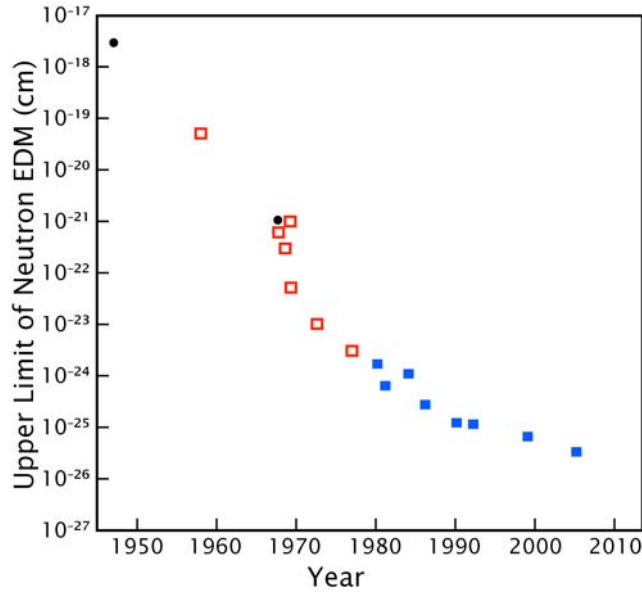
Fig. I-1.   Upper limits of nEDM plotted as a function of year of publication. The solid circles correspond to neutron-scattering experiments. The open squares represent in-flight magnetic-resonance measurements, and the solid squares signify ultracold neutron (UCN) magnetic-resonance experiments.

B. Theoretical Motivation

The search for a nEDM, d_n, aims to discover new physics in the *CP* violating sector. A focus on *CP* violation is suggested by the critical importance which this symmetry has assumed in constructing theories of modern particle physics. More broadly, it acknowledges the importance of *CP* violation in shaping our understanding of the origins and evolution of the universe. In particular, explaining the origin of the baryonic matter of the universe is an important goal for nuclear physics [7]. While the *CP* violation present in the SM suffices to explain what has been observed in the kaon and *B* meson systems, it is not sufficient to explain the small excess of baryons over antibaryons in the present universe. This new measurement of d_n—with its substantially greater sensitivity to new *CP* violation—provides a powerful tool in this quest.

The role of symmetry, including the observed breaking of the discrete symmetries of parity *P* and *CP*, has been particularly significant for the construction of the SM. Parity violation, which has been measured in many systems, is well represented in the SM through a definitive chiral *V-A* coupling of fermions to gauge bosons. The information available on *CP* violation, while much more limited, has had a profound impact. Indeed, the decay of neutral kaons anticipated the three-generation structure of the SM as we now know it.

Although the deeper reasons for the *P* and *CP* violation of the SM have yet to be understood, *CP* violation is arguably the more mysterious of the two. It occurs in two places within the model: as a complex phase in the Cabibbo-Kobayashi-Maskawa (CKM) matrix that characterizes charge changing weak interactions of quarks, and as total derivative in the SU(3)$_C$ Lagrangian that does not vanish because of the topology of the vacuum. The *CP* violation observed in the neutral kaon system and in the decays of *B* mesons is consistent with the presence of the phase factor. On the other hand, present limits on d_n and the ^{199}Hg EDM imply that the coefficient of the *CP* violating term in the strong Lagrangian is exceedingly small. In

neither case does the strength of the associated *CP* violation allow us to explain the observed abundance of baryonic matter over antimatter. Thus, searching for new sources of *CP* violation has become an attractive focus in the quest for new physics.

The observation of *CP* violation implies time-reversal symmetry *T* violation (and vice versa) through the *CPT* theorem. This theorem asserts that field theories with local, Lorentz invariant and hermitian Lagrangians must be invariant under the combined transformation *C*, *P*, and *T*. In the absence of degeneracy, the energy of a spin-½ particle, e.g., a neutron, in an electric field *E* is related to d_n by $E_n = d_n\boldsymbol{\sigma} \cdot \mathbf{E}$ where σ is its Pauli spin matrix. Because this expression is odd under *T* (and *P*), measuring a nonvanishing d_n is also a unique signature for *CP* violation. The same arguments apply to the electron EDM, d_e,—whose value is determined from measurements of the EDM of paramagnetic systems, i.e., those having unpaired electrons, such as atomic thallium—and to the EDM of diamagnetic atoms such as ^{199}Hg or ^{129}Xe.

Importantly, the EDMs of each of these systems carry a complementary dependence on the *CP* violating parameters of a given new physics model. For example, d_e is quite insensitive to *CP* violation in the strong sector, making systems with quarks the only viable probe of strong *CP* violation. In contrast, the neutron, lepton, and neutral-atom EDMs generally depend differently on the complex phases entering any new EW *CP* violation. Consequently, it is essential to carry out measurements in a variety of systems in order to provide the most comprehensive probe. Moreover, if a nonzero EDM is observed, then it will require complementary EDM measurements to discern the source of the new *CP* violation among the many possibilities. In this respect, the time is ripe for a new d_n search with significantly greater sensitivity, as complementary efforts are currently underway for d_e and neutral-atom EDMs.

CP Violation and the Baryon Asymmetry of the Universe

One of the outstanding puzzles of physics is the fact that the universe contains any baryonic matter at all. Indeed, if the universe were matter-antimatter symmetric at its birth, then one might expect the matter and antimatter in the universe should balance out in the present universe. The departure from this expectation is characterized by the baryon asymmetry, $\Delta n_{Bar}/(n_{\mathrm{Bar}} + n_{\overline{Bar}})$, where $\Delta n_{Bar} = n_{Bar} - n_{\overline{\mathrm{Bar}}}$ is the difference in the abundances of baryons and antibaryons. It is conventional to quantify this asymmetry in terms of the number of baryons in the universe today, $n_{Bar}|_{today}$, and the number of photons in the cosmic background n_γ. One observes that the ratio $r_{Bar} \equiv n_{Bar}|_{today}/n_\gamma$ is just a few 10^{-10}, *i.e.*, that the universe is strikingly dilute, containing just a single baryon for every 10^9 or so photons.

Of course, n_{Bar} changes over time. During an earlier epoch, when the temperature of the universe was above the threshold for production of nucleons and antinucleons ($T \sim 10^{13}$ K), both species were plentiful and were in thermal equilibrium with the photons. The photon number, n_γ, is roughly constant in time [8]. At that time, $\Delta n_{Bar} \approx n_{Bar}|_{today}$ [8]. The baryon asymmetry of the universe (BAU) at this earlier epoch is therefore approximately equal to the value of r_{Bar},

$$\frac{\Delta n_{Bar}}{n_{Bar} + n_{\overline{Bar}}} = r_{Bar} \gg \text{few} \times 10^{-10}. \tag{I.1}$$

The basic question is: how could this BAU result from physical processes happening since the birth of the universe in the Big Bang some $\tau_U \sim 10^{10}$ years ago?

In a seminal paper, A. Sakharov [9] identified three ingredients that would have to have been present in the particle physics of the early universe in order to account for the BAU:
(1) reactions that change baryon number have to occur;
(2) these reactions must be both *C* and *CP* violating; and
(3) they must occur in nonequilibrium processes.

Attempts to understand the BAU from this point of view—known as baryogenesis—have focused on several eras of cosmic evolution:

(1) One—the era of grand unified theory (GUT) baryogenesis—occurred when the temperature of the universe was $T \approx 10^{29}$ K, corresponding to an energy scale $M_x \approx 10^{16}$ GeV. If the forces of nature were unified at the beginning of cosmic evolution, then it is believed that the unification of the strong and EW interactions would have begun to break down at this time. In this scenario, the BAU is produced in tandem when the symmetry group for grand unification was spontaneously broken.

(2) At the other extreme, baryogenesis could have occurred during the era of EW symmetry breaking when it is thought that the particles of the SM became massive. This era corresponds to $T \approx 10^{15}$ K or energies of about 100 GeV comparable to the mass of a *W* or *Z* gauge boson. We discuss this possibility of EW baryogenesis (EWB) [10] in more detail below.

(3) A third possibility involves neutrinos in the early universe. If at some temperature, well above the EW phase transition, an excess of leptons over antileptons is generated, topological processes that conserve baryon minus lepton number, can communicate this asymmetry to the baryon sector [11]. This scenario—known as leptogenesis—has seen considerable interest recently, generated by the observation of neutrino oscillations. The most natural explanation for the nonvanishing, but tiny, neutrino mass implied by these oscillations is the existence of a heavy, Majorana neutrino that mixes with Dirac neutrinos to generate small masses via the seesaw mechanism. Because Majorana neutrinos are their own antiparticles, their interactions violate total lepton number. Thus, out-of-equilibrium decays of the heavy Majorana neutrinos in the early universe could have created the lepton asymmetry needed for the BAU—provided there exists new *CP*-violation in the lepton sector.

While all three of these possibilities are theoretically attractive, only the second option—EWB—can be tested and (in principle) ruled out experimentally. Generally speaking, the mass scales associated with particles in GUT baryogenesis and leptogenesis are too large to make their effects discernible to experiment. Moreover, the *CP* violation associated with these heavy particles need not be manifest at low energy. For example, the analog of the phase factor $e^{i\delta_{CKM}}$ that arises in the mixing matrix for the light neutrinos could be identically zero, even if the *CP* violating phases needed for leptogenesis processes at high energies were large enough to explain the BAU. Observation of a *CP* violation in the light neutrino sector would provide indirect evidence for the viability of leptogenesis. In contrast, EWB involves new particles with masses of order the EW scale, and the connection between the *CP* violating interactions of these particles and the *CP* violation needed to explain the BAU is more direct than in the high scale baryogenesis alternatives. Thus, EDM searches—at the level of sensitivity expected for this nEDM experiment—are poised to discover this new electroweak *CP* violation if EWB is responsible for the BAU.

Theoretically, EWB has seen a resurgence of scrutiny recently after the first generation of studies in the 1980s and 90s. During that time, Shaposhnikov [12] analyzed EWB in the SM and showed that—while the SM contains all of Sakharov's ingredients—they are not sufficiently effective to account for the BAU. In the SM and other non-Abelian gauge theories there exist multiple and topologically distinct vacuum states distinguished by their baryon number and lepton number. Although baryon current conservation strictly forbids transitions among states of different baryon number states at the classical level, one finds quantum mechanically that the divergence of the baryon current is subject to triangle anomalies that signify symmetries broken at a quantum mechanical level. Thus, baryon-number-violating transitions are no longer

forbidden, and the corresponding probability may be expressed in terms of instanton-like gauge field configurations [13] called sphalerons. This probability is extremely small for $T \approx 0$ as in the universe today where the proton lifetime $\tau_p > 10^{32}$ yr $>> \tau_U$; however, when the temperature is greater than $\sim 10^{17}$ K, sphalerons are easily excited, and anomalous baryon number violation is extremely rapid [14]. In this way, the first Sakharov condition is satisfied in the SM. The second Sakharov condition is satisfied in the SM through the explicit *CP*-violation present in the CKM matrix. Finally, if conditions of supercooling prevail at EW-scale temperatures, then the third Sakharov condition is satisfied in the first-order transition, occurring as droplets of the broken phase begin to nucleate out. Supercooling refers to the situation where the universe cools through expansion beyond the point at which a phase change would already have occurred under equilibrium conditions.

However, Shaposhnikov [12] was unable to describe r_{Bar} quantitatively in the SM. The SM has two shortcomings. First, the SM *CP*-violating effects are highly suppressed by the small mixing angles of the CKM matrix and light fermion Yukawa couplings. As a result, the largest BAU that might be created via SM processes is many orders of magnitude too small. Second, it is now believed that a single Higgs doublet as incorporated into the SM would not support a first-order electroweak phase transition because a single Higgs doublet with mass, $M_H > 70$ GeV is known, from lattice gauge calculations [15], to be insufficient for supercooling, and at the same time LEP measurements imply that M_H exceeds 114.4 GeV. Clearly, new physics beyond the SM, including new sources of *CP* violation that may lead to a measurable value for d_n, must exist if the observed BAU arises from EW baryogenesis.

One such source might be found in the supersymmetric extensions of the SM. It has been shown recently [16,17,18,19,20,21,22,23,24] that small values of the *CP* violating phases (consistent with constraints from d_n) can provide values of r_{Bar} comparable to the empirical value given in Equation I.1. In many SUSY models, both the BAU and the EDMs of elementary fermions depend on two CP violating phases: ϕ_μ and ϕ_A. The baryon asymmetry is then given by

$$r_{Bar} = F_1 \sin\phi_m + F_2 \sin(\phi_m + \phi_A) \tag{I.2}$$

where $F_{1,2}$ are functions of the other supersymmetric parameters. For suitable choices of these parameters, the production of baryon number can be enhanced through resonant scattering of superpartners from the spacetime-varying Higgs vacuum-expectation values during the phase transition. Near the peaks of these resonances, a sufficiently large BAU can be produced for values of the *CP* violating phase $\phi_\mu \sim$ few times 10^{-2}; precision EW data prevent the F_2 term from becoming resonantly enhanced.

The presence of $O(10^{-2})$ phases is marginally compatible with present EDM limits and one-loop contributions from superpartners. An illustration is shown in Figure I-2, where the constraints on the phases ϕ_μ and ϕ_A from present d_e and d_n limits are shown for representative choices of SUSY mass parameters [21]. The colored band indicates the region needed to produce the BAU. Figure I-2 illustrates both the complementarity of the neutron and electron EDM measurements for this particular scenario as a probe of new *CP* violation. Moreover, the impact of improved precision is clear. As the sensitivity of the measurements is increased by two orders of magnitude, the width of the EDM bands will shrink by similar factors, as the EDMs depend linearly on the *CP* violating phases. If resonant superesymmetric EWB is responsible for the production of the BAU, then future measurements should discover a nonvanishing EDM. Conversely, the absence of a signal would rule out this particular scenario.

It is important to bear in mind that Figure I-2 applies to one particular SUSY scenario, and that the dependence of both EDMs and the BAU on *CP*-violating phases in other scenarios can be considerably more complex. In versions of SUSY with an extended Higgs sector, for example, resonant enhancements of F_2 may be allowed, leading to a stronger dependence on the

phase ϕ_A. In this case, exploiting the complementary dependence of d_e and d_n on the *CP*-violating phases would be crucial to probing such a scenario. Considerable theoretical work remains to be undertaken to study *CP*-violation and baryogenesis in this broader class of models, and the new EDM measurements provide theorists with strong motivation to carry out this analysis.
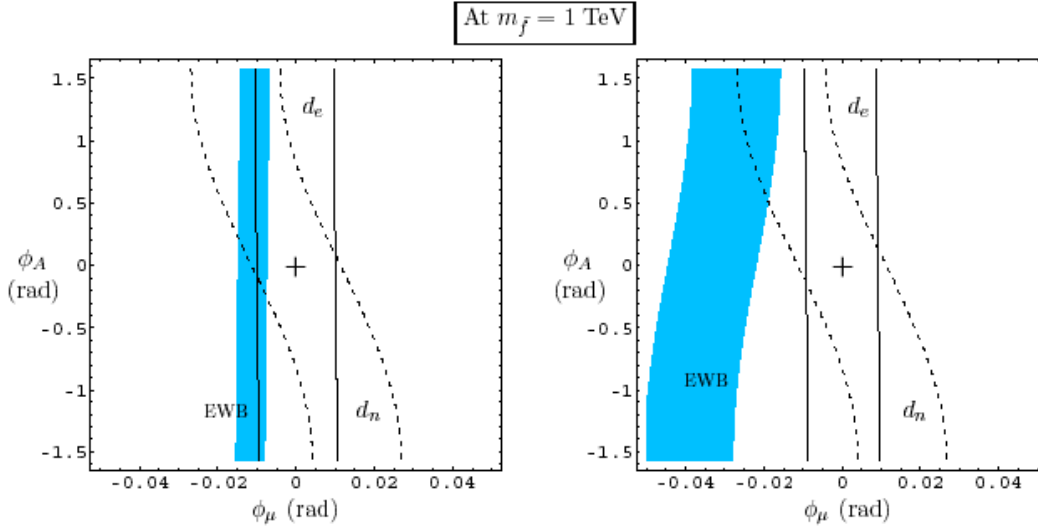
Fig. I-2.   The role of d_n and d_e in determining the phases of EWB for representative parameter choices in the supersymmetric theory. The blue band is the choice of parameters to explain EWB. The dotted band is the limit for d_n and the solid band is the limit from d_e. The plots represent two different choices of SUSY mass parameters.

The one-loop EDM constraints on SUSY *CP* violation can be evaded if some of the supersymmetric particles are sufficiently heavy. Recently, there has been considerable interest in a variant on SUSY known as "split supersymmetry"—wherein the masses of the fermion superpartners are quite large (of order 10 TeV or more) while the masses of the gauge and Higgs boson superpartners that make up charginos and neutralinos remain of order the EW scale. In this scenario, the EDMs of the neutron and electron arise at two-loop order, and the constraints on the *CP* violating phases are more relaxed. In particular, phases of O(1) are not presently ruled out for split SUSY, and there exists considerable latitude for resonant EW baryogenesis to produce the BAU.

The impact of present and future EDM measurements on the viability of this scenario is illustrated in Figure I-3 (see Reference [24]), where the constraints are shown on SUSY mass parameters obtained by effective baryogenesis, LEP 2 direct-search bounds, and two-loop electron EDM limits (the implications of d_n are similar). The parameters μ and M_1 govern the masses of the Higgs and guage boson superpartners, respectively. The light-blue bands give the region required by resonant EWB for $\sin\phi_\mu$ =0.1. The red region is excluded by LEP2. The region below the dark-blue line is ruled out by present bounds on d_e. The remaining bands indicate the prospective reaches for future experimental d_e probes (similar to those for the neutron). Again, as in the case of the conventional SUSY scenario, future EDM measurements have the potential to exclude resonant SUSY baryogenesis if an EDM of order 10^{-28} e·cm or larger is not discovered. It should be noted that the precise bands associated with nEDM measurements are not shown, as there exist differences in the literature over the relative signs of various two-loop contributions. Theorists are addressing these disagreements—motivated in part

by the new d_n measurement discussed here. Nevertheless, the overall order of magnitude sensitivities of the electron and neutron EDM measurements to two-loop effects are comparable.
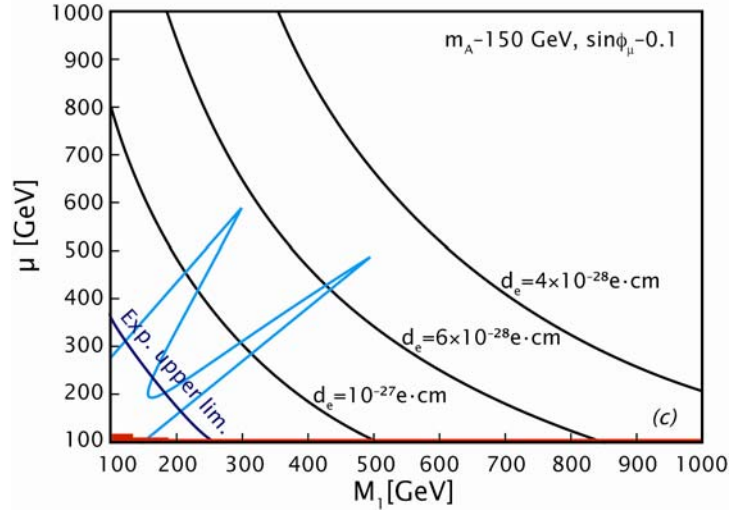
Fig I-3.   The allowed space for the Higgs and *W* boson superpartners for a particular SUSY model. The allowed band is to the upper right of the limits on d_e (solid lines) and LEP 2 direct searches (dark blue). The values required for EWB with $\sin\phi_\mu = 0.1$ are toward the origin (light blue).

In short, the nEDM experiment proposed here, together with other concurrent EDM measurements on complementary systems, will be a powerful probe of cosmology. One might ask how robust this probe will be during the era of studies at the Large Hadron Collider (LHC). To address this question, Figure I-4 shows the reach of various collider studies into the parameters space shown in Figure I-3. The light blue and red bands are as in Figure I-3. The grey region is excluded by the requirement that the lightest supersymmetric particle (LSP) be a neutralino and, thus, a candidate for cold dark matter. The prospective reach of the LHC is indicated by the green lines and arrows, while the possible reach of a future linear collider is given by the blue curves. As one can see, the LHC will probe some—but not all—of the parameter space relevant to baryogenesis in this scenario, even if one requires the neutralino to be the LSP. Indeed, the lower portion of the light blue bands could still be allowed and imply observable EDMs after completion of LHC running.

Strong CP

As noted above, the SM contains two sources of *CP* violation. In the EW sector it appears through δ_{CKM}. The other is a term in the QCD Lagrangian itself, the so-called θ-term,

$$L_{\text{QCD}} = L_{CP} + \frac{\bar{\theta}g_s^2}{32\pi^2}G_{\mu\nu}\tilde{G}^{\mu\nu}, \tag{I.3}$$

which explicitly violates *CP* symmetry because of the appearance of the product of the gluonic field operator *G* and its dual $\tilde{G}$. Because *G* couples to quarks but does not induce flavor change, d_n is much more sensitive to θ than it is to δ_{CKM}; additionally, the θ-term is practically irrelevant to d_e and kaon decays. Thus, measurement of d_n would uniquely determine an important parameter of the SM. Calculations [25,26] have shown that $d_n \sim \text{O}(10^{-16}\theta)$ *e*·cm.
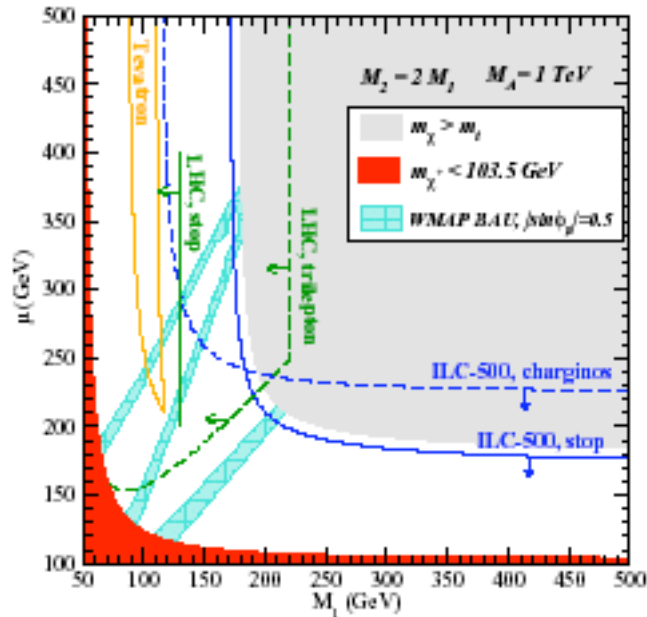
Fig. I-4. Physics reach of present and future collider studies relevant to SUSY baryogenesis. The light-blue and red regions are as in Figure I-3. Yellow lines indicate prospective sensitivity of Tevatron studies. Green lines indicate parameter space accessible to LHC measurements. The reach of a 500 GeV ILC is shown by the blue lines.

Although the value of the strength θ is unknown, the observed limit on d_n implies that $\theta < 10^{-9\pm1}$ [27]. A comparable limit on θ comes from the EDM of the mercury atom. However, the natural scale apparent in Equation I.3 suggests rather that $\theta \sim O(1)$. The extreme smallness of θ (The so-called strong *CP* problem) begs for an explanation. One attempt [Reference 28] augments the SM by a global U(1) symmetry (referred to as the Peccei-Quinn symmetry) imagined to be spontaneously broken and to give rise to Goldstone bosons called axions. The θ-term is then essentially eliminated by the vacuum expectation value of the axion. Subsequently, much experimental effort and millions of dollars have been spent on the search for axions. The fact that axions have not been observed is, however, not in conflict with the empirical limit on the θ because the allowed axion parameter space has not yet been completed explored experimentally. Moreover, other proposals exist [29] to explain the small value of θ. For example, if *CP* violation is implemented spontaneously, $\theta = 0$ as the leading effect arises naturally. Clearly, an experimental determination of d_n has the potential to lead to a new paradigm for *CP* violation.

Electroweak CP

In any case, because *CP* violation as represented in the CKM matrix embodies flavor mixing, d_n is very small in the SM; calculations predict it to be 10^{-32} to 10^{-30} $e{\cdot}$cm [30,31], well beyond the reach of any experiment being considered at present. Because of the experimental evidence indicating the presence of direct *CP* violation, a pure $\Delta S = 2$ interaction is insufficient to impact experiments. As d_e cannot originate in the SM even from three-loop diagrams, the prediction of the SM, $d_e \, (\text{SM}) < 10^{-40}$ $e{\cdot}$cm [32], is also well beyond current experimental capabilities.

Models of new physics, including left-right symmetric models, nonminimal models in the Higgs sector, and supersymmetric models as discussed above, allow for *CP*-violating mechanisms not found in the SM, including terms that do not change flavor. For this reason, searches for d_n and d_e—for which the effects of flavor changing *CP* violation are suppressed as in the CKM case—have been significant for the development of such models. The models allow for effects that might be observed in a variety of experiments including the new searches for d_n and d_e, *B*-meson decay, transverse polarization of muons in $K_{\mu3}$ decay; decays of hyperons; decays of τ leptons; and *CP* violation in charmed hadron decays.

If the origin of *CP* violation is essentially correctly described in the SM through δ_{CKM}, large characteristic *CP* asymmetries are predicted for *B*-decay [27]. Recent results from the *Belle* and *BaBar* collaborations present compelling evidence for *CP* violation in the neutral *B* meson system roughly consistent with these expectations [33]. However, the large, *CP*-violating effects in *B*-decay arising in the SM could be obscuring signals of new physics that would be manifest otherwise in these decays. In this case, the fact that *CP* violation arising from the CKM matrix is very small in d_n leaves open the possibility that measurable effects will be found in d_n even if further analysis finds no deviation from the SM in *B* decays.

More generally, models of new physics contain sources of *CP* violation that affect both flavor-changing and flavor-conserving sectors with a relative weighting characteristic of the model. Correlations between flavor-changing and flavor-nonchanging observables (such as between *B*-decay and EDMs) can provide important clues to distinguish among competing theories.

Models of New Physics

As the discussion of the baryon asymmetry indicates, there exists strong motivation from the standpoint of cosmology to search for new sources of *CP* violation. The level of sensitivity needed to probe *CP* violation at a cosmologically significant level is indicated by the EDM-baryogenesis bands in Figures I-2, I-3, and I-4. It is similarly useful to consider the implications of the nEDM experiment for other models of new *CP* violation. As illustrated above in the case of SUSY, such models provide a natural and reasonable expectation that the values of d_n may lie at levels just beyond current empirical limits. Additionally, these models clearly show that significant correlations among different *CP* measurements can be expected, and that knowledge of these correlations is essential to unraveling the origin of the effects once they are found. If d_n is *not* seen at levels just beyond current empirical limits, one would arrive at the important conclusion that something quite special is going on.

In the following discussion of models, we focus on d_n, but it is important to bear in mind that the EDM of atoms (see below) and of the electron are also relevant. In many models, d_e is predicted to lie at least an order of magnitude below d_n. The reasons for this are the smaller chirality flip and weaker gauge couplings for leptons [34]. However, there is a great deal of model dependence, and in the absence of experimental information, d_e or d_n may be favored by the specific choice of parameters. In parallel to efforts to improve the experimental sensitivity to d_n, ambitious attempts to improve on the electron EDM measurements are being vigorously pursued. These efforts include a measurement on an excited metastable state of PbO [35] in which a factor of 10^4 improvement in statistical sensitivity is being sought and a measurement of the change in magnetization of solid-state systems such as GdIG or GaGd garnet upon application of electric field [36] in which a factor of 10^5 improvement is possible. Based on experience with these theoretical models and the current empirical limits, one may infer that new experiments to measure d_e or d_n would have to exhibit about the same improvements in sensitivity over existing measurements to be competitive. In the case of neutral atoms, various nuclear-structure effects are expected to amplify the impact of *CP* violation (see Reference [37]

and references therein), so new experiments with sensitivity comparable to that of the ^{199}Hg measurement will effectively probe this *CP* violation with a sensitivity comparable to that of the new d_e and d_n measurements.

Among models, one leading candidate, SUSY, has already been discussed above. In addition, left-right symmetric gauge models [38] have many intriguing features such as the highly symmetric starting point that motivates them. Although many potential dynamical sources of *CP* violation exist, the EDM in these models is driven by W_L–W_R mixing, the scale of which is set by the mass of the W_R boson. These models are interesting because they show that it is possible, through W_L–W_R mixing, to have ε' agree with neutral kaon decay, yet have d_n large enough to be observable (at the level of O(10^{-27}) *e·*cm [27]). The electron EDM can be naturally in the range of 10^{-26} to 10^{-28} *e·*cm [34]. The most strict limits on the relevant parameters in these models [39] have been determined from measurement of the EDM of diamagnetic atoms (atoms with paired electrons such as ^{129}Xe and ^{199}Hg). Diamagnetic systems are sensitive to *CP* violating effects predominantly through the nuclear force rather than through d_e [see, e.g., Equation (I.4), below].

CP violation in the CKM matrix of the SM may also occur "minimally" via the complex couplings of the Higgs to the fermions. A class of nonminimal models arises in the Higgs sector through *CP* violation generated from spontaneous symmetry breaking. There is considerable latitude in constructing these models, because the Higgs sector represents the largest area of unknown physics of the SM and lacks direct experimental support. As with other models, such as SUSY, the origin of an EDM in multi-Higgs models can lie in one of several sources:

(1) Higgs exchanges that generate an EDM for individual quarks d_q or leptons. Such direct one-loop contributions with charged Higgs, tend to give a large d_n incompatible with experimental upper limits, if one insists that the empirical value of ε also originates entirely within this sector [40]. Thus, for these models to be viable, one must arrange for ε to arise in part (or entirely) from other sources (such as the CKM phase).

(2) *CP* odd gluonic operators that induce a d_n. Because the contribution of these operators is suppressed by successively higher powers of M_H with increasing operator dimension, the operator most likely to give the dominant contribution to d_n (excluding $G\tilde{G}$, which is related to θ as discussed earlier) is $G^2\tilde{G}$. Estimates for the resulting d_n suggest values $d_n \sim$ O(10^{-26}) *e·*cm [41,42].

(3) Quark color-electric dipole moments, d_q^{QCD}, (two-loop effects) that lead to large d_n with values close to the current upper bound [41,43,44]. The corresponding two-loop contribution to d_e is obtained by replacing gluons in the color-electric dipole operator by EW gauge bosons and attaching them to a lepton. This yields $d_e \sim$ few 10^{-27} [41,43,44,45,46] which is just at the present experimental bound.

Recognizing that this classification is actually quite general and applicable in particular to supersymmetric theories [47], the EDM of the neutron and the paramagnetic atom *Tl* can be expressed in terms of quantities appearing in this classification as [48,49]

$$d_n = 1.1(\frac{4}{3}d_d - \frac{1}{3}d_u) + O(1)d_q^{QCD} + O(1)(q/10^{-9})d_n^{2005}$$

(I.4)

$$d_{Tl} = -600d_e + O(10^{-4})d_q + O(10^{-3})d_q^{QCD} + O(10^{-3})(\theta/10^{-9})d_{Tl}^{1995}$$

where the expressions for the neutron have been taken from the QCD sum rule analysis of reference [49].

Corresponding relationships exist for the diamagnetic atoms; a typical result is

$$d_{Xe} = 10^{-3} d_e + O(10^{-4})d_q + O(10^{-3})d_q^{QCD} + O(10^{-1})(q/10^{-9})d_{Xe}^{1995} . \tag{I.5}$$

In these expressions, the contribution from strong *CP* violation involving the θ-term, has been expressed in terms of the current upper bounds ($d_{Tl}^{1995} \leq 6.610^{-24}$ *e*·cm, $d_{Xe}^{1995} \leq 1.410^{-26}$ *e*·cm, and $d_n^{1995} \leq 0.810^{-25}$ *e*·cm). A recent analysis [50] within the context of the MSSM has shown that the measurement [51] of the EDM of ^{199}Hg may be providing the most reliable constraint on *CP*-violating phases.

Thus, one cannot rule out the possibility that nonminimal Higgs models will lead to values for d_n and d_e that are observable with the improvements in sensitivity planned in next-generation experiments. These models may also make significant contributions to other *CP* violating observables, such as the transverse polarization in $K_{\mu3}$ decay, without necessarily having much effect on kaon decays. They are especially worthy of attention because Higgs dynamics also appears to be capable of providing sufficient *CP* violation to generate the BAU of today's universe at the EW scale.

Within each scenario, there can be numerous nontrivial correlations among the *CP* observables, rare decay rates, and gross features of the particle spectrum; for example, in the SO(10) GUT, d_n and d_e scale as $1/m^2$ with the scale m of supersymmetry breaking, whereas the $\mu \rightarrow e\gamma$ rate scales as $1/m^4$ [52].

Summary and Conclusions

There is ample reason to expect a nonzero value for the nEDM, with many theories predicting values lying within the six orders-of-magnitude window between the current limit and the value allowed by the SM. Experiments that explore the next two orders of magnitude would make a significant contribution to the search for new physics that complements the information to be gained from the Large Hadron Collider (LHC).

C. EDM Experiments Worldwide

The history of nEDM measurements is closely interwoven with our evolving knowledge of discrete symmetries in physics. In 1950, when parity was considered an inviolable symmetry, Purcell and Ramsey [2] pointed out the need to test this symmetry via detection of a nEDM. They then carried out a pioneering experiment [53,3] setting an upper limit at 5×10^{-20} *e*·cm for nEDM. The role of the baryon (proton, neutron, hyperons) EDMs in testing parity symmetry was extensively discussed in the seminal paper of Lee and Yang [54], who cited the yet-unpublished nEDM result from Smith, Purcell, and Ramsey [53,55].

The discovery of parity violation in 1957 [56,57,58] prompted Smith et al. to publish their nEDM result [3]. By this time, however, it was recognized [59,60] that *T* invariance would also prevent the neutron from possessing a nonzero EDM. Because no evidence of *T* violation was found even in systems that exhibited maximal parity violation, a nonzero nEDM was regarded as highly unlikely. However, Ramsey [61] emphasized the need to check *T* invariance experimentally. He also pointed out that Dirac's magnetic monopole violates both parity *(P)* and *T* symmetry. The experimental activities on the nEDM lay dormant until *CP* violation, directly linked to *T* violation via the *CPT* theorem [62,63,64], was discovered in 1964 [65].

The interest in the nEDM was greatly revived when a large number of theoretical models, designed to account for the *CP*-violation phenomenon in neutral kaon decays, predicted a nEDM large enough to be detected. Many ingenious technical innovations have since been implemented, and the experimental limit of nEDM was pushed down to 3×10^{-26} *e*·cm, a six-order-of-magnitude improvement over the first EDM experiment [4]. Unlike *P* violation, the

underlying physics for *CP* and *T* violation remains a great enigma nearly 40 years after its discovery. As discussed above, improved nEDM measurements will continue to provide the most stringent tests for various theoretical models and to reveal the true origins of *CP* violation.

Concurrent nEDM Experiments

The search for a nonzero nEDM continues at the ILL with a two-phased approach. Phase 1 develops their technique and hopes to obtain a sensitivity of 10^{-27} *e*·cm. Phase 1 is in advance of this project by several years. If no limitation is discovered, they will ask the ILL to construct a more intense cold-neutron beamline that should provide a statistical sensitivity of 10^{-28} *e*·cm, and this phase is on a schedule comparable to this project.

The arrangement is shown in Figure I-4 [66]. The design features a superthermal source based on liquid helium (LHe) to produce UCNs well away from their neutron detectors, thus essentially eliminating cold-neutron-induced background counts. A description of the super-thermal mechanism is given in Section IV. The measurement employs the Ramsey method of separated oscillatory fields [67]. To avoid the geometric phase effect (see Section VII), the measurement cells are protected with a superconducting shield to isolate the cells from external magnetic fields. The main precession field is generated with a solenoid that possesses good field uniformity. A key feature is the cell arrangement, which contains three cells (not shown). There are two outer high-voltage (HV) electrodes that are held at ground and two inner electrodes held at the same HV. The measurement cells are between the ground and HV electrodes. The magnetometry cell is between the two HV electrodes and has no electric field, and hence cannot have an EDM effect. The precession of the neutrons from each of the three cells is measured independently. Magnetic fluctuations in the outer two cells are corrected for by the fluctuations in the inner cell. The design does not employ a comagnetometer, so the ability to correct for the spatial variations in the magnetic field is limited to the scale of the cells.

A new UCN source, based on the superthermal production process in solid deuterium, is under construction at the Paul Scherer Institute (PSI) [68]. The current plan for measuring the nEDM involves moving the EDM apparatus from the previous ILL nEDM experiment to the PSI. Their plans to modify the apparatus to overcome the geometric phase effect that limited the device at the ILL are unknown.

The design of the experiment planned for an experiment at the Petersberg Nuclear Physics Institute (PNPI) is under construction. This experiment also uses a deuterium superthermal source. It also uses the Ramsey method and features eight cells with different electric fields. The cells are quite large to gain statistics and have many external magnetometers. This type of magnetometry has proven very challenging in the past.

There are rumors of a new nEDM experiment that measures the spin precession of the neutrons as they pass through a single crystal. The advantage of this approach is the enormous electric field produced by the lattice. Not many details are available, but crystal experiments in the past have had difficulty getting enough neutrons that pass precisely along the crystal axis and in controlling the $v \times E$ systematic because it is a beam experiment [69].

There are similar rumors of one or two Japanese nEDM efforts at either KEK or JPARC. No details are available.
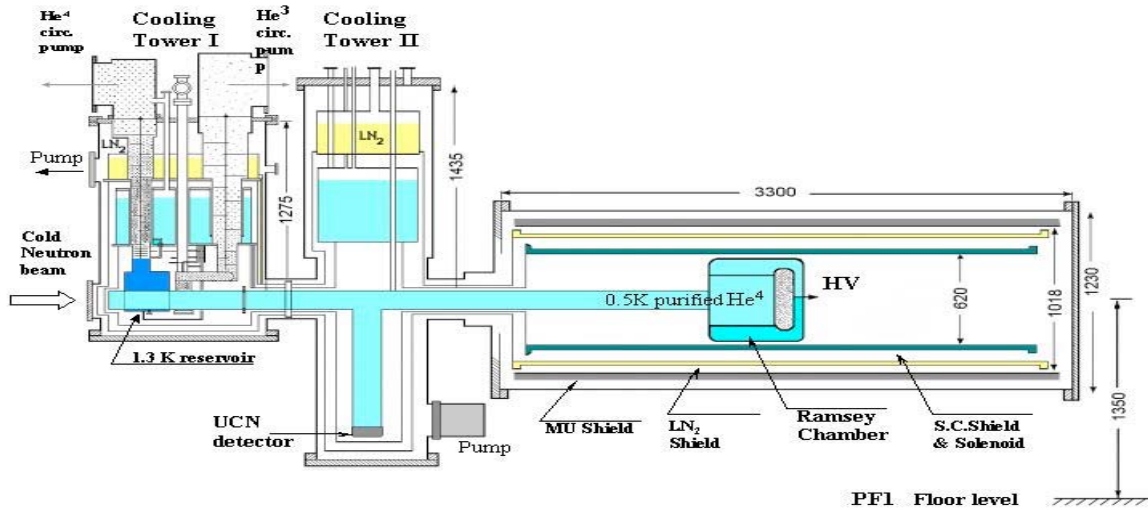
Fig. I-4.   The experimental arrangement for the next neutron EDM experiment at the ILL.

EDM Experiments in Diamagnetic Atoms

        Diamagnetic atoms have no unpaired electrons, and the major contribution to the EDM of the system comes from the nucleus. The atomic electrons screen the effects of the EDM. The nuclear EDM is only measurable because relativistic effects keep the cancellation between the nucleus and the electrons from being exact. As noted earlier, the nuclear contribution to the EDM is sensitive to different parts of the *T*-violating force as compared to the neutron. For example, ^{199}Hg is about 100 times less sensitive to quark chromo-electric EDMs compared to the neutron, but is about 1,000-10,000 times less sensitive to elementary quark EDMs. In addtion, there are theoretical hurdles in converting diamagnetic EDMs into quark EDM or θ_{QCD} values. With these caveats, under some simplifying, model-dependent theoretical assumptions, the atomic EDM is sometimes quoted in terms of a nEDM, however the measurement of the neutron and diamagnetic-atom EDMs actually provide independent information. The conversion factor depends on the atomic number of the nucleus.

        A series of experiments has been carried out on ^{199}Hg at the University of Washington. Their latest result gives $d_{Hg} < 2.1 \times 10^{-28}$ *e*·cm. For mercury, the conversion factor to d_n is about 100, which translates into a limit on $d_n < 2 \times 10^{-26}$ *e*·cm [70]. This result is very close to the direct limit from the ILL experiment. Efforts continue to improve the mercury result, and another factor of 2 or so may be expected in the next few years. Orders-of-magnitude improvement seems unlikely in the near future.

        The other important diamagnetic atom is ^{129}Xe. The current limit is $d_{Xe} < 2 \times 10^{-26}$ *e*·cm. After applying the appropriate conversion factor, the value for $d_n < 2 \times 10^{-23}$ *e*·cm [71]. A new experiment at Princeton with an expected sensitivity of $d_{Xe} \sim 10^{-30} – 10^{-31}$ *e*·cm is underway [72].

        A program is underway Argonne National Laboratory towards a measurement of the electric dipole moment of ^{225}Ra [73]. This experiment will take advantage of the expected enhancement of the atomic EDM of ^{225}Ra due to the octupole deformation of the ^{225}Ra nucleus. Currently, the feasibility of laser trapping and cooling of ^{225}Ra atoms is being investigated.

Electron EDM Experiments

In theories of the weak interaction, the EDM of the electron is zero in first order, and, as discussed above, the electron EDM is sensitive to different parts of the *T*-violating interaction. There have been a number of precision measurements of the EDM of paramagnetic atomic and molecular systems, from which limits for the EDM of the electron can be inferred. For example, the measurements in thallium by Commins et al. [74] suggest a value of $d_e = (0.18 \pm 0.12 \pm 0.10) \times 10^{-26}$ *e*·cm. This experimental limit is about 13 orders of magnitude above the SM predictions, but some extensions for physics beyond the SM predict effects within range of these experiments.

Polar molecules offer the opportunity for large atomic enhancement factors. There are two examples currently being investigated. The first is YbF, where an upper limit of $d_e < 4 \times 10^{-25}$ *e*·cm has been reported by the Sussex group [75]. The group continues to work with a hoped for sensitivity of 10^{-28} *e*·cm. The other system is PbO. The work at Yale is supposed to be at an advanced stage. The Yale team hopes for a sensitivity of 10^{-30} *e*·cm [76].

The work in polar molecules depends on detailed molecular structure. A rather different approach has been taken by a Los Alamos group investigation of GaGd garnet [77]. The idea is to place high voltage on an amorphous sample of the garnet and look for a very weak induced magnetic field. Noise is suppressed by working at cryogenic temperatures, and the magnetic field sensor is a SQUID.

There are many examples of searches for d_e in the proposal stage, but the details and their reach are still not public.

Other Low-Mass Particles

There are two experiments proposed on other low-mass particles, one to search for the EDM of the muon and the other to search for the EDM of the deuteron. Both use the *g-2* ring at Brookhaven National Laboratory. The muon is like a heavy electron, so the physics is related to d_e. The sensitivity being sought is $d_\mu < 10^{-24}$ *e*·cm [78]. While this value appears quite a bit less sensitive than the values for d_e, there are some special extensions to the SM where the EDM is enhanced due to the large mass of the muon. In the case of the deuteron, the sensitivity is supposed to be $d_d < 10^{-27}$ *e*·cm [79]. The physics of d_d is quite similar, though complementary, to that of d_n (the up and down quark EDMs enter with different relative signs compared to the neutron), so there is little reason to expect this measurement to have the same discovery potential as the new initiatives on the neutron. Both of these proposals await approval from Brookhaven and the funding agencies.

References

1. J. Chadwick, *Nature* **129**, 312 (1932);
   Proc. Roy. Soc. (London) **A136**, 692 (1932).
2. E.M. Purcell and N.F. Ramsey, *Phys. Rev.* **78**, 807 (1950).
3. J.H. Smith, E.M. Purcell, and N.F. Ramsey, *Phys. Rev.* **108**, 120 (1957).
4. C.A. Baker et al., (submitted to *Phys. Rev. Lett.*) [http://arxiv.org/abs/hep-ex/0602020].
5. A. Angelopoulos et al. (CPLEAR Collaboration), *Phys. Lett.* **444B**, 43 (1998).
6. G. Buchalla et al., *Nucl. Phys.* **B370**, 69 (1992);
   A.J. Buras et al., *Nucl. Phys.* **B408**, 209 (1993);
   M. Ciuchini, *Nucl. Phys. Proc. Suppl.* **59**, 149 (1997).
7. R. Tribble, chair. Subcommittee on Fundamental Physics with Neutrons Report to the Nuclear Science Advisory Committee (2003)
   [http://www.sc.doe.gov/production/henp/np/nsac/nsac.html].

8. S. Weinberg, *The First Three Minutes* (Harper-Collins Publishers, NY, 1977), p.95.

9. A.D. Sakharov, *JETP Lett.* **5**, 24 (1967).

10. V.A. Kuzmin, V.A. Rubakov, and M.E. Shaposhnikov, *Phys. Lett.* **155B**, 36 (1985).

11. M. Fukugita and T. Yanagita, *Phys. Lett.* **174B**, 45 (1986).

12. M.E. Shaposhnikov, *Nucl. Phys. B* **287**, 757 (1987).

13. G. 't Hooft, *Phys. Rev. Lett.* **37**, 8 (1976).

14. A.G. Cohen, D.B. Kaplan, and A.E. Nelson, *Annu. Rev. Nucl. Part. Sci.* **43**, 27 (1993).

15. K. Kajantie et al., *Nucl. Phys. B* **466**, 189 (1996).

16. A. Riotto, *Phys. Rev. D* **58**, 095009 (1998).

17. M. Carena, et al, *Nucl. Phys. B* **503**, 387 (1997);
    M. Carena et al, *Nucl. Phys. B* **599**, 158 (2001).

18. C. Balazs, M. Carena, and C.E.M. Wagner, *Phys. Rev. D* **70**, 015007 (2004).

19. C. Lee, V. Cirigliano, and M.J. Ramsey-Musolf, *Phys. Rev. D* **71**, 075010 (2005).

20. C. Balazs, et al, *Phys. Rev. D* **71**, 075002 (2005).

21. V. Cirigliano et al., (to be published in Phys. Rev. D) [http://arxiv.org/abs/hep-ex/0603058].

22. T. Konstandin, T. Prokopec, and M.G. Schmidt, *Nucl. Phys. B* **716**, 373 (2005);
    Nucl. Phys. B **679**, 246 (2004).

23. T. Konstandin et al, [http://arxiv.org/abs/hep-ex/0505103].

24. V. Cirigliano et al., [http://arxiv.org/abs/hep-ex/0603246].

25. V. Baluni, *Phys. Rev. D* **19**, 2227 (1979).

26. R.J. Crewther et al., *Phys. Lett.* **88B**, 123 (1979);
    Errata, **91B**, 487 (1980).

27. I.I. Bigi and A.I. Sanda, *CP Violation* (Cambridge University Press, Cambridge, UK, 2000).

28. R. Peccei and H. Quinn, *Phys. Rev. Lett.* **38**, 1440 (1977);
    Phys. Rev. D **16**, 1791 (1977).

29. S. Barr and A. Zee, *Phys. Rev. Lett.* **55**, 2253 (1985).

30. I.B. Khriplovich and A.R. Zhitnitsky, *Phys. Lett.* **109B**, 490 (1982).

31. M.B. Gavela et al., *Phys. Lett.* **109B**, 215 (1982);
    B. McKellar et al., *Phys. Lett B* **197**, 556 (1987).

32. M.E. Pospelov and I.B. Khriplovich, *Yad. Fiz.* **53**, 1030 (1991*) [Sov. J. Nucl. Phys.* **53**, 638 (1991)].

33. see B. Aubert, [http://arxiv.org/abs/hep-ex/0203007] and
    K. Abe, [http://arxiv.org/abs/hep-ex/0202027] and
    references therein.

34. W. Bernreuther and M. Suzuki, *Rev. Mod. Phys.* **63**, 313 (1991).

35. Yale Proposal. De Mille, Search for an Electron Electric Dipole Moment in the *a*(1) state of Pb0.

36. S.K. Lamoreaux, *Phys. Rev. A* **66**, 022109 (2002);
    B.J. Heidenreich et al., *Phys. Rev. Lett.* **94**, 253004 (2005).

37. J. Dobaczewski and J. Engel, *Phys. Rev. Lett.* **94**, 232502 (2005).

38. R.N. Mohapatra, *Unification and Supersymmetry*, (Springer-Verlag, 1992).

39. P. Herczeg, in *Symmetries and Fundamental Interactions in Nuclei*, ed. W. C. Haxton and E. Henley (World Scientific, 1995).

40. G. Beall and N.G. Deshpande, *Phys. Lett.* **132B**, 427 (1983).

41. D. Chang, W.-Y. Keung, and T.C. Yuan, *Phys. Lett.* **251**, 608 (1990).

42. I.I. Bigi and N.G. Uraltsev, *Nucl. Phys. B* **353**, 321 (1991).

43. M.S. Barr and A. Zee. *Phys. Rev. Lett.* **65**, 21 (1990).
44. J. Gunion and D. Wyler, *Phys. Lett.* **248B**, 170 (1990).
45. R.G. Leigh, S. Paban, and R.-M. Xu, *Nucl. Phys. B* **352**,45 (1991).
46. C. Bowser-Chao, D. Chang, and W.-Y. Keung, *Phys. Rev. Lett.* **79**, 1988 (1997).
47. S.M. Barr, *Int. Journal Mod. Phys. A* **8**, 209 (1993).
48. R. Barbieri, A. Romanino, and A. Strumia, *Phys. Lett.* **369B**, 283 (1996).
49. M. Pospelov and A. Ritz, *Ann. Phys.* **318**, 119 (2005).
50. T. Falk et al., *Nucl. Phys. B* **560**, 3 (1999).
51. J.P. Jacobs et al., *Phys. Rev. Lett.* **71**, 3782 (1993);
    M. Romalis et al., *Phys Rev. Lett.* **86**, 2505 (2001).
52. S. Dimopoulos and L.J. Hall, *Phys. Lett.* **344B**, 185 (1995).
53. J.H. Smith, Ph.D. thesis, Harvard University, 1951 (unpublished).
54. T.D. Lee and C.N. Yang, *Phys. Rev.* **104**, 254 (1956).
55. N.F. Ramsey, *Molecular Beams* (Oxford University Press, Oxford, 1956).
56. C.S. Wu et al., *Phys. Rev.* **105**, 1413 (1957).
57. R. Garwin, L. Lederman, and M. Weinrich, *Phys. Rev.* **105**, 1415 (1957).
58. J. Friedman and V. Telegdi, *Phys. Rev.* **105**, 1681 (1957).
59. L. Landau, *Nucl. Phys.* **3**, 127 (1957).
60. I.B. Zel'dovich, *J. Exp. Theor. Phys.* **6**, 1488 (1957) [*Sov. Phys. JETP* **6**, 1148 (1957)].
61. N.F. Ramsey, *Phys. Rev.* **109**, 222 (1958).
62. J. Schwinger, *Phys. Rev.* **82**, 914 (1951);
    91, 713 (1953).
63. G. Lüders, *Kgl. Danske Videnskab Selskab. Mat. Fiz. Medd.* **28**, No. 5 (1954);
    G. Lüders and B. Zumino, *Phys. Rev.* **106**, 385 (1957).
64. W. Pauli, in *Niels Bohr and the Development of Physics* (McGraw-Hill, New York, 1955).
65. J.H. Christenson et al., *Phys. Rev. Lett.* **13**, 138 (1964).
66. http://minoserv.maps.susx.ac.uk/~nedm/indexhtm.
67. N.F. Ramsey, *Phys. Rev.* **76**, 996 (1949).
68. http://ucn.web.psi.ch/.
69. http://physics.valpo.edu/facultyResearch/proposal_MDM/
70. M.V. Romalis et al., *Phys. Rev. Lett.* **86**, 2505 (2001).
71. T.G. Vold et al., *Phys. Rev . Lett.* **52**, 2229 (1984).
72. http://www.atomic.princeton.edu/romalis/CP/.
73. http://www-mep.phy.anl.gov/atta/research/radiumedm.html.
74. E.D. Commins et al., *Phys. Rev. A* **50**, 2960 (1994).
75. J.J. Hudson et al., *Phys. Rev. Lett.* **89**, 023003 (2002).
76. http://pantheon.yale.edu/%7Edpd5/EDM.htm.
77. S.K. Lamoreaux, *Phys. Rev. A* **66**, 022109 (2002).
78. Y.K. Semertzidis et al., In the proceedings of KEK International Workshop on High Intensity Muon Sources (HIMUS 99), Tsukuba, Japan, Dec 1999, (hep-ph/0012087).
79. Y.K. Semertzidis et al. (EDM Collaboration), AIP Conf.Proc.**698**:200–204, 2004 [hep-ex/0308063].

II.   Proposed Measurement – Overview

A. Conceptual Design

This experiment is based on a technique to measure the electric dipole moment of the neutron (nEDM) that is qualitatively different from the strategies adopted in previous measurements. This overview defers many crucial technical details that are essential to the success of the measurement until later in the conceptual design report (CDR).

The overall method adopted here [1] is to form a three-component fluid of neutrons and ^{3}He atoms dissolved in a bath of superfluid ^{4}He at ~0.5 K. Both the neutron and ^{3}He magnetic dipoles can be made to precess in the plane perpendicular to the *B* field when placed in an external magnetic field. The measurement of the nEDM comes from a precision measurement of the difference in the precession frequencies of the neutrons and the ^{3}He atoms, as modified when a strong electric field parallel or antiparallel to *B* is activated. This comparison measurement assumes the neutral ^{3}He atom has a negligible EDM, as expected for a diamagnetic atom of low atomic number [1].

The primary method for determining the nEDM, d_n, is to study the precession frequency of neutrons with aligned spins in the plane perpendicular to a static magnetic field, B_0. Application of a static electric field, E_0, parallel (antiparallel) to B_0 changes the Larmor precession frequency, ν_n, in proportion to d_n. The precession frequency is:

$$\nu_n = -\left[2\mu_n B_0 \pm 2d_n E_0\right]/h \equiv \nu_0 \pm \Delta\nu/2 \qquad (\text{II}.1)$$

where the minus sign reflects the fact that $m_n < 0$. Thus, the frequency shift, $\Delta\nu$, as the direction of E_0 is reversed, is

$$\Delta\nu = -4d_n E_0/h, \qquad (\text{II}.2)$$

In the case of $B_0 = 10$ mG and $E_0 = 0$, the Larmor precession frequency is $\nu_0 = 29.2$ Hz. With $E_0 = 50$ kV/cm and using a nominal value of $d_n = 4 \times 10^{-27}$ e·cm, the frequency shift, when the electric field is reversed, is

$$\Delta\nu = 0.19\mu \text{ Hz} = 0.65 \times 10^{-8}\nu_0. \qquad (\text{II}.3)$$

Note that the absolute frequency shift, $\Delta\nu$, is critical, not the fractional shift in frequency.

The figure of merit for nEDM experiments varies as $E_0\sqrt{N\tau}$, which can be derived from Equation II.2. The neutrons decay, implying that the measurement must be repeated many times. *N* is the number of neutrons in the cell during a single measurement and τ is the duration of each measurement. The constant of proportionality depends on the experimental arrangement. The object of any design is to maximize these three quantities, which this experiment achieves as explained below.

Neutrons (WBS 1.2 and 1.6)

The conceptual design for the proposed apparatus is shown in Figure II-1. The picture is derived from a full 3-D engineering model that has been created to study whether all the scientific ideas can be realized in a single piece of equipment. The apparatus is divided into two parts, the lower cryostat where the measurement is made and the upper cryostat where the ^{3}He is injected and removed as well as where the refrigeration is done. The upper cryostat is where all services enter the system except for the light guides described later.
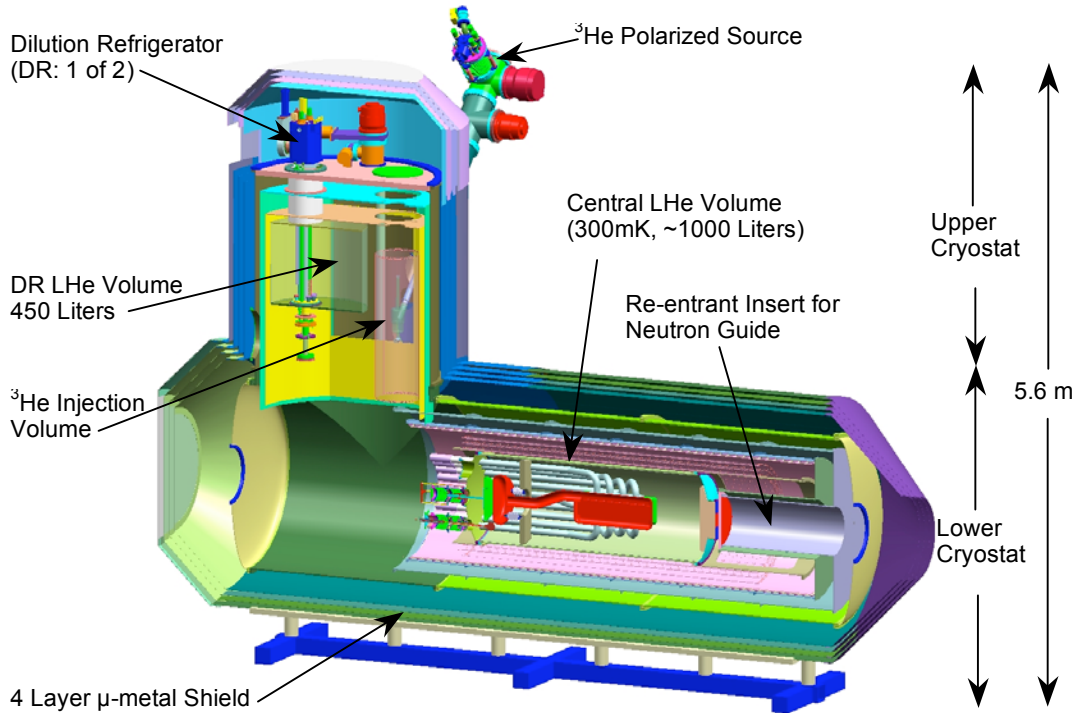
Fig. II-1.   The schematic overview of the full detector apparatus for the neutron EDM apparatus. This view most clearly demonstrates the relationship between the upper and lower cryostats. The upper cryostat contains the refrigeration and ^{3}He systems. The lower cryostat contains the entrance port for the neutrons, the magnets/magnetic shielding and the measurement cells.

The polarized, cold neutrons are prepared in a beam splitter that uses magnetized mirrors to either reflect or transmit the two polarization states. The last stage of the splitter consists of spin rotators to orient the spins parallel to B_0, which is horizontal and normal to the direction of the neutrons, and a weak guide field to preserve the spin directions. The two neutron guides (not shown) enter from the right and terminate roughly 50 cm upstream of the high voltage (HV) plates. The gap is necessary to preserve electrical stability.

The placement of the EDM experiment at the SNS Fundamental Neutron Physics Beamline (FNPB) is shown in Figure II-2. The splitter begins at the upstream extent of the mirrors. The details of its operation are given in the subsystem description. The beginning of the splitter marks the end of the FNPB beam guide and the start of the EDM project.

The lower cryostat contains two measuring cells sandwiched between a HV electrode and two ground electrodes as shown in Figure II-3. The measurement cells are loaded with ultracold neutrons (UCNs) using the strategy suggested first by Golub and Pendlebury [2] and known as superthermal production. The UCNs are locally produced inside a cell filled with ultrapure, superfluid ^{4}He at 0.5 K. Cold neutrons with energies of 1 meV may interact with the superfluid and be down scattered to energies less than 165 neV with a recoil phonon in the superfluid, carrying away the missing energy and momentum. At 0.5 K, the rate of upscattering of UCN by phonons is negligible. The cold-neutron beam that traverses the cells is dumped in a boron nitride block downstream of the cells.
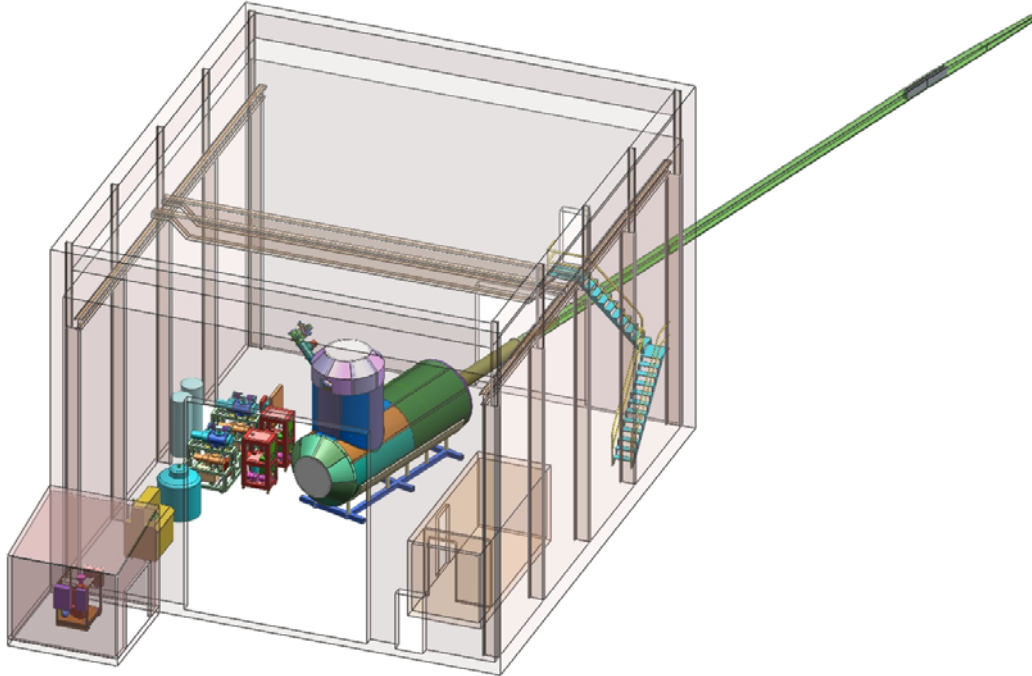
Fig. II-2. The layout of the nEDM experiment at the FNPB. The cryostat is situated in the UCN guide hall is on the left. The neutron beam passes through the beam splitter from the monochromator to the experiment. The downsteam end of the ballistic guide section is the dividing line between the FNPB and EDM. The UCN building is also part of FNPB.
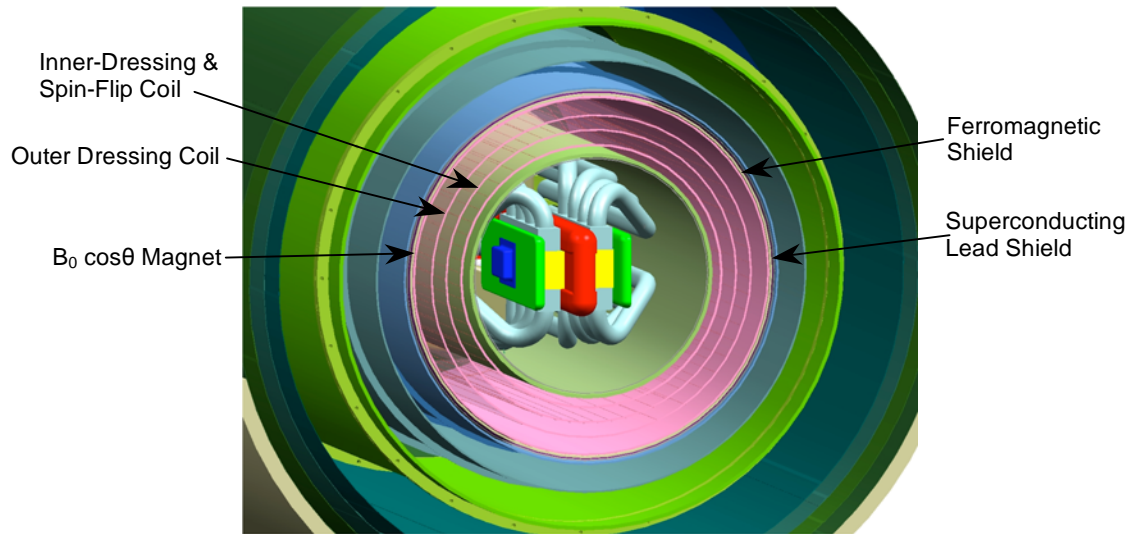
Fig. II-3. The two measurement cells surrounded by the HV electrodes and and SQUID package. In concentric circles from the inside to outside are the HV ground return, the inner dressing coil, all other magnet coils, the ferromagnetic shield, the superconducting shield, the 4 K cryoshield, the 50 K cryoshield, and the outer vacuum jacket.

The averaged UCN production rate [3] at the Spallation Neutron Source (SNS) is about 0.3 UCN/cm^3/s. The measurement cells employ deuterated polystyrene coatings to minimize neutron absorption by hydrogen [4]. The goal for the mean life of a neutron in a trap filled with

pure ^{4}He is about 500 s as a result of losses by neutron β decay and neutron/wall interactions. The neutron density will reach $\rho_n \sim 150$ UCN/cm^3 during a 1000 s collection interval. The UCN density scales with the cold neutron flux. This UCN production technique and the UCN production-rate calculations for a ^{4}He filled UCN trap have been tested and validated by Golub, et al. [2] and by the neutron-lifetime experiment now in progress at NIST [5]. The superthermal process produces more UCN than any other known method.

The liquid helium (LHe) provides two additional benefits. The dielectric strength of LHe is quite good, allowing for E_0 to be 50 keV/cm [6]. The low temperatures suppress neutron absorption mechanisms in the walls so that the UCN storage time can be of the same order as the neutron lifetime.

Magnetometry (WBS 1.5 and 1.6)

If the neutrons experience either temporal or spatial variations in the magnetic field, the precession frequency will contain fluctuations that will prevent the experiment from achieving the desired sensitivity. The solution is to introduce a second species that has no EDM and whose precession rate can be measured in the same volume so that the fluctuations can be removed [1]. Data from the latest EDM experiment at the ILL illustrates the situation as shown in Figure II-4 [7]. This experiment places polarized ^{199}Hg into the neutron cell. The blue circles are the raw neutron resonant frequency. The nonstatistical fluctuations are clearly visible. The large step, near 15 hr, corresponds to an electric-field reversal. When the corrections are applied for the field variations measured by the ^{199}Hg, the red circles are obtained; they are consistent with Shot noise.
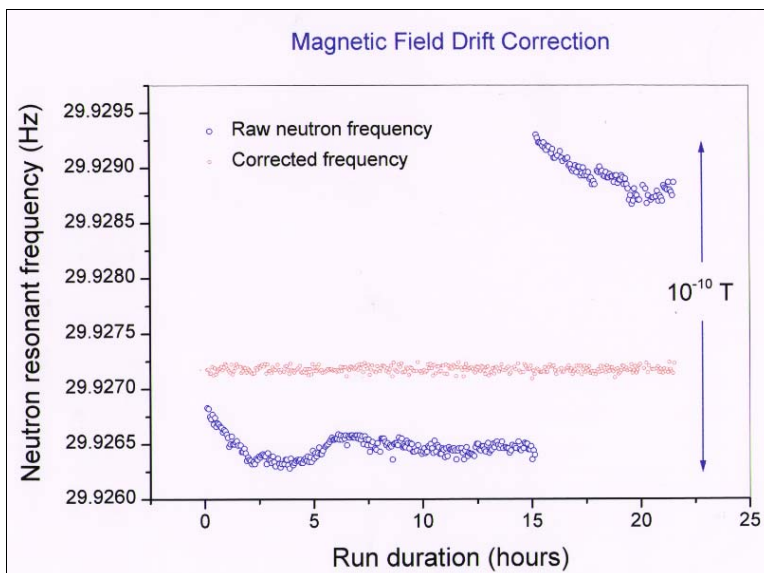
Fig. II-4.   Data from the recently completed ILL EDM experiment [8]. The blue circles are the EDM signal without field corrections from the comagnetometer. The red circles are the EDM signal corrected for field fluctuation.

The goal of the nEDM experiment is a factor of 100 improvement in the neutron EDM sensitivity. For an improvement beyond a factor of 3–10, magnetic gradient noise requires additional magnetometry to suppress such noise. The optimal magnetometer to eliminate the magnetic field noise and many potential systematic errors is one that occupies the same volume as the neutrons. The collaboration has adopted this approach to overcome potentially insurmountable problems in achieving the goal. The only species that can coexist in the same

volume as the LHe is ^{3}He. ^{3}He can be polarized to nearly 100%. ^{3}He is a diamagnetic atom and has no EDM greater than 10^{-28} e·cm because the dependence of the EDM on atomic number varies as Z^2. Because ^{3}He is much lighter than ^{199}Hg, it has a negligible EDM because the experimental upper limit on ^{199}Hg is less than 10^{-28} e·cm. Except for the small gravitational fractionation of the neutrons, the ^{3}He will measure the same magnetic field as the neutrons and be quite accurate because the magnetic moments of the neutrons and of the ^{3}He atoms are the same to 10%. The precession rate of the ^{3}He may be measured using SQUIDs to detect their magnetization. The SQUIDs are placed just outside the ground planes for the HV as shown in Figure II-3. The SQUIDs need to have a noise level below 1 $\mu\phi_0/\sqrt{Hz}$.

The ^{3}He also serves as an analyzer of the neutron precession rate. The cross section for neutron absorption by ^{3}He is 59 b for spins aligned and 11 kb for spins opposite at thermal neutron energy (25.3 meV) [9] The cross sections both scale inversely with neutron velocity (with higher-order corrections at the level of 5 b). Thus, neutron absorption by ^{3}He is highly spin dependent, and if the ^{3}He concentration is adjusted to be about 10^{12} atoms/cc, the neutrons are only absorbed in the singlet state during the measurement cycle. The rate of neutron loss due to absorption is

$$1 - P_3 P_n \cos[(\gamma_3 - \gamma_n)B_0 t]. \tag{II.4}$$

The P_i are the ^{3}He and neutron polarizations and the γ_i are the gyromagnetic ratios of the two species.

When a neutron is absorbed on a ^{3}He atom, the reaction products are a proton and a triton that share 764 keV of energy. The reaction products produce scintillation light in the LHe that is emitted in the hard ultraviolet. If the measurement cell is coated with a wavelength shifter, the scintillation light is converted to the blue where it may be viewed with photomultiplier tubes (PMT). The best wavelength shifter is deuterated tetraphenyl butadiene (dTPB) because it has good conversion efficiency and has a small neutron-absorption cross section. The light guides that connect the cell to the PMTs exit the apparatus on the downstream end of the lower cryostat as shown in Figure II-5.
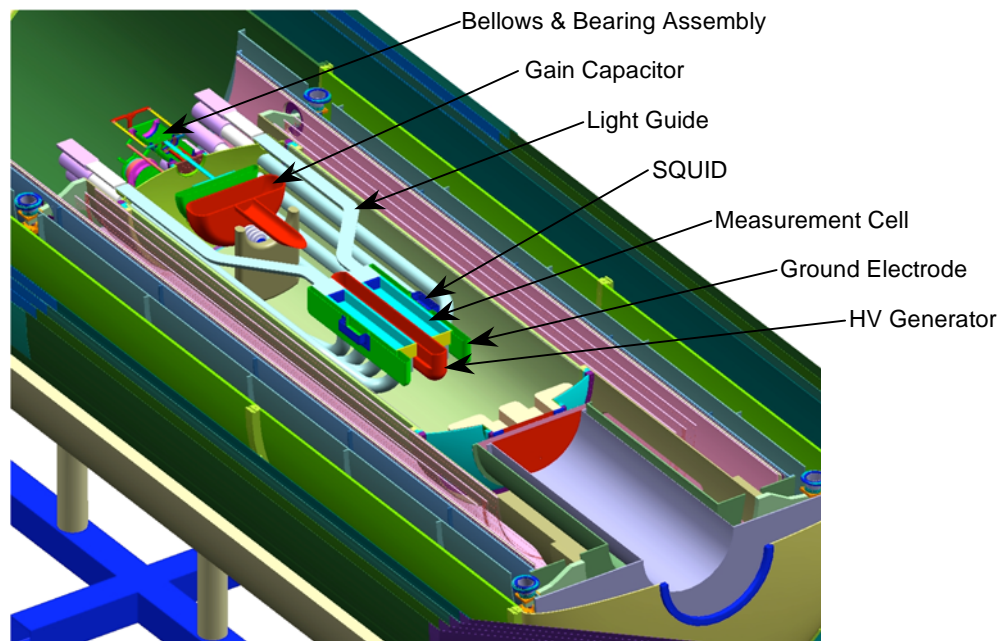

Fig. II-5.   The central region of the detector illustrating the measurement cells, HV electrodes, the path of the light guides, and the HV generator.

To summarize, the observed signals in this experiment are a SQUID signal that measures the ^{3}He magnetization and a scintillation signal that measures the beat frequency between the precession rates of the two species. The signature of an nEDM would appear as a shift in the beat frequency corresponding to the application of a strong electric field with no corresponding change in ^{3}He precession.

Electric Field (WBS 1.6)

The electric field applied to the measurement cell is well approximated by the field generated between the electrodes of a parallel plate capacitor. A number of requirements are imposed on the HV system.

The plates of the capacitor are to be built from acrylic coated with a thin layer of carbon-based material. There will be almost no current carried by the plates, and the carbon is an adequate conductor for this purpose. The plates are bombarded by cold neutrons during the UCN production. Acrylic ($C_5O_2H_8$) and carbon are amongst a short list of materials that do not produce activated nuclei that decay by γ-ray emission with time constants comparable to the UCN storage time. It is crucial to minimize the decay γ rays that will Compton scatter in the measurement cell and thus produce background scintillation light. The coating is also appropriate to minimizing the Johnson noise that materials with higher conductivity, such as metals, would induce in the SQUIDs. The resistivity of the thin coating minimizes the eddy-current heating generated by any radio frequency (RF) magnetic fields used in the experiment.

The electric field must be uniform and stable to 1% over the measurement cell to prevent systematic effects from entering. The measurement cell is also built from acrylic, with the neutron entrance face made from deuterated acrylic. The cell is a dielectric in the field. Distortions of the field by the cell are minimized by making an inset in the electrode to recess the cell.

The SQUIDs are very sensitive to electric discharge, and the apparatus must be designed to prevent all sparks. The HV electrode is contained in a cylindrical shell that also provides a ground reference. The ground shell must be situated at least 30 cm from the ends of the HV electrode to prevent sparks. The radius of curvature of the ends of the electrode also needs to be at least 5 cm to prevent sparking to the ground shell. This requirement sets the separation between the two cells to a minimum of 10 cm.

There are other considerations. The electric and magnetic fields need to be aligned to 1º to control systematic effects. The leakage currents across the cell must be less than 1 nA to limit electric field correlated magnetic fields.

The gap between the electrodes is 7 cm. A HV of 350 kV is required to obtain a 50 kV/cm electric field. LHe has excellent dielectric strength to support this field. The fixed electrodes, each with a capacitance of about 55 pF, are charged by placing them in parallel with a variable capacitor with a range of about 10 to 1000 pF. The variable capacitor is situated downstream of the neutron-beam absorber as shown in Figure II-5. The variable capacitor or HV generator begins at a separation of roughly 0.5 cm. It is charged with a power supply to 50 kV. At this voltage the vacuum feed-through can be commercially obtained. The wire connecting the power supply can be quite small and does not induce a major heat leak into the cryogenics. The HV electrode in the generator is disconnected from the power supply via a movable bellows and probe construct. Once this separation occurs, the HV system is isolated from any power-supply ripple. The movable ground electrode with a similar bellows construct is retracted to a distance of roughly 7 cm. Because the charge is conserved, the HV electrodes are raised to the desired 350 kV as the capacitance decreases.

Studies by the collaboration of the dielectric strength of LHe indicate the breakdown potential has a dependence on pressure. The need to pressurize the LHe in order to maintain the

desired field adds significant complexity to the apparatus, and this effect is being carefully studied before a final decision is made.

The electric field will be regularly monitored between the variable capacitor plates using a generating voltmeter. Occasionally, the field will be measured between the measurement electrodes, i.e., in the cells, using the Kerr effect. The Kerr effect is a change in ellipticity of polarized light propagating through a medium that is proportional to the square of the electric field in the region. An accuracy of 1% in less than 100 s is straightforward for these measurements.

Light Collection and Particle Identification (WBS 1.6)

The reference design calls for light guides to carry the wavelength-shifted scintillation light out the downstream end of the apparatus to room temperature PMTs. The PMTs should observe a mean of 12 photoelectrons based on a very similar design employed at NIST [5]. While this number of photoelectrons is sufficient to observe the scintillation light, it is not optimal for particle identification (ID) of the inducing particles, i.e., the triton and proton from neutron absorption on ^{3}He are distinguished from electrons from either neutron decay or Compton-scattered capture γ rays. Because the sensitivity of the experiment depends on the ability to suppress backgrounds, alternate designs are still being evaluated.

The particle ID depends on detecting the de-excitation modes of the ^{4}He molecular dimers that produce the ultraviolet light. The prompt signal arises from the singlet dimers. There is an after-pulsing that arises from the triplet de-excitation that has a much longer time constant. The triplet de-excitation is enhanced due to their mutual interaction (Penning ionization) that favors more rapid after-pulsing for highly ionizing particles where the energy is more densely deposited. The detection of the number of these single photoelectron events in the first few microseconds following the prompt pulse has been demonstrated to provide a particle ID technique. The technique works best if there are at least 40 photoelectrons per event in the prompt signal. A number of strategies are being pursued to improve the photoelectron count.

McKinsey [10] has reported good performance from specially prepared PMTs operated at 27 K in liquid neon. These tubes have a flash of metal on the photocathode to prevent charge buildup that occurs due to higher photocathode resistivity at low temperatures. Because room temperature helium quickly destroys a PMT by diffusing through the glass, the PMTs must be located in vacuum rather than in the LHe space. If PMTs can be made to work at 4 K, it will remove several of the gaps in the light guides necessitated by the cryogenics and increase the number of photoelectrons significantly. A side benefit is a reduction of the heat load on the cryogenics.

Another possibility is to use visible-light photon counters (VLPC) with cryogenically cooled electronics instead of PMTs. VLPCs have much better quantum efficiency and are viable if they have sufficiently low dark current for individual photon counting.

Laser fluorescence can also be used to measure the number of triplet states remaining after a fixed time following the prompt pulse. This technique is under development and will be described in the R&D section of the CDR.

Magnetic Fields and Shielding (WBS 1.5)

The EDM apparatus contains a number of magnets. The general uniformity specification for the magnets is 10^{-3}. The subsystem description gives the details of all magnets. The following description describes elements denoted in Figure II-3.

The main field, B_0, is produced by a saddle-shaped $cos\theta$ coil wound on the surface of a cylinder. The most challenging specification for this coil is to make the volume-averaged gradient better than 0.05 μG/cm along the field direction. This requirement is needed to control

the gradient field systematic described in the section on systematic effects. The proper boundary condition for a *cosθ* coil is provided if the coil is wound inside a ferromagnetic shield. Most common ferromagnetic materials lose their permeability at low temperatures, but there are amorphous metals and special alloys that maintain enough permeability to serve this function.

The SQUIDs require a superconducting enclosure to shield them from ambient magnetic noise. The full package of magnets will be enclosed in a superconducting shield. This shield will need to have at least 5 cm greater radius than the magnet coils because a superconductor has the wrong boundary conditions for *cosθ* coils. This shield needs to be cooled carefully to prevent the trapping of stray fields. A degaussing strategy is employed to remove residual fields.

The entire experiment is encased in a 4-layer conventional magnetic shield designed to isolate the experiment from the Earth's field and other magnetic contamination surrounding the experiment. The penetrations through these shields for various services are carefully designed to prevent contamination of the inner region with unwanted fields.

The polarized neutrons and ^{3}He are introduced into the measuring cells with their spins aligned with the magnetic field direction. At the beginning of the measurement period, the spins of both species are rotated by a RF π/2 pulse from another *cosθ* coil.

In order to diagnose the gradient field effect, two gradient *cos2θ* coils and a solenoid will be wound to provide an artificial gradient along the coordinate axes when desired.

Finally, two dressed-spin RF *cosθ* coils are placed at different radii. In a classical description, spin dressing is the modification of the effective gyromagnetic ratio of a species by flipping its spin rapidly compared to its Larmor frequency in the static field. A single dressing frequency exists that makes the effective gyromagnetic ratios of the neutrons and ^{3}He the same. A suitable RF spectroscopy can be performed to extract the EDM without the use of the SQUID signal [1]. The details are given in the magnet sections of this CDR. The dressed-spin coils are a backup to the SQUIDs whose noise spectrum cannot be known until the experiment is assembled at ORNL. The problem with the dressed-spin coils is that they will induce eddy currents in metals with a resultant heat load on the cryogenics. In fact, two dress-spin coils are being used in order to partially cancel the RF magnetic field on the surface of the ferromagnetic shield and thereby the eddy currents.

^{3}He Processing (WBS 1.4)

The life cycle of the polarized ^{3}He atoms in the EDM experiment consists of their production in an atomic beam source (ABS), their injection into LHe and storage, their transport into the measurement cell, their eventual depolarization, and their removal from the system. Most of these operations employ upper-cryostat equipment illustrated in Figure II-1. Details are available in the subsystem description.

The ABS is a quadrapole filter that focuses one polarization and defocuses the other one. ^{3}He atoms are injected into the filter from a 1 K volume of ^{3}He through a nozzle aimed along the axis of the filter. Large vacuum pumps remove the unwanted polarization state. The performance of this source is measured to be 10^{14} atoms/s with 99.6% polarization. This flux allows the desired concentration to be accumulated in 300 s.

The ABS is tilted at 45° to the horizontal in order to inject the beam into a 500 mK bath of ultrapure LHe. The exit of the ABS is designed so that the trajectory of the ^{3}He atoms does not intersect any walls before it intersects the LHe. A magnetic-guide field maintains the polarization along the path. This field is tapered to provide adiabatic transport of the polarized atoms into the 10 mG holding field surrounding the collection volume.

The collection volume contains the 500 mK bath. The original sample of ultrapure LHe will be produced in a separate apparatus using McClintock's heat wind technique [11] The

collection volume is surrounded by a *cosθ* coil to provide a uniform (10^{-3}) holding field and prevent depolarization. The entrance to the collection volume is surrounded by a thin cesium metal ring to prevent a helium film from entering the ABS transition region. Entrance and exit of ^{3}He from the volume is controlled by valves. The entire ^{3}He system consists of volumes isolated with a variety of types of valves. These valves are a reliability and technical challenge, but their details are postponed to the subsystem description.

At the appropriate time, the collection volume is opened to the measurement cells. The ^{3}He atoms diffuse through the LHe through a tube surrounded by a polarization holding coil. After roughly 100 s, the concentration of ^{3}He atoms in the measurement cells is nominal, and valves isolate the two volumes. The ^{3}He in the collection volume and transfer tube is removed by opening these volumes to the purifier.

The polarized ^{3}He in the measurement cells is used for one or more measurement cycles. Eventually, it depolarizes beyond a preset threshold. The measurement cell is connected to the purifier allowing the ^{3}He to diffuse from the cell into the purifier. Once the measurement cell has the density of ^{3}He reduced by a factor of 100, it is isolated from the purifier.

The purifier takes advantage of a narrow temperature range between 300–600 mK where the velocity of the ^{3}He is sufficient for it to escape its binding to the LHe but the diffusion is still rapid. The purifier contains a high-volume absorption trap to collect the ^{3}He. The purifier also contains a film stopping mechanism to prevent LHe from contaminating the charcoal.

A number of aspects of the diffusive transport of the ^{3}He have yet to be proven but calculations on the diffusion give reasonable tube diameters and practical times. The backup is a mechanical bellows system for moving the entire volume of helium. The mechanical-bellows system requires some very challenging superfluid valves. The diffusive movement is the preferred system.

Measurement Cycle

Table II-1 lists the steps in a measurement cycle along with illustrative durations. The durations remain to be optimized to achieve maximal sensitivity once the UCN storage and ^{3}He relaxation times are known. The table assumes that the starting condition is that the upper and lower cryostats are free of both UCN and ^{3}He.

Table II-1.   The Steps in an EDM Measurement Cycle.

Step	Description	Duration (s)
1	Diffuse polarized ^{3}He atoms into the measurement cell	100
2	Illuminate the measurement cell with polarized cold neutrons to produce polarized UCN aligned with the ^{3}He atoms	1000
3	Apply π/2 pulse to rotate spins to be perpendicular to the magnetic field	10
4	Measure precession frequency measurements	500
5	Remove ^{3}He atoms from the cryostats by diffusion to the purifier	100
6	Reload the collection volume with polarized ^{3}He from the ABS	300
7	Return to step 1	N/A

Refrigeration (WBS 1.3)

The optimal operating temperature is expected to lie between 300–500 mK. The upper end of the range is desirable because it minimizes the sensitivity to the geometric phase systematic. The lower range is desirable because it maximizes the time between recharges of the absorption trap in the purifier. At temperatures much above 500 mK, two phonon upscattering of the UCN becomes a concern. The high thermal conductivity of superfluid helium makes it quite

difficult to consider running individual parts of the cryostats at different temperatures when they are connected by LHe.

The LHe is cooled to and maintained at the operating temperature by three refrigerators. The cool down from 4 to 1 K is managed by a pumped ^{4}He refrigerator. Below 1 K, the two dilution refrigerators (DR) manage the cooling. Two DRs are used to give adequate cooling power. Crudely, one can think of each DR being associated with one of the cryostats. Further details and the heat budget for the experiment are described in the cryogenic subsystem description.

Liquid helium is made from gaseous helium stored in external tanks outside the UCN guide hall by a helium liquefier. Except for plumbing and electrical services, the liquefier is a standard commercial unit. One of the tanks has sufficient capacity to hold the entire charge of ultrapure helium in case of a system warm up. The Hazard Analysis describes the safety features associated with the cryogenics as well as other hazards related to the construction and operation of the EDM experiment.

B. Expected Sensitivity and Systematic Effects

Sensitivity

Scintillation Signal Sensitivity

The EDM preproposal develops the arguments for the sensitivity of this experiment under certain assumptions [12, p. 140]. Those assumptions include:

(1) The backgrounds to the scintillation measurement are roughly 1:1 with the signal and have an exponential decay spectrum with a decay constant close to that of the bottle storage time.

(2) The polarizations in the problem are P(^{3}He) $\equiv P_3 \cong 1$, P(cold neutrons) $\equiv P_{cn} \cong 0.9$, and the P(UCN) $\equiv P_n \cong 0.96$. P_n exceeds P_{cn} because the polarized ^{3}He is preferentially absorbing the "wrong" spins-state neutrons during the filling process.

(3) The number of neutrons in the two cells combined is 0.86 $PV\tau$, where P is the combined UCN production rate, V is the volume of one cell (4000 cm^3) and τ is the neutrons in the apparatus, including ^{3}He absorption, beta decay, and wall losses, taken to be equal to the natural lifetime of the neutron or about 1000 s.

If the production rate is taken to be 1/cc/s, then the sensitivity to a frequency shift due to the electric field is 2.6 μHz per cycle, which translates to a 1σ sensitivity for the EDM of

$$5.1 \times 10^{-27} e \cdot cm \sqrt{\frac{days}{T}} \tag{II.5}$$

with T defined as the total live time of the experiment in days. This project intends to collect data for 300 live days over three calendar years, leading to a 1σ-sensitivity of

$$3.0 \times 10^{-28} \ e \cdot cm. \tag{II.6}$$

Three factors modify the result in Equation II.6. The UCN production rate expected at the SNS is 0.3/cc/sec and leads to a degradation. The particle ID can greatly reduce the background assumption (1) above. If the background is essentially eliminated, there is a factor-of-two improvement in the sensitivity [13]. In a background-free experiment, the measurement time should be extended relative the UCN filling time taken as equal in Equation II.5. This optimization should lead to another factor-of-two improvement [13]. Putting in these factors, the 1σ sensitivity becomes

$$1.4 \times 10^{-28} \ e\cdot\text{cm} \tag{II.7}$$

as the ultimate potential for this technique.

SQUID Magnetometer Sensitivity

It is necessary to use the [3]He precession signal to determine the average magnetic field affecting the UCN precession. Ideally, the field would be constant, however, there are changes due to finite shielding of ambient magnetic-field changes, and systematic fields due to leakage currents associated with the application of HV.

Because the [3]He and neutron magnetic moments are equal to within 10% and because the electric field does not affect the [3]He precession, it is only the difference in magnetic Larmor precession frequencies that needs to be known to high accuracy. The sensitivity per measurement cycle is 2.6 µHz that was derived for Equation II-5, so the minimum required accuracy on δB is

$$\delta B = \frac{2.6\mu\text{Hz}}{\left|\gamma_3 - \gamma_n\right|} = 800\text{fT} \tag{II.8}$$

per measurement cycle; practically, the accuracy on δB should be a factor of three smaller so that it does not contribute noise to the measurements.

The noise in a SQUID system has been analyzed in the preproposal [12, p. 143], and the condition in Equation II.8 translates into a noise criteria of

$$1.3\mu\Phi_0 / \sqrt{\text{Hz}} / \text{cm}^2 . \tag{II.9}$$

A Conductus-1020 SQUID has a noise level of $3\mu\phi_0/\sqrt{Hz}$, implying at least a 2 cm^2 pickup loop is required to attain the requisite signal-to-noise ratio. This calculation assumes that the [3]He polarization does not decay significantly over the measurement period.

Systematic Effects

This section addresses possible systematic effects that are "fundamental" as opposed to the usual concerns of external magnetic fields associated with reversing HV apparatus, etc. Of course, such effects can be important for the proposed experiment but will be largely suppressed by the internal [3]He comagnetometer. The issues discussed here lead to real differences in the effective magnetic field seen by the [3]He and UCN and have been described in more detail in the preproposal [12, p. 144].

Pseudomagnetic Field

The effective UCN potential is given in terms of the coherent scattering length of each spin state of every constituent in the measuring cell. In the case where the constituents are polarized, each spin state has a different potential; this energy difference creates a pseudomagnetic field. For polarized [3]He at a fractional concentration of 10^{-10}, the difference in the scattering lengths leads to a pseudomagnetic spin precession of 660 µHz when the [3]He polarization lies along the static magnetic field. Note that this frequency shift is not dependent on the electric field, and so is canceled by the two cells having opposite electric fields, but can introduce noise into the system if it varies between the two cells between fillings.

This rather large value is suppressed by a number of factors. First, the [3]He spins are flipped into the plane for the free precession measurement, so the average field seen by the UCN has near-zero average; the only contribution to the precession frequency is that due to the imprecision of the $\pi/2$ pulse. Achieving 5% accuracy for this pulse reduces the pseudomagntic precession to 33 µHz. Furthermore, the cells are filled with almost exactly the same [3]He density because both are filled from the same source, so the difference frequency is even smaller. The initial [3]He density is expected to be the same within 5%. Furthermore, the relative difference in

the π/2 pulse between cells can be accurate to within 1%. These various factors bring the pseudomagnetic precession frequency difference to less than 1 µHz, which is sufficiently below the expected accuracy of about 2.6 µHz per measurement cycle so that no extra noise will be introduced. However, the importance of comparing two cells filled from the same source is evident. The direct ^{3}He magnetic field and its effect on the UCN is too small to be of concern compared to the pseudomagnetic field.

Gravitational Offset and other Spatial UCN/^{3}He Differences

The density of UCN "sags" under the influence of the Earth's gravitational field because their kinetic energy is so low. The ^{3}He energy (effective temperature) will be around 0.3 K compared to 3 mK for the UCN, so the effect of gravity on the ^{3}He distribution is extremely small. The shift in center of mass of UCN in a storage chamber of height h was estimated in Reference [1], p. 93:

$$\Delta h = \frac{mgh^2}{3kT}. \qquad (II.10)$$

For $h = 10$ cm $T = 3$ mK, $\Delta h = 0.13$ cm. The principal concern is that, if there is a spurious field from leakage currents, the ^{3}He and UCN will not average it in the same way. The problem cannot be solved exactly because the leakage current distribution is unknown, but the effect can be estimated. The usual rule of thumb is that the current is assumed to flow in a ¼-turn loop around the cell. Assuming a current of 1 nA, which is likely achievable at low temperature, and the average displacement of the two species, the maximum systematic error of 10^{-29} e·cm is comfortably below the anticipated statistical limit.

A related concern is nonuniformity of the ^{3}He distribution due to wall interaction. The effort to detect a nonuniformity in the ^{3}He distribution in a test cell (by use of neutron tomography) shows no substantial effects. In fact, it is anticipated that the ^{3}He will be repelled by the superfluid/cell interface. Unlike the case of most atoms that experience a Van der Waals attraction, or even near chemical binding, to walls of storage cells, the case of ^{3}He in superfluid helium is special as suggested by anecdotal evidence.

Another concern is the effects of unavoidable small heat currents on the ^{3}He distribution. At our anticipated operating temperature of less that 0.3–0.5 K, these effects are extremely small, with the effect of heat decreasing as the temperature T^{-7}.

V × E Effects

The motional or $v \times E$ magnetic field introduces a problem because the UCN and ^{3}He atoms have very different average velocities. However, the motional field is randomly fluctuating because the velocity changes on subsequent collisions with the cell walls. The problem is discussed in Reference [14], Section 3.5.3, and in Reference [15], where it is shown that the effect is "quadratic" in that it is proportional to the square of the electric field. The conclusion is that, for a 50 kV/cm field, the electric field must reverse with an accuracy of 1% to maintain a systematic shift below 5×10^{-29} e·cm. The electric field reversal accuracy is easily met and checked with the Kerr-effect measurement. Another point is that in the range of expected operating temperatures, the ^{3}He move diffusively with an effective velocity very similar to that of the UCN so that the shift is the same for both species.

Geometric Phase Effect

The geometric phase effect is the magnetic field gradient interference with the $v \times E$ field. The recent discussion of the effect began in the context of the cylindrical geometry of the newly

completed ILL EDM experiment [16] The effect is illustrated in Figure II-6. For the UCN, the frequency shift has the form

$$\delta\omega = \frac{\gamma^2 \frac{\partial B}{\partial R} R^2 E}{c}. \qquad (II.11)$$

There is also a frequency shift for the ^{3}He, but the form is more complicated. Note that Equation II.11 has the unfortunate property of changing sign with the electric field reversal. The effect was recently studied in detail including rectangular geometry [1]. The conclusion is that the important magnetic-uniformity requirement to suppress this effect is along the precession-field direction. The effect is more significant in the ^{3}He and does not cancel with the neutron effect. The effect does cancel between the two cells to first order if the nonuniformity is symmetric about x = 0. For a 10 mG holding field, the nonuniformity across the cell needs to be 0.1 µG to minimize the effect on the sensitivity, a quite challenging requirement. Because the time between wall collisions for the ^{3}He varies with temperature due to the rapidly varying diffusion coefficient, the effect is quite temperature dependent as illustrated in Figure II-7. The figure illustrates the need to stay above 400 mK.
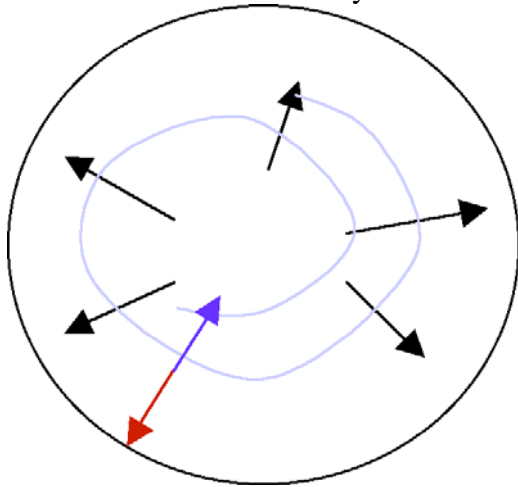
Fig. II-6. An illustration of the change in sign for the geometric phase effect. For $B_r = (\partial B/\partial r)r$, $v \times E$ changes sign (blue or red) with the direction of motion of the particle (light blue)
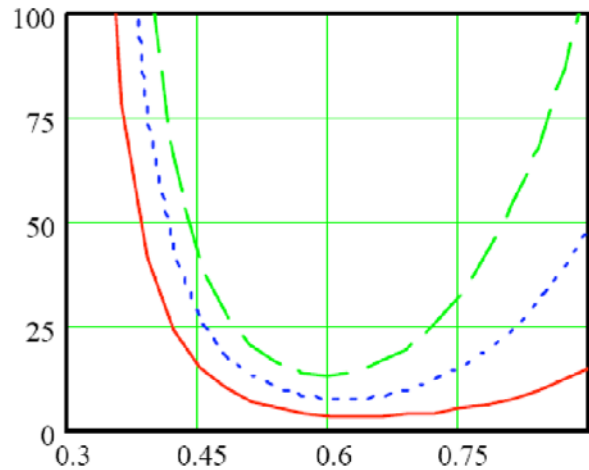
Fig. II-7. The relative temperature dependence of the geometric phase effect on ^{3}He. The red, blue and green curves are for 10, 20, and 30 cm cells

C. Project Specifications

Overarching Goal

The overarching goal of the EDM project is to construct an apparatus that will search for a nEDM with a statistical sensitivity and systematic uncertainty of 2.2×0^{-28} *e*·cm (90% CL). The collaboration has selected the cryogenic method of Lamoreaux and Golub [1] and sited the experiment on the UCN beam line of the FNPB at ORNL.

Principal Specifications

The principal specifications for measuring the performance of the nEDM experiment are given in Table II-2. Specifications are given at four times in the development of the nEDM Program:

(1)   at the completion of the R&D to be reviewed before critical decision (CD)-2 approval,

(2)   before completion of the nEDM Project to be reviewed before CD-4 approval,

(3)   following the first engineering run of the experiment and well after completion of the nEDM Project when the minimal performance specifications should be met, and

(4)   at the time of publication when the optimal performance specifications are needed to obtain the ultimate sensitivity.

The object of the nEDM Project is to construct an apparatus that will meet these specifications at each stage of the project and scientific program.

The specifications for all rows in Table II-2, except for the one identified as the *sensitivity*, are viewed as guidance. The sensitivity of the experiment depends on the product of the other performance specifications in a complicated way. The overall sensitivity is the principal measure of the physics reach of the apparatus and is the main criterion used to for CD-2 and CD-4 approvals. The sensitivity will be reevaluated before CD-2 based on the results of the R&D using the same methods utilized to project the optimal result.

The specifications for the EDM project have been broken into two sets, those which are directly used for the CDs and those that support obtaining of the overarching goal. This division is somewhat arbitrary, but the principal specifications are the most crucial for success. Many of the specifications cannot be known until a considerable amount of operations have occurred. The supporting specifications serve to document the design parameters for the collaboration.

The column labeled minimal performance is designed to be roughly the performance that would allow a sensitivity of $10^{-26}\,e{\cdot}\mathrm{cm}$ to be obtained. The achievement of this level of performance in the categories combined with no known limitation to approach the optimal performance will be the first goals of the collaboration. The optimal performance is the expectation after the engineering run.

The various parameters are not independent of one another. For example, the ^{3}He relaxation time has a much greater effect when it becomes shorter than the UCN wall loss time. Thus, a direct coupling to the overarching goal is not straightforward. The minimal performance is chosen to crudely represent a loss of a factor of two in sensitivity relative to the optimal goal, with the idea that 7 such losses of a factor of two would degrade $10^{-28}\,e{\cdot}\mathrm{cm}$ to $10^{-26}\,e{\cdot}\mathrm{cm}$.

Table II-2.   The Specifications for the nEDM Experiment [a]

Description	R&D [b]	CD-4 [c]	Minimal	Optimal
		Performance		
Operating Temperature (mK)	N/A	500 [d]	300–550	300–550
UCN Wall Loss Time (s)	1,000	100 [e]	200	2,000
⟨photoelectrons⟩/750-keV-ionization	20	4 [e]	12	40
^{3}He-Spin Relaxation Time (s)	1,000	200 [f]	200	30,000
Polarized ^{3}He Density in Cell (atoms/cm^3)	10^{12}	10^{11} [f]	3×10^{11}	10^{12}
^{3}He Polarization (%)	90	70 [f]	80	99
Purifier Concentration Fraction	2×10^{-12}	10^{-11} [f]	3×10^{-12}	10^{-12}
^{3}He Diffusion Time (s)	N/A	500 [f]	200	100
Valve Reliability (cycles)	6,000	500 [f]	3,000	20,000
SQUID Noise ($\mu\phi_0$)/$\sqrt{Hz}$	5	100 [e]	20	1
Electric Field (kV/cm)	40	5 [e]	25	50
Magnetic Gradient $\langle \delta B_x/\delta x \rangle_{vol}$ (μG/cm)	0.02	0.1 [g]	0.05	0.01
Shielding Factor from Conventional Shield	N/A	10^{-4} [g]	10^{-4}	2×10^{-5}
8.9-Å Neutron Flux (n/Å/cm2/s/MW)	N/A	5×10^5 [d]	2×10^6	8×10^6
8.9-Å Neutron Polarization (%)	N/A	70 [d]	80	90
Sensitivity at 90% CL (10^{-28} e·cm) [h]	30	300	300	2.2

[a] The minimal performance is the first goal of the collaboration following project completion and the optimal performance is needed to reach the ultimate sensitivity

[b] Conditions not identical to the full experiment

[c] Performance determined in full subsystem tests that may be outside of the main cryogenic vessel. The sensitivity will be the main criterion to be used for CD-4 acceptance.

[d] Measured at ORNL

[e] Measured at LANL

[f] Measured at LANL or Illinois – site to be determined

[g] Measured at Caltech

[h] The best estimate of the projected sensitivity based on all available information

Supporting Specifications

The supporting specifications are shown in Table II-3. The columns have the same definitions as for the principal specifications.

Table II-3. The Supporting Specifications for the nEDM Experiment.

Description	Minimal Performance	Optimal Performance
Total Experiment Live Time (yr)	0.3	1
Total Cooling Power at 450 mK (mW)	25	50
Cool Down Time (d)	28	14
Polarized ^{3}He Loading Time (s)	1000	100
Injection ^{3}He Polarization (%)	90	99.5
Maximum ^{4}He Purity (10^{10} atoms/cm^3)	10	1
Valve Lifetime (cycles)	5000	10^5
Particle Identification Rejection	1	50
Magnetic Shielding Factor	10^4	10^5
Eddy Current Heating at 4 K (mW)	1000	100
Uniformities of Other Magnetic Fields	5×10^{-3}	10^{-3}
Coil Power Supply Ripple	10^{-6}	10^{-7}
Coil Winding Precision (mm)	5	1
Alignment of E and B Fields (deg)	3	0.5
Electric Field Spark Rate (/yr)	0.5	0.1
Electric Field Uniformity	10^{-2}	10^{-3}
Personnel Radiation Field (mR/hr)	0.2	0.2

CD-4 Requirements

The attainment of the CD-4 requirements will demonstrate that all of the crucial functions of the apparatus work at a level where there is a reasonable probability that the scientific goals of the project will be reached. The following list elaborates on the numbers in the CD-4 column of Table II-2. The evaluation of the sensitivity for CD-4 approval requires both measurements at the time of the full system tests (before final assembly) from a variety of locations and assumptions about the performance in the full apparatus. The CD-4 requirements are preliminary and will be updated based on the R&D results before CD-2.

The CD-4 deliverables needed to complete the nEDM Project are

Cryogenic vessel installed at ORNL
• Demonstrated to cool the central detector volume to 500 mK
• Operated with the magnet coil package, central insert and ^{3}He services in place

Central detector insert installed and cryogenically integrated at ORNL but the following requirements met at LANL
• High voltage holds ≥5 kV/cm with a leakage current <10 nA
• Mean number of photoelectrons from 750 keV of energy deposition is ≥4

- SQUID noise $<100\ \mu\Phi_0/\sqrt{Hz}$ in 10 Hz bandwidth that, based on independent tests, implies a S/N>1
- Neutron storage time in similar cell demonstrated to be >100 s in an independent test

Magnet coil package installed and cryogenically integrated at ORNL
- $<dB/dx>/B_0 <10^{-5}$/cm at 77 K achieved at Caltech

Four-layer magnetic shield in storage at Caltech or ORNL
- Shielding factor of 10^{-4} achieved at Caltech

The shields will be installed post project at a time when needed technically. Premature installation will endanger the shields and delay progress towards science because they would be a hindrance to other required operations.

^{3}He services installed and cryogenically integrated at ORNL but the following requirements met at LANL or Illinois
- Produces $\geq 10^{11}$/cm^3 of $\geq$70%-polarized ^{3}He in the collection volume as seen with a SQUID
- Purifier reduces the ^{3}He concentration to less than 1 part in 10^{11}
- ^{3}He demonstrated to move between volumes with a time constant of 500 s
- Valves shown to operate over 500 cycles

Neutron guides installed at ORNL except for the final two meters
- Flux out/MW $\geq 2 \times 10^6$ n/ Å /cm^2/s/MW @ 8.9 Å with a polarization $\geq$70%
- An evaluation of the overall sensitivity to be better than 300×10^{-28} e·cm

References

1. R. Golub and S.K. Lamoreaux, *Physics Reports* **237**, 1 (1994).
2. P. Ageron et al., *Phys Lett.* **A66**, 469 (1978);
   R. Golub et al., *Z. Phys.***B51**, 187 (1983);
   R. Golub, *J. Phys*. **44**, L321 (1983);
   Proc. 18th Int. Conf. on Low Temperature Physics, Pt. 3 Invited Papers (Kyoto, Japan), 2073 (1987);
   R. Golub and S.K. Lamoreaux, *Phy. Rep.* **237**, 1 (1994);
   R. Golub and J.M. Pendlebury, *Phys. Lett. A* **62**, 337 (1977).
3. S.K. Lamoreaux and R. Golub, *JETP Lett*. **58**, 793 (1993).
4. S.K. Lamoreaux, Institut Laue-Langevin Internal Report 88LAOIT, 1988, unpublished;
   J.M. Pendlebury, *Nuc. Phys*. **A546**, 359 (1992).
5. P.R. Hoffman et al., *Nature* **403**, 62 (2000).
6. J. Long, et al., [http://arxiv.org/abs/physics/0603231].
7. C.A. Baker et al., (submitted to *Phys. Rev. Lett.*) [http://arxiv.org/abs/hep-ex/0602020].
8. P.G. Harris et al., *Phys. Rev. Lett.* **82**, 904 (1999).
9. D.R. Rich, et al. *Nucl. Instrum. and Meth. A* **481**, 431 (2002);
   O. Zimmer, et al. *EPJDirect* **A1**, 1 (2002);
   C.D. Keith, et al. *Phys. Rev. C* **69**, 034005 (2004).
10. D.N. McKinsey, "PMT Test at LNe temperature," presented to the EDM collaboration, Raleigh, NC, March 2, 2006.
11. P.V.E. McClintock, *Cryogenics* **18**, 201 (1978);
    P.C. Hendry and P.V.E. McClintock, *Cryogenics* **27**, 131 (1987).

12. A New Search for the Neutron Electric Dipole Moment, Pre-proposal submitted to the Department of Energy, by the EDM Collaboration 2002.
13. E. Van Cleve and M.D. Cooper, EDM Technical Note: Sensitivity of the Liquid He EDM Experiment as Derived from Least Squares Fitting of Pseudo-Data and Comparisons to the Heisenberg-Uncertainty Principle, LAUR-02-5924 (2002).
14. T.G. Vold et al., *Phys. Rev. Lett.* **52**, 2229 (1984).
15. S.K. Lamoreaux, *Phys. Rev. A* **53**, 3705 (1996).
16. J.M. Pendlebury et al. *Phys. Rev. A* **70**, 032102 (2004);
    P.G. Harris and J.M. Pendlebury, *Phys. Rev. A* **73**, 014101 (2006).

III. Research and Development

The plan for this EDM experiment was first expounded in Golub and Lamoreaux [1]. For a convincing case to be developed that the experiment was feasible, a vigorous experimental program was required to demonstrate the assertions in their article. This experimental program commenced with the granting of a LANL Laboratory-Directed Research and Development (LDRD) grant. The initial grant was modest but initiated R&D related to an atomic beam source (ABS) needed to produce highly polarized ^{3}He. LANL followed the first three-year grant with six more years of larger grants. LDRD grants largely cover salaries, but over the years roughly $1.6M of equipment money has been available to develop a systematic R&D approach. Additionally, several years of engineering and technician work (~$1M) has been covered by the LDRD. The LDRD money has been the backbone of the R&D program.

In 2002, the newly born collaboration wrote a preproposal to the Department of Energy (DOE) to describe the suggested project. Copies were also sent to the National Science Foundation. After favorable review, the DOE granted the collaboration $0.6M for preconceptual R&D and engineering. Following the granting of CD-0, the DOE gave another $0.18M to the project for R&D, conceptual engineering, and project development. All these funds have contributed to the extensive R&D program described here. The collaboration plans to supplement the previous funds with about $0.3M from DOE project funds and $0.5M of LDRD funds, including salaries for engineers and technicians, during 2007 to complete all R&D before the request for CD-2. The following description is by subject area and not chronological order.

Conceptual Engineering

At the beginning, it was unknown whether all the ingenious ideas in Golub and Lamoreaux could be incorporated into a single apparatus. A full three-dimensional (3-D) model for the first reference design of the apparatus was initiated. Only after several years of work was a comprehensive design formulated. The reference design has undergone a number of iterations. First calculations of the size of the cryogenic volume set the scale of the apparatus at about 1000 L of 500 mK LHe to maintain the stability of the electric field and the uniformity of the magnetic field.

The 3-D model has been crucial to the R&D because it is important to know how a piece of apparatus will fit into the full experiment before deciding the prototype to construct or the measurement to make. The 3-D model has been developed using the Unigraphics [2] program. The program can produce shop drawings, has sectioning capability, has a variety of rendering options, etc. This model is the conceptual design of the EDM experiment. All the figures of the apparatus in this CDR have been produced from the model.

A. Completed Work

Neutrons (WBS 1.2 and 1.6)

The Neutron Lifetime Experiment currently running at the National Institute of Standards and Technology (NIST) is a close cousin of this EDM experiment. There are a number of detailed differences, but there could hardly have been a better prototype for developing our experiment. The common membership of both projects greatly aided in the cooperation. One of the most important results was the verification of UCN production rate from cold neutrons via the superthermal mechanism. The formula for the UCN production rate may be cast in the form

$$P = 7.2 \frac{d^2\Phi^*}{d\lambda\, d\Omega} \frac{1}{\lambda_u^3} \delta\Omega \text{ UCN cm}^{-1}\text{s}^{-1} \tag{III.1}$$

was verified to better than 25% [3]. This development allowed for the accurate prediction of the UCN density in the EDM measurement cell.

In order to make optimal use of the output of the FNPB, the two EDM cells need to be symmetrically populated with highly polarized (>90%) cold neutrons. A ballistic guide coupled to the proposed polarizer splitter matched the needs quite well. The ballistic guide changes the phase space of the beam to one where the cold neutrons are largely below their critical angle. Thus, losses due to the finite reflectivity for angles corresponding to $m > 1$ (the reflectivity at $m = 3$ is 80%) are avoided. The collaboration modeled the combined system and determined the transmission and polarization out of the polarizer splitter. This work led to the FNPB adopting the ballistic guide for the UCN beam line and verified the applicability of the system to the EDM project. The expected transmission is 40%, and the predicted polarization is >90%.

The contributions to the neutron storage time, τ, in the absence of ^{3}He are

$$\frac{1}{\tau} = \frac{1}{\tau_n} + \frac{1}{\tau_h} + \frac{1}{\tau_w} + ..., \tag{III.2}$$

where only the contributions from the neutron lifetime (~900 s), holes in the cell, and losses on the walls are explicitly shown. The quantity of interest is the losses on the walls, where a large value like 2000 s would be highly desirable.

The collaboration takes advantage of the solid deuterium source of UCNs under development at Los Alamos for a measurement of the *A*-correlation coefficient in neutron decay (UCN/A). Extractable UCNs from the source are transmitted in vacuum to an acrylic bottle coated with deuterated styrene, the major component of the wall coating of the EDM cell. After filling the bottle for several hundred seconds, the bottle is closed with a shutter. The beam is closed off, and after a period of time, the shutter is reopened in order to count the number of neutrons remaining in the bottle. By varying the period between closing and opening the shutter, the number of neutrons vs delay time is fit with an exponential to extract the storage time. The wall losses are expected to be temperature dependent and to improve at low temperatures. This effect was observed. The results at 20 K to date have been $\tau = 324 \pm 106$ s. This value is consistent with the neutron lifetime and a 125 μm gap in the bottle around the shutter. Only a rough upper limit on the wall losses can be made because the statistics acquired is limited by the source production. We plan further measurements with an improved shutter mechanism having a smaller gap.

Magnetometry (WBS 1.5 and 1.6)

The noise from a SQUID contained in a superconducting lead shield has been measured with a Conductus-1020 in a configuration relevant to the task of detecting the ^{3}He magnetization. The result at 20 Hz is 2 $\mu\phi_0/\sqrt{Hz} = 4 \times 10^{-21}$ Tm$^2/\sqrt{Hz}$ at 4 K under the load of a pickup loop. The noise is expected to vary as the square root of the temperature. The effect is shown in Figure III-1. The noise at 0.5 K is consistent with the requirements of the experiment. The apparent offset from the origin is not completely understood.

The expected signal has been simulated with low field NMR on unpolarized hydrogen in a water sample. A driving signal is applied to the water and the relaxation signal is observed with a SQUID. The Fourier transform of the relaxation is shown in Figure III-2. The signal from the unpolarized water is estimated to be about one-tenth that from the 99%-polarized ^{3}He in the EDM cell.
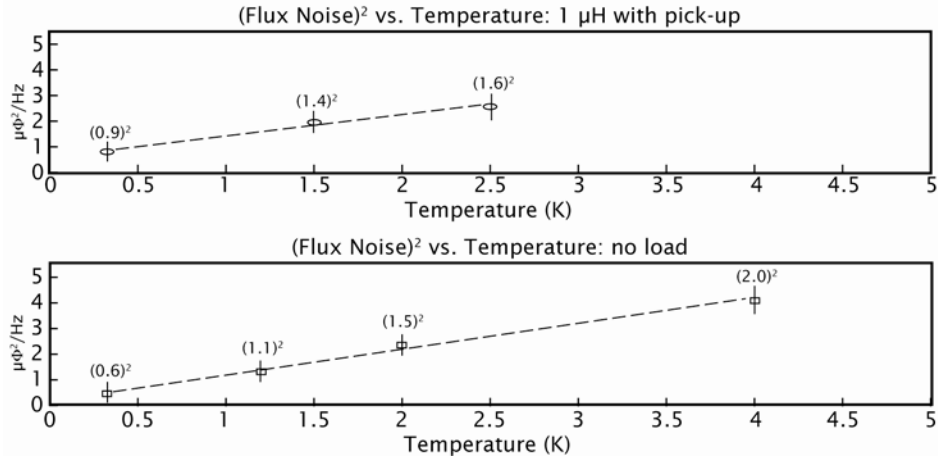
Fig. III-1.   The flux noise from a Conductus-1020 SQUID under load. The $T^{1/2}$ dependence of the noise is demonstrated.
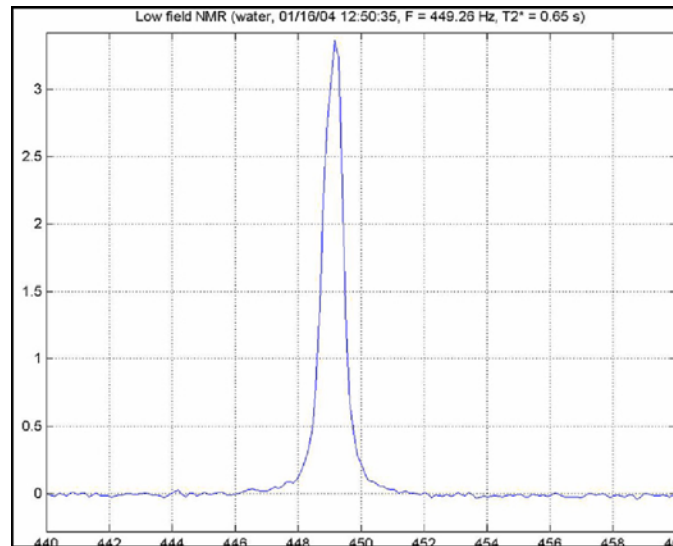

Fig III-2.   The magnetization signal from unpolarized water produced by the spin relaxation induced by a driving pulse. This signal is smaller than expected from the ^{3}He in the experiment.

The recently completed EDM experiment at the ILL uncovered the importance of the geometric phase effect. Our collaboration has studied the effect in detail [4]. The results have been discussed elsewhere in the CDR, but the most important result is that the effect on the ^{3}He is quite sensitive to the temperature, implying that the operating temperature should be adjusted to be about 0.5 K.

The dressed-spin method for measuring the EDM is discussed the section associated with magnets and magnetic shielding. More details are found in Golub and Lamoreaux [1]. The challenge of the dressed spin technique arises from the heat generated by eddy currents in the HV electrodes and the ferromagnetic shield. The problem in the electrodes is minimized by using a poor conductor to coat the surface of the HV electrode. This coating is also good to minimize Johnson noise in the SQUIDs. The heating in the ferromagnetic shield is minimized by using two coils of opposite field directions whose sizes are adjusted to produce the proper RF field in the cells but to cancel in the shield.

Electric Field (WBS 1.6)

The electric field has been modeled to determine the geometric parameters of the cell electrodes and the effect of the measurement cell walls that have a different dielectric constant from LHe. The principle results are (1) the ground plane surrounding the electrodes needs to be 30 cm from the edge of the HV electrode to prevent breakdown, setting the scale for the innermost part of the apparatus and (2) the edge of the HV electrode must have a radius of 5 cm to prevent breakdown, setting the separation between the cells and the neutron guides.

The Kerr effect is the change in ellipticity of a polarized laser beam as it passes through a medium in a strong electric field. For linearly polarized light entering a cell, the ellipticity, ε, is proportional to the square of the electric field, E:

$$\varepsilon = (\pi L/\lambda)KE^2, \tag{III.3}$$

where L is the path length of the beam and λ is the wavelength of the light. The proportionality constant, K, is known as the Kerr constant and is expected to be small for LHe due to the small electric polarizability of helium.

The Kerr effect is applied to the EDM experiment as a method of measuring the electric field between the cell electrodes. It may be especially useful to verify the accuracy of reversing the electric field. The method requires knowing the Kerr constant, which had not previously been measured. Our collaboration has measured it to be $(1.43 \pm 0.02^{(stat)} \pm 0.04^{(sys)}) \times 10^{-20}$ (cm/V)^2 [5]. The value is about three orders of magnitude smaller than liquid nitrogen. The value is independent of temperature. The quadratic dependence is shown in Figure III-3. The measurement time is 500 s in a cell with an effective length of 3.2 cm. This time will become shorter for the longer path length planned in the EDM apparatus.
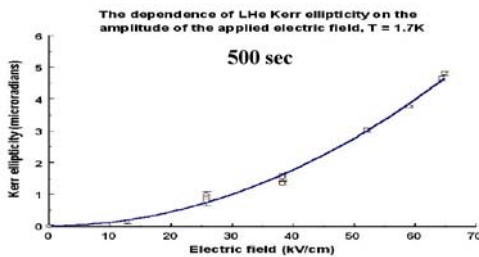
Fig III-3. The Kerr ellipticity vs electric field for LHe. The quadratic dependence is evident in the data. The curve is a fit to the data used to extract the Kerr constant for LHe.
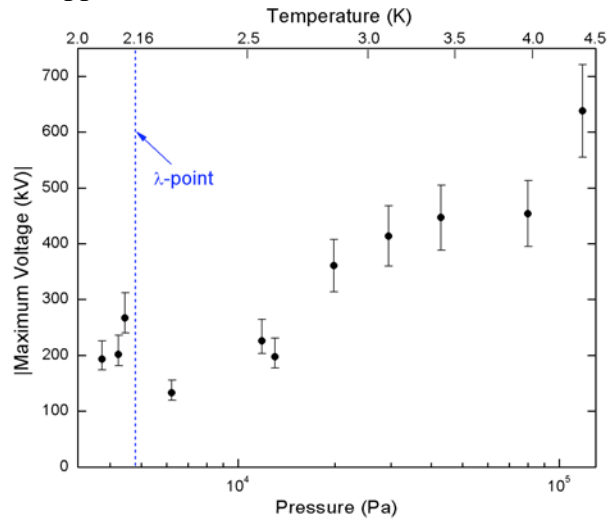
Fig III-4. The breakdown potential of LHe as a function of temperature.

The HV multiplier used to generate a 50 kV/cm electric field across the measurement cells was suggested to the collaboration following a seminar [6]. The idea is to connect a set of fixed electrodes to a variable capacitor, charge the variable capacitor when the plates are close together, disconnect the power supply, and mechanically increase the distance between the variable capacitor plates. As the plates are separated, the charge is conserved and the field between the measurement electrodes is multiplied. The technique has a number of advantages. It avoids attempting to charge the plates directly to 350 kV, which usually requires a heavy cable that is incompatible with cryogenics. It allows the use of readily available commercial

feedthroughs to transition from air to vacuum to LHe. It isolates the electrodes from power supply instabilities during the measurement.

The collaboration has constructed a test apparatus to test the variable capacitor method and to measure the dielectric strength of LHe, i.e., the breakdown voltage. The literature has a number of measurements of the dielectric strength of LHe, but all are for gaps of less than 1 cm and for very small area electrodes. In our case, the gap needs to be variable from 0–1 cm to 7–10 cm, and the plate area needs to be comparable to the cell electrodes; the plate radius has been chosen to be 20 cm. The small gap data suggests that the breakdown will scale as the square root of the gap. Indeed, the breakdown voltage at 4 K scales just a bit better than the square root of the gap. The value obtained is about 600 kV for a 7.5 cm gap. A measurement vs temperature shows that the breakdown voltage worsens as the temperature and pressure are reduced. This effect, shown in Figure III-4 down to the λ point, is still under study.

Light Collection and Particle Identification (WBS 1.6)

The light from the stopping of a charged particle in LHe arises from the decay of helium molecules. The prompt peak comes from the rapid decay of singlet molecules. Afterpulsing is due to the de-excitation of triplet molecules from their interaction with each other. The afterpulsing has a long time constant and is more prevalent for more highly ionizing decay products because these ions form molecules in a smaller volume. Afterpulses are single-photoelectron counts, and if they are detected in the first 10 µs following the prompt signal, they provide a method for improved particle identification of the stopping ions. In particular, the ^{3}He(n,p)t absorption process can be distinguished from both neutron β decay and Compton-scattered γ rays from cold-neutron capture and delayed decay, both backgrounds to the EDM measurement.

The collaboration mounted an experiment on a cold-neutron beamline at the Hahn-Meitner Institute in Berlin to compare the ionization signal with and without ^{3}He in the LHe. The results are shown in Figure III-5. The mean area of the prompt peak corresponds to roughly 40 photoelectrons. The afterpulses are collected for 10 µs following the prompt peak. The mean number for electrons is roughly 2, and the mean number for absorption events is roughly 6. The plot makes the need for good photoelectron statistics evident.

If the particle ID is highly successful at removing backgrounds, the sensitivity of the experiment is improved in two ways [7]. Firstly, the precision of the extracted phase of the neutron signal is better. Second, the counting time in a background-free regime may be increased relative to the filling time for the cells.

Magnetic Fields and Shielding (WBS 1.5)

A cosθ magnet is appropriate to produce a horizontal magnetic field in a cylindrical cryogenic vessel. The magnet has been modeled to determine the size of the magnet needed to produce a uniform field over the volume of the measurement cell. The result is that the magnet needs to be greater than 2 m long.

The superconducting shield is required to isolate the SQUIDs from the magnetic background outside the experiment. The superconducting shield produces the wrong boundary conditions for the cosθ magnet. The correct boundary conditions are provided if the magnet is wound inside of a ferromagnetic shield, which would need to be at a smaller radius than the superconducting shield. Unfortunately, most materials lose their permeability at LHe temperatures. The collaboration has tested some commercially available amorphous metals to use in a ferromagnetic shield. They maintain adequate permeability at the operating temperature of the experiment. The results for one such material, Metglas, is shown in Figure III-6.
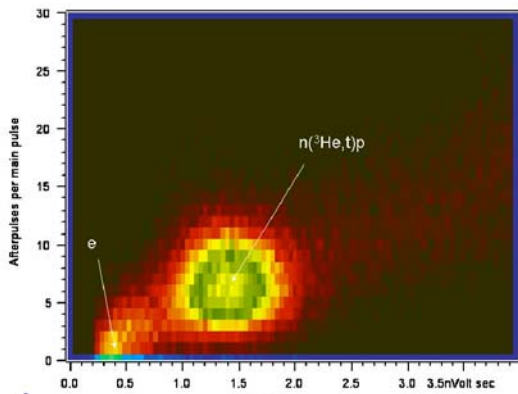
Fig. III-5. The number of afterpulses vs the area of the prompt scintillation peak. The electrons are clearly distinguished from the neutron-absorption events.
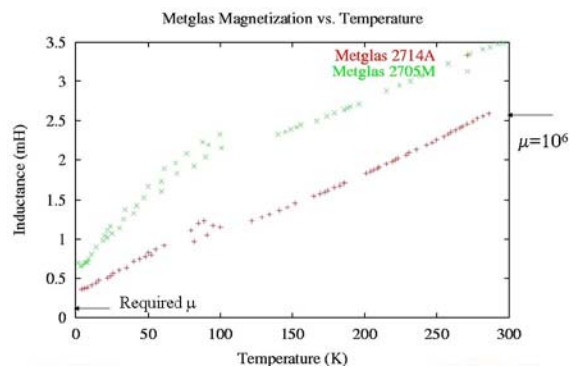
Fig. III-6. The permeability of two types of Metglas, amorphous metals, as a function of temperature. The required permeability is maintained at LHe temperatures.

The conventional cosθ magnet has coil wires on the ends. The end wires make it very difficult to bring in the required services for the central detector, e.g., the HV, the neutron guides, or the light guides. A variation of the cosθ magnet is the saddle shaped coil, where the longitudinal wires run along the same path as those in the conventional magnet, but the end wires are wound on the cylinder. This arrangement leaves the ends open. A saddle-shaped coil is illustrated in Figure III-7.

The collaboration has constructed a prototype saddle-shaped coil and measured the uniformity of the magnetic field. The result is shown in Figure III-8. This first attempt did not produce the required uniformity but has been judged a good starting point for developing the required uniformity. Note that the uniformity improves with the inclusion of Cryoperm, another amorphous metal product.
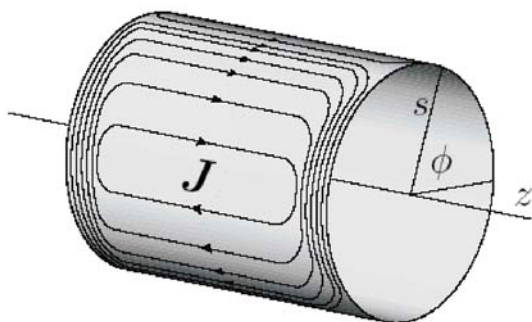
Fig. III-7. An illustration of the windings of a saddle-shaped coil.
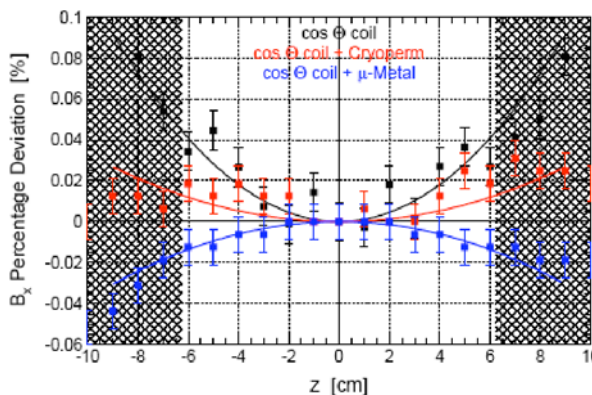
Fig. III-8. The uniformity of a saddle-shaped cosθ coil wrapped inside different shields.

^{3}He Processing (WBS 1.4)

Many important properties of the ^{3}He processing depend on the interactions of the atoms with phonons in the LHe. The number of phonons in the LHe is very strongly dependent on temperature so that the mean free path between interactions is very short at temperatures above

1 K and quite long (of the order of the dimensions of the volumes in the experiment) at 400 mK. In the usual two fluid model of liquid ^{4}He below λ point, in which liquid ^{4}He comprise the superfluid component and the normal component, the normal component carries thermal energy as a pure phonon gas. Therefore, the ^{3}He diffusion coefficient can be related to the isotopic concentration of ^{3}He and the velocity of the normal component of liquid ^{4}He as follow:

$$Xv_n - D\nabla X = 0, \tag{III.4}$$

where, X is the ^{3}He concentration, v_n is the velocity of the normal component of ^{4}He, and D is the diffusion coefficient. It follows that in the presence of a known heat source and a known heat sink, which determine the heat flow and therefore the flow of the normal component, the spatial distribution of the ^{3}He atoms depends only on the diffusion coefficient D. Therefore it is possible to determine D by measuring the spatial distribution of ^{3}He.

The collaboration has measured the diffusion coefficient as a function of temperature in the range from 0.45–0.95 K using neutron tomography [8]. A highly collimated beam (2.5 mm FWHM) of cold neutrons passes through a cylindrical volume of LHe with $X = 10^{-4}$. A small fraction of the cold neutrons are absorbed by the ^{3}He producing protons and tritons that are detected via the same methods to be used in the EDM cells. The number of counts per neutron is proportional to the path length of the beam through the ^{3}He. The beam passes near a resistive heater in the LHe. The heater produces phonons that radiate away from this source, and the phonon/^{3}He interaction produces a liquid region deficient in ^{3}He whose size is proportional to the intensity of the heat source. Thus, the larger the heat source, the greater the size of the bubble and the smaller the signal of neutron absorption. The correlation between heater power and light output has been analyzed to extract the diffusion coefficient.

The results of the data analysis are shown in Figure III-9. At temperatures below 0.7 K, the diffusion coefficient varies as T^{-7} as predicted for interactions dominated by single phonons. From observation, the distribution of ^{3}He atoms in the EDM measurement cell is uniform below 0.5 K. This result is crucial to the magnetometry, where a nonuniform distribution would imply that the ^{3}He would not be sensitive to the same magnetic field as the UCN.

At temperatures above 1 K, the phonon interaction with the ^{3}He is sufficiently strong that a heat source at one end of a capillary tube can completely impede the flow of ^{3}He. This observation is the basis of the "heat-flush" method for purifying ^{4}He [9]. The collaboration has used this process to produce ultrapure ^{4}He in a cryostat built at the Hahn-Meitner Institute. The production rate is a few cc/min of liquid. The initial sample has been analyzed with accelerator mass spectrometry at Argonne National Laboratory. The concentration is $X < 10^{-12}$. This device is one option the collaboration has to produce its initial 20 L charge of ultrapure liquid ^{4}He.

An important simplification of the experiment has occurred since the measurement of the diffusion coefficient. Originally, the method for removing depolarized ^{3}He was to physically move the LHe to a region where it could be warmed above 1 K and purified with the heat-flush method. This method required many moving parts and put a tremendous heat load on the dilution refrigerators.
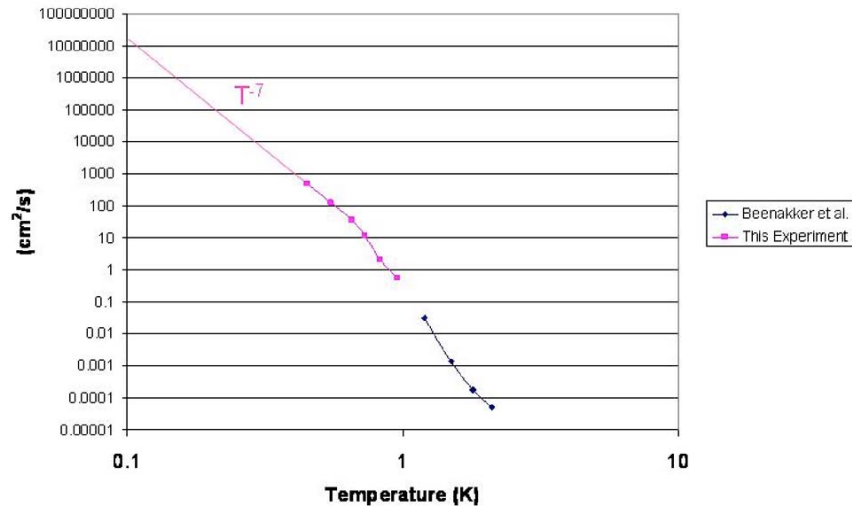
Fig. III-9.   The ^{3}He diffusion coefficient in ^{4}He. The data above 1 K comes from one of the lowest-temperature previous measurements. At the lowest temperatures, the dominant interaction is with single phonons that produces the T^{-7} dependence.

The current reference design allows the ^{3}He to move diffusively from regions of relatively high concentration ($X \sim 10^{-10}$) to regions of relatively low concentration ($X \sim 10^{-12}$). If the regions are connected with a 2-cm-diameter pipe, the time to transfer the ^{3}He is estimated to be around 100 s. The low concentration region is where the ^{3}He is removed by an evaporative purifier that is under development.

The initial supply of highly polarized ^{3}He atoms is produced by an atomic beam source (ABS). The ABS consists of a small volume of 1 K ^{3}He that feeds atoms through a nozzle into a 1-m-long magnet. The magnet is made from a series permanent magnets arranged to from a quadrupole. The magnet focuses one spin state into a beam and defocuses the other one into the background gas. The system removes the background gas with very high performance pumps.

The separation phase is matched with an identical quadrupole magnet that serves as a beam analyzer. In the gap between the two magnets, a spin rotating magnet allows for the polarization to be measured by comparing spin-flipped to non-spin-flipped transmission. The transmitted ^{3}He are detected downstream of the analyzer section with a residual gas analyzer. This spectroscopy has demonstrated a polarization of (99.6 ±0.25)%. The production rate of polarized ^{3}He is 10^{14} atoms/s with good emittance and an average velocity of 150 m/s. This production rate provides the required ^{3}He within a few hundred seconds.

The collaboration has made a preliminary measurement of the relaxation time of polarized ^{3}He in an acrylic cell coated with dTPB. At 1.9 K, the relaxation time is about 2000 s. This experiment must be repeated at 500 mK.

Refrigeration (WBS 1.3)

The collaboration has purchased a dilution refrigerator (DR) with the greatest cooling power that is commercially available. In its proof test, the DR produced a cooling power of 3.6 mW at 120 mK. The cooling power scales as T^2, so that at 500 mK, the cooling power is roughly 60 mW. This value is being used in the reference design, but by making plumbing changes that optimize the cooling power at 500 mK instead of 100 mK, another factor of two in performance can be expected.

B. Continuing Investigations

Despite answering the most crucial question of feasibility for this technique, the R&D program must continue to move the design from its conceptual phase to an optimized preliminary design. The collaboration proposes to use part of the project funds to finish the R&D by the end of calendar year 2007 in time for the scheduled CD-2b review described in the PPEP.

Neutrons (WBS 1.2 and 1.6)

An unanswered question is the optimal method to build the magnet for the holding field of the splitter-polarizer. The difficulty is near the intersection point of the two transmission mirrors where the field is in principle supposed to go in opposite directions along the same line. Clearly, there needs to be a small collimated region where the cold neutrons are absorbed. The collaboration will undertake a study with a finite-element analysis (FEA) code to decide on the size of the dead region and on the character of the magnet to produce the best holding field.

The neutron storage-time measurement described above is incomplete. A new shutter arrangement has been designed that hopefully will remove the hole where neutrons leak out around the shutter. Depending on the performance of the solid-deuterium UCN source, data with better statistics and no losses around the shutter should be taken during July, 2006.

Magnetometry (WBS 1.5 and 1.6)

By adding a solenoidal RF coil between the separator and analyzer sections of the ABS, the ^{3}He dressed spin has been measured. The data allows for the detection of deviations from first-order theory. The data has been taken and is under analysis. The effect of the RF coils on the polarization is also being analyzed.

The geometric phase effect requires a very stringent magnetic-field uniformity to eliminate this systematic. Furthermore, the effect does not cancel between the neutrons and ^{3}He. Due to their higher velocity, their influence on the ^{3}He is more severe. The rapidly varying diffusion coefficient makes the effect quite temperature dependent. A small apparatus is under construction to measure the geometric phase effect as a function of temperature by applying an exaggerated field gradient. The goal will be to validate the theory.

The collaboration has never observed a SQUID NMR signal from the precession of ^{3}He in LHe. An apparatus is being designed to observe the precession at a variety of concentrations below $X \sim 10^{-6}$. These tests will allow us to optimize the pickup loops and SQUID configuration for the experiment.

The cryostat to be used is in fabrication. A number of the parts have been received. It will have a number of other uses, including the testing of the evaporative purifier and the ^{3}He injection efficiency. With slight modification, it will also be usable to test the final ^{3}He components and the final central detector insert.

Electric Field (WBS 1.6)

As the configuration of the light guides in the central detector is becoming clearer, it is necessary to make detailed calculation of the electric field in the measurement-cell region to determine any nonuniformity in the electric field introduced by the addition of these dielectrics. The FEA program AnSys [10] will be used for the calculations.

A number of issues must be resolved with regard to the practical application of the Kerr effect to a full-scale system. The laser light must wind its way through the magnetic penetrations. The existing HV apparatus will be used to test the scheme.

Leakage currents along the acrylic walls of the cell can introduce an important systematic. Sheets of acrylic, both uncoated and coated with deuterated styrene, will be tested in the HV apparatus to measure the leakage current.

The electrodes employed currently in the HV apparatus are fabricated from Al. There are a several reasons why the electrodes should be made from acrylic coated with some form of carbon. It is necessary to learn the thickness of the carbon coating that is required to give the right amount of conductivity without supporting eddy-current heating or producing Johnson noise in the SQUIDs. New electrodes will be fabricated using a variety of coating techniques and tested in the HV apparatus.

The temperature dependence shown in Figure III-4 of the dielectric strength of LHe has been a surprise. One possibility is that the breakdown is dominated by frozen contaminants like air and pump oil. Procedures to clean the system more carefully are close to implementation. Another possibility is that the aluminum electrodes cause the problem. Even though polishing them has made no difference, the changeover to carbon-coated acrylic will provide an interesting test. Finally, the change in breakdown voltage can be due to the pressure in the liquid. A concept is on the drawing board of how to compress the LHe in the HV apparatus to see if the higher density recovers the highest breakdown potentials. Even if this last method works, its application to the real experiment introduces quite a bit of undesirable complexity to the operation of the device. The decision to use pressurization will only be made when the effect is better understood, especially below the λ point.

Light Collection and Particle Identification (WBS 1.6)

Recent simulations of the light guides that carry the emissions from the dTPB have given preliminary evidence that the best way to configure the light guides is for them to come out both the top and bottom of the cells. These simulations will continue as the preliminary design is established.

For the light to reach the outside of the cryostat, the light guides must have small breaks at the boundaries between 300 mK and 4 K, between 4 K and 70 K, and between 70 K and 300 K. Each of these breaks loses about 30% of the light. Recently, specially modified PMTs have been run successfully at 27 K in liquid neon [11]. The modification is to put a flash of metal near the photocathode to carry away charge buildup induced by the reduction in photocathode resistivity at low temperatures. The same technique should work at 4 K. The added complexity is the permeability of glass to room-temperature helium, which allows helium gas to destroy the vacuum in the tube. If the tube is kept in vacuum and the guide is part of the seal, the PMT should operate normally. The collaboration will build a small apparatus to test the performance of a single tube. If successful, an important factor of two in photoelectron statistics will be gained by eliminating the last two breaks in the guides.

A different approach that is in the process of being evaluated is visible-light photon counters (VLPC). By cooling both the VLPC and its preamplifier to LHe temperatures, early results show promising dark currents. Although VLPCs have high photoefficiency, they have small surface area. The application of VLPCs to the EDM light-collection problem will require a second wavelength shifter embedded in fiber optics that compresses the phase space of the light to match the VLPC. The measurement of the net gain or loss of photon statistics is nearing completion.

A novel method for improving the particle ID is laser-induced fluorescence to directly detect the triplet molecules. Laser light in the 1000 nm range floods the cell to drive the triplet decays. The PMTs are protected from this light with filters. The laser is triggered by the prompt signal. The strength of the triplet decay signal induced by the laser allows identification of the particles. This investigation is new, but the payoff could be substantial.

Magnetic Fields and Shielding (WBS 1.5)

Continued modeling of the cosθ coils is needed to optimize the design and field uniformity. A particularly promising approach is to superimpose two coils with different numbers of turns in order to have the nonuniformities cancel in the region of the measurement cells. These studies are in progress.

A prototype magnet will be constructed to understand the best construction techniques. It is planned to be of ¼-scale to the actual main field magnet. These techniques should be applicable to all the magnets. Once constructed, this magnet can also serve as the holding field coil for the ^{3}He injection tests described below.

^{3}He Processing (WBS 1.4)

All of the results from the ABS were obtained with the source horizontal. The plan for ^{3}He injection is to orient the source at 45° above horizontal so that the beam can be aimed directly at the surface of the LHe in the collection volume. This test is simple and no problems are anticipated, but an operational test in this orientation seems prudent to avoid a surprise.

Though we have obtained some reasonable ^{3}He relaxation times down to 1.9 K for a dTPB coated acrylic cell, the literature indicates that the relaxation time should be a strong function of temperature below 4 K. Hence, it is necessary to measure it at 500 mK. These measurements are well along and have a good chance of completing by the end of 2006. They will be followed by tests of some other materials that may be used in the cryostat.

The ^{3}He atoms are weakly bound in the LHe. They can only escape into a vacuum if their velocity is sufficient to overcome the binding energy. At low temperatures, their ballistic velocity is insufficient. Above about 600 mK, the diffusion makes their effective velocity insufficient. Hence, in a narrow temperature region, between about 100–600 mK, it may be possible to evaporative remove depolarized ^{3}He from the LHe to regain the ultrapure ^{4}He.

Plans are underway to construct a prototype evaporative purifier and test it over the allowable temperature range. The purifier consists of a vat of LHe shaped to give a large surface-to-volume ratio. The vacuum above the LHe is maintained with an absorption pump that removes the ^{3}He. The biggest anticipated problems are the lifetime of the absorber and the control of the superfluid helium-film flow. The lifetime of the absorber will be better at lower temperatures because of a lower ^{4}He vapor pressure, but this temperature may be too low for the operation of the experiment. Hence, there will be two absorbers to allow one to be regenerated while the other is in operation. The requirement is to keep the time between regenerations practical. The helium-film flow requires either a film burner or a ring of cesium near the top of the purifier.

The other major ^{3}He system to be tested is its injection into the LHe without loss of polarization. There are a number of elements to prove. The superfluid helium-film flow must be contained here too, and the reference design calls for a cesium ring near the transition region coupling the collection volume to the ABS. The transition region must have a magnet coil designed to shape the field between the ABS and the holding coil so that the spin precession is adiabatic and the polarization is preserved. Finally, the polarization and holding time in the collection volume need study. The cryostat for this test and for the evaporative purifier test is the same.

There are a significant number of valves needed to control the movement of the ^{3}He in the experiment. The actuation system may be similar, but the valve body must be specialized to the application. Some of the applications require a body that is superfluid tight, while others may be required to be neutron and polarization friendly. Over the lifetime of the experiment, as many as 10^5 cycles may be required. Hence, high reliability is a must. By the end of 2007, the

collaboration expects to prototype valves that meet all the requirements. The chapter on the ^{3}He subsystem expands on the requirements.

Measurement Cycle (WBS 1.3 and 1.7)

There is no in-principal problem with the slow controls for the experiment, but there are many environmental parameters to monitor and many devices to control. A number of solutions have been employed elsewhere. Because the typical timescale for changing the state of the apparatus is less than an hour, it is required to have an automated system for an experiment with a live time of one year. The collaboration intends to build a prototype system to establish a standard across the collaboration. As construction continues, this prototype will be extremely useful in testing all parts of the apparatus.

Refrigeration (WBS 1.3)

The cryogenics team is busily establishing a heat budget for each of the components. This exercise is important to set the limits for each piece of the apparatus and to make the evaluation that each piece can operate within its allocation.

It has been believed for some time that additional refrigerators would be required to cool and maintain the EDM experiment. The DR that is currently owned simply has insufficient cooling power. One of the additional refrigerators will be an evaporative ^{4}He device used to cool the large volume of LHe through the λ point. The other will supplement the original DR, and an evaluation is underway to decide between a DR and a ^{3}He refrigerator. Both of these refrigerators will be specified before CD-2a.

References

1. R. Golub and S.K. Lamoreaux, *Phys. Rep.* **237**, 1 (1994).
2. UGS Corporation, 5800 Granite Parkway, Suite 600, Plano, TX 75024.
3. I.B. Khirplovich and S.K. Lamoreaux, *CP Violation without Strangenes*s, (Springer-Verlag, Berlin, 1997).
4. S.K. Lamoreaux and R. Golub, *Phys. Rev. A* **71**, 32104 (2005) and
   A.L. Barabanov, R. Golub, and S.K. Lamoreaux, [http://arxiv.org/abs/nucl-ex/0512014].
5. A.O. Sushkov et al., *Phys. Rev. Lett.* **93**, 153003 (2004).
6. V. Sandberg, private communication.
7. E. Van Cleve and M.D. Cooper, EDM Technical Note: Sensitivity of the Liquid He EDM Experiment as Derived from Least Squares Fitting of Pseudo-Data and Comparisons to the Heisenberg-Uncertainty Principle, LAUR-02-5924 (2002).
8. S.K. Lamoreaux, et al., *Europhys. Lett.* **58**, 718 (2002).
9. P.V.E. McClintock, *Cryogenics* **18**, 201 (1978);
   P.C. Hendry and P.V.E. McClintock, *Cryogenics* **27**, 131 (1987).
10. ANSYS, Inc., Southpointe, 275 Technology Drive, Canonsburg, PA 15317.
11. D.N. McKinsey, "PMT Test at LNe Temperature," presented to the EDM collaboration, Raleigh, NC, March 2, 2006.

IV.   Polarized Neutron Beam Line and Shielding (WBS 1.2)

The UCN needed for this experiment are produced via the superthermal method [1]. The method takes advantage of the fact that the free-neutron dispersion curve crosses the phonon dispersion curve for LHe in two places, zero energy and 8.9 Å or about 1 meV (see Figure IV-1). Hence, the neutron/LHe system is analogous to a two-state atomic system, where the emission of a phonon allows the neutron to "de-excite" and be left with nearly zero energy. The UCN are created up to the phase-space depth of the well provided by the potential of the container. The UCN build up because losses by excitation are inhibited due to an absence of phonons; phonons are removed from the system by the refrigeration. Two-phonon "up-scattering" has a T^7 dependence and is very small at 500 mK. The production rate given in Equation III-1 has been verified experimentally [2]. At the FNPB, the production rate is expected to be 0.3/cm^3/s. If the storage time in the cell is 500 s, the expected density will be 150/cm^3. By comparison, most of the data from the most recent EDM search [3] was taken with a density of about 1/cm^3.
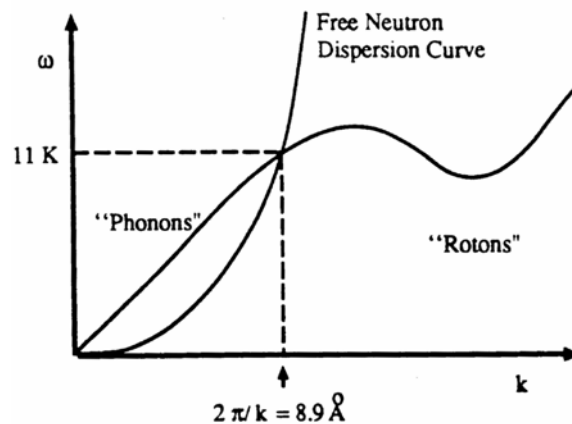

Fig. IV-1.   The dispersion curves for the free neutron and for LHe. The crossing at 8.9 Å is the magic wavelength for UCN production.

The FNPB is a set of two neutron guide systems dedicated to studies of fundamental properties of the neutron. On the UCN guide, the system is designed for monochromatic 8.9 Å neutrons to take advantage of the superthermal process. A system of monochromators selects neutrons with a wavelength of 8.9 Å. The cold neutrons must be transported and polarized within the 33 m distance to the EDM experiment. The first 18 m are part of a general neutron guide system provided by the FNPB project and the last ~15 m will be designed and constructed by the EDM collaboration. The EDM guide starts with a straight guide of 20 cm × 30 cm rectangular cross section. The guide walls are coated with a supermirror coating. This coating is specified by a quantity m which describes the enhancement in reflectivity compared to a nickel coating ($m = \theta/\theta_C$, where θ is the maximum incident angle for neutron reflection and θ_C is the critical angle for nickel (1.7 mrad/Å)). The losses increase with increasing m. Monte-Carlo simulations show that only ~40% of the incident neutrons can be transported through a 33-m-long guide if the cross section is 12 cm × 14 cm and m is 3.5 (original FNPB design). In order to reduce the number of wall bounces and the angle of incidence, the cross section has been increased to 20 cm × 30 cm with conically shaped transition guides at the beginning and the end of the beam line. Figure IV-2 shows a schematic drawing of the geometry. First simulations show that such a "ballistic guide" increases the neutron flux by up to ~75% as compared to a straight guide with smaller dimensions [4].
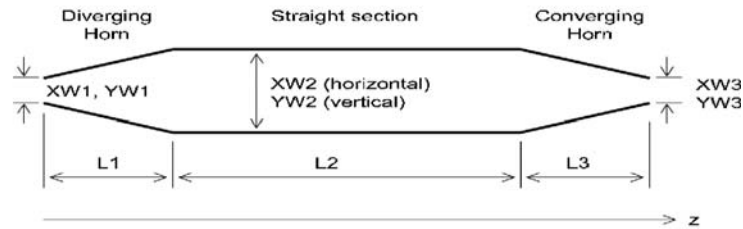
Fig. IV-2.   Schematic drawing of a "ballistic" neutron guide.

Details of the Simulation

The optimization of the ballistic guide has been performed using Monte Carlo (MC) simulation. Although there existed already a general MC code, the McStas program [5], a new ray-tracing package is used to specifically trace the 8.9 Å neutrons through the guide and the EDM beam polarizer/splitter. Neutrons are generated to match the phase space calculated by a McStas FNPB simulation for the neutrons coming out of the double crystal monochromator. The neutrons are then injected into the ballistic guide to simulate their behavior in the guide. The performance of various geometries has been evaluated. The transmission, i.e., the ratio of the number of neutrons exiting the guide to the number of neutrons entering the guide, and the relative transmission, i.e., the ratio of the transmission of the guide geometry under consideration to that of the 12 cm × 14 cm straight guide, are the optimization parameters. (Note that because the input to the ballistic guide is the same for all geometries, the relative transmission is the same as the output neutron flux or fluence normalized to that of the straight guide.) An improved geometry is a 'ballistic' guide with L1 = L3 = 9 m ($m = 3.5$) and L2 = 15 m ($m = 2$) (see Figure IV-2). Such a 'ballistic' guide shows an increase of ~75% in neutron transmission relative to the 12 cm × 14 cm straight guide ($m = 3.5$). However, the EDM experiment needs neutrons fed to two different target cells, implying that the guide must be split into two guides at the exit. Figure IV-3 shows the guide geometry with the beam divided into two outputs. Simulations to optimize the neutron fluence with the exact boundary conditions imposed by the EDM experiment are planned for later this summer.

The Polarizer

If all the neutrons can be arranged to enter the cells with their polarization direction aligned with the spins of the polarized ^{3}He, essentially no neutrons will be lost due to capture. Hence, a neutron polarizer has been incorporated in the beam line.

In order to produce polarized neutrons with polarizations greater than 95%, a neutron guide with internal magnetically remnant polarizing supermirrors is anticipated. Sputtering techniques have evolved to a level where multilayers of different materials can be fabricated over large areas with a high degree of perfection. The basic idea of such supermirror polarizers is to combine layers of magnetic alloys (such as Fe, $Fe_{0.89}Co_{0.11}$, or FeCoV) with layers of
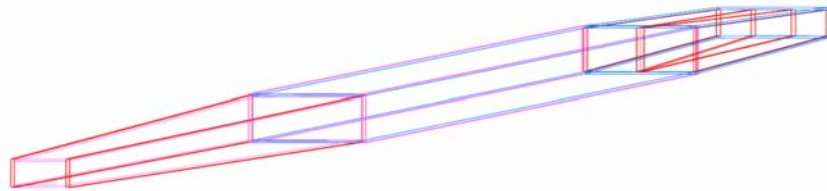

Fig. IV-3.   Neutron guide system for EDM experiment.

nonmagnetic materials (such as Si or TiN$_x$). An *m* value as high as 2.5 is achieved routinely. Because the scattering-length densities for magnetic materials depends on the spin direction of the neutrons, a proper combination of magnetized- and nonmagnetic-material layers causes large coefficients of reflection for one spin state and small coefficients of reflection for the other. Techniques exist to coat several hundred layers on silicon substrates (low-neutron-absorption cross section). The typical thickness for a layer is several tens of Angstroms. The ferromagnetic materials can be magnetized (in-plane) by external magnetic fields. These sheets will maintain high levels of magnetization with coercive fields that can withstand antiparallel fields of a few Gauss. Such systems have already been realized at laboratories like the HMI [6] and PSI [7]. A schematic of a possible design for the EDM experiment is shown in Figure IV-4.

Two planes of magnetized supermirrors, with their internal fields aligned in opposite directions, are aligned vertically in such a way that every neutron must pass through one of the polarizing sheets. A weak magnetic guide field is needed to define a quantization axis for the neutron spins to preserve their polarization. Depending on the spin orientation (up or down), one of the two supermirrors has a large coefficient of transmission and a small coefficient of reflection for one spin state and vice versa for the other spin state. This arrangement allows a separation of the two spin states. The highly polarized neutron beams are transported in nonmagnetic neutron guides to the target cells.

In order to realize this geometry, the last ~14 m of the beam line need to be equipped with a permanent magnetic guide field of a few Gauss (< 10G). Either a rectangular Helmholtz coil configuration or, more likely, a magnetic dipole field using permanent magnets in combination with field-shaping plates will be employed. However, if a permanent-magnet system is used, a separate magnet may be necessary to magnetize the supermirror polarizers. To polarizer standard supermirror guides, saturation fields of up to 200 G need to be applied for short periods of time (~1 s). Studies by P. Boeni et al. [6] indicate that a reduction in layer thickness amounts to lower saturation fields (as low as 30–50 G). The configuration shown in Figure IV-4 requires a magnetizing field pointing in opposite directions for each polarizer. This implies that the two sheets need to be separated by several centimeters in the vertex region (also to avoid large differential fields caused by local remnant fields).

Detailed GEANT4 MC simulations, including realistic reflections and transmission, will be performed with the goal of optimizing P^2T (where *P* is the neutron polarization and *T* is the transmitted flux). A set of GEANT4 C++ classes for neutron transport and UCN storage has been developed by P. Fierlinger et al. [8]. The program also tracks neutron spins through magnetic fields. The program has been made available to our collaboration. These classes will be used for optimization studies as well as a complete MC simulation of the whole experiment. The exact magnetic-field arrangement will be determined using finite-element analysis programs.
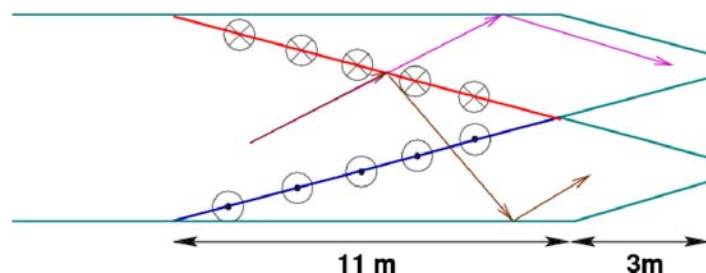

Fig. IV-4.　Top view of a possible polarizer design. The red and blue lines indicate magnetically remnant polarizing sheets with antiparallel magnetization. The arrows are possible neutron trajectories for neutrons with spin iton the plane (violet) and out of the plane (gold).

The Spin Flipper and Transition Field

The neutrons exit the polarizer with spins in the vertical direction (up or down). The magnetic field direction, and therefore the ^{3}He polarization direction, in the target cells is horizontal and is in the same direction for both measurement cells (given by the field direction of the $cos\theta$ coil). As described above, both neutron polarization states are intended to be transported by the guide system. Because the neutrons in each of the two splitter guides have opposite polarizations, one measurement cell would be filled with neutron spins parallel to the ^{3}He spins, while the other would be filled with spins antiparallel to the ^{3}He spins. To prevent rapid capture of the neutrons by ^{3}He in the antiparallel case, a spin flipper is needed for that guide (for symmetry, and possible systematic checks, spin flippers will be installed for both guides). In addition, magnetic fields to adiabatically rotate the neutron spins from vertical to horizontal are needed to get the spin direction matched to the measurement cells. One spin flipper and a spin-rotating transition field are needed for each arm of the guide. There are two practical types of RF flippers: a resonant one that requires neutrons to spend the right time in the RF field and one employing adiabatic fast passage, i.e., not a tuned device, but one that requires a static B field gradient. Simulations for each type of flipper have already been developed at IU for other projects.

Either type of spin flipper can work with high efficiency over a broad range of static fields and/or field gradients. The boundary conditions on the static field are set by the polarizer requirements and the need to match the field at the entrance to the apparatus. In an RF spin flipper, the coil needs an area where it can transmit the RF field to the neutrons without it being absorbed by metal. If this condition requires the coils to be located in vacuum, cooling for the RF coils may be needed. Alternatively, a part of the vacuum shroud for the guide in the RF flipper region could be made from ceramic.

Either type of RF spin flipper requires a sine wave generator in the 10–100 KHz range (depending on size and therefore Larmour precession frequency of static field), coupled to a RF amplifier which can be switched into either the beam line coil or a dummy coil of equal impedance with a high-power RF switch. The amplitude of the RF field should be at least a few Gauss over a volume of order $30 \, \text{cm} \times 30 \, \text{cm} \times 30 \, \text{cm}$. The required RF power depends on the Q of the resonant circuit and quality of impedance matching; a first guess for the RF power is a few hundred Watts per flipper. An impedance-matching circuit which does not spark at the high transient voltages must be designed and constructed for the flipper. In addition, logic is needed to implement the start trigger, e.g., a signal from the SNS accelerator, and the flipper sequence. Moreover, an RF coil is required to sense the RF field and explicitly confirm that the RF field is operating. For the resonant spin flipper, which needs a definite amplitude and frequency, some feedback electronics is likely to be needed to lock parameters. For the adiabatic flipper, a static B gradient of order ~1 G/cm over several centimeter length of neutron beam needs to be imposed. A schematic drawing of a spin flipper based on AFP is shown in Figure IV-5.

The magnetic guide field in the transition region between the spin flipper and the measurement region requires special care. The magnitude of the field needs to decrease adiabatically from several Gauss to ~10 mG to match the measurement field and must be directed in such a way that the neutrons enter the cells with horizontal (sideways) polarization. We plan to use an electromagnetic coil system to perform this task.
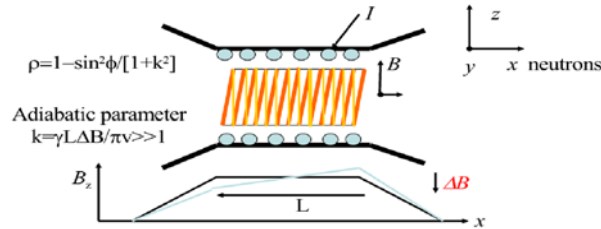
Fig. IV-5.　　Schematic drawing of an AFP spin flipper.

Flux and Polarization Monitor

A neutron flux and polarization monitor will be developed for diagnostic purposes. A compact system consisting of two ionizing chambers with ^{6}Li glass entrance and exit windows and a magnetic supermirror as a polarization analyzer sandwiched between the detection chambers appears to be suitable. Such a system is not planned as part of the permanently installed equipment. This system is intended to solve problems or for cross-checks; the analyzer will be mounted at the end of the neutron guide before the neutrons enter the cryostat. The whole system is intended to be mounted on a small moveable platform. There is just room between the two guides to slide the detectors into the beam when needed.

Shielding

The shielding of the neutron beam line should be straightforward due to the low radiation levels expected from a monochromatic beam. Nonmagnetic materials will be used. Concrete blocks as well as hydrogenous materials such as polyethylene form effective neutron shielding. Some attention has to be paid to preventing the generation of γ-ray backgrounds and to shielding such backgrounds from other sources. A complete GEANT4 simulation is to be used to optimize the shielding with the goal of minimizing the backgrounds.

References

1. R. Golub and J.M. Pendlebury, *Phys. Lett. A* **62**, 337 (1977).
2. P. R. Huffman, et al., *Nature* **403**, 62–64 (2000).
3. C.A. Baker et al., (submitted to *Phys. Rev. Lett.*) [http://arxiv.org/abs/hep-ex/0602020].
4. T.M. Ito et al. (to be published in *Nucl. Instrum. Methods Phys. Res. Sect. A*).
5. McStas, "A Neutron Ray Trace Simulation Package," [http://neutron.risoe.dk/].
6. P. Boeni et al., *Physica B* **267**, 320 (1999).
7. J. Stahn, Talk at ILL Workshop (April 2006).
8. P. Fierlinger; private communication.

V.   Cryogenics, Refrigerators, and Related Equipment (WBS 1.3)

The objective of this subsystem is to design, procure, install, and test a large vacuum container that will cool $1200\,L$ of liquid helium (LHe), plus all of the other cryogenic components of the nEDM experimental apparatus, to an operating temperature in the range of 0.30–0.55 K. The device will reliably provide these conditions for the periods (~90 days) needed to complete each full cycle of EDM measurements. The system will be designed to minimize the assembly, cool-down, warm-up, and disassembly time needed for repeated testing of other experiment subsystems.

The components of the cryogenic system include a room-temperature vacuum tank, the cryogenic vessel (CV), two intermediate temperature shields, a LHe reservoir, refrigerators, and the associated sensors and controls. The CV will include ports and feedthroughs into which the other experimental subsystems will be inserted. The CV will be nested inside the four-layer external magnetic shield system. The internal magnets and shields will be thermally linked to 4.2 K. The ^{3}He injector, the ^{4}He purifier and the EDM experimental volume will be thermally linked to 0.30–0.55 K. In addition, the cryogenics task includes the design, procurement, testing and installation of the large container that will hold the LHe required to electrically insulate the EDM measurement cells. At the conclusion of the assembly of all of these components, the cryogenic system will be tested at operating temperature and prepared for integration of the neutron EDM experimental apparatus.

External Cryogenic Vessel, Intermediate, and 4 K Shields

The main vacuum volume for the cryogenic system, the CV, will be an L-shaped aluminum pressure vessel (see Figure V-1). The "toe" of the L points upstream toward the neutron source. The horizontal section of the L will contain the main experimental volume, magnets, and shields. The vertical section will contain the dilution refrigerators (DRs), ^{3}He injector, ^{4}He purifier, and associated services. Most of the electrical and cryogenic access to the experimental volume will go through the vertical section. The CV is designed so that the experimental volume can be removed through the downstream end cap of the CV. Also, the experimenters can access the lower part of the vertical section by removing the same end cap. The upper end cap at the top of the L will include ports for the insertion of the refrigerators, ^{3}He injector, ^{4}He purifier, their shielding magnets, and electrical and control feedthroughs. The polarized ^{3}He atomic beam source will be coupled to the ^{3}He injector volume through a 45° insert into the upper vertical section of the CV. The neutron beam will enter through a foil window and collimator at the upstream end of the horizontal section of the CV. In operation, the CV will be enclosed in a four-layer passive magnetic shield.

The CV must be able to maintain high vacuum for insulation, have no magnetic effect on the experiment, and produce minimal radiation backgrounds in the operation of the experiment. This pressure vessel must be designed in accordance with ASME Standards and have appropriate safety relief valves and controls. The CV will be evacuated with a dedicated turbopump system and include a large charcoal or molecular sieve cryogenic getter thermally attached to 4.2 K.

The thermal infrared radiation from room temperature to the experimental volume would greatly exceed the available refrigeration power. Therefore the CV will contain two aluminum infrared shields at 50 K and 4.2 K. The 4.2 K shield will be cooled by the LHe in a $500\,L$ reservoir inside the CV. The 50 K shield will be cooled by the enthalpy of the evaporating LHe or a pulse-tube refrigerator, either of which is within the scope of the CV. Both of the shields will be wrapped with layers of aluminized Mylar superinsulation to reduce the effective emissivity of the shields and therefore the heat leak from high temperatures. Silicon-diode

temperature sensors will be located at several points on each shield to monitor the temperature distributions. The cool-down times and temperature distributions of each shield will be simulated as part of the preliminary design of the CV. The shields will be supported in the CV with low conductivity (e.g., G10) supports. Each of the shields will include ports and heat links for the insertion of experimental components. In the preliminary design process, the cryogenics group will provide specifications to the other researchers for the geometry and heat budget for each experimental insertion.
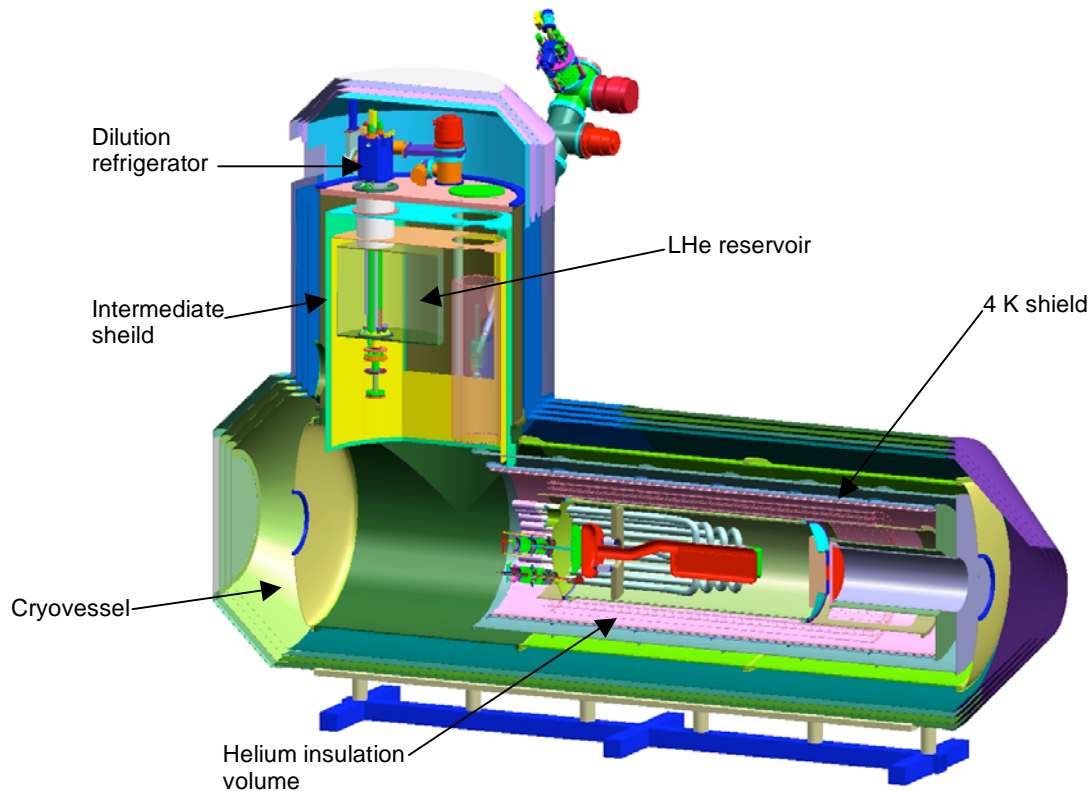
Fig. V-1.   A schematic of the EDM experimental vessel.

Helium Electrical Insulation Volume

The helium electrical-insulation volume is a nonmagnetic enclosure which will house the [4]He target cells, electrostatic plates and charging apparatus, magnetometers, and superfluid helium insulation material. The volume will be 216 cm long, with a 81.6 cm I.D., 1.27 cm wall thickness, and will be constructed of a fiber/epoxy composite. A small window flange at the upstream end will admit neutrons. The EDM experimental insert containing the target cells, HV electrodes and controls, SQUID magnetometers, and light guides will be inserted through a large flange in the downstream end of the insulation volume. A gas precool circuit will facilitate the transition to 4.2 K. The [4]He evaporator and DR will condense and cool the 1200 L of liquid through a heat exchanger mounted in the vertical section of the CV.

The electrical insulation volume is composed of an insulating composite to avoid eddy-current heating due to RF fields from the dressing coils, and to avoid causing interferences which could be measured by the SQUIDS. The system will be assembled and tested with a dummy end cap, while the experimental-insert group will design and test the end cap to be used in the experiments.

The cooling of the superconducting shield through the superconducting transition must be carefully controlled. A frequently encountered problem is that thermal gradients may produce currents and trapped magnetic fields as the shield enters the superconducting state. These fields may be greater than the field which the superconductor was supposed to shield against. Only trial and error can help to eliminate this problem. A well-controlled cool-down of the shield with the temperature decreasing from one end of it to the other may solve this problem [1]. The transition will be accomplished by a helium-flow cooling system and strategically placed heaters.

Refrigerators

The experiment requires several refrigerators. A dedicated helium liquefier will provide a steady source of liquid to the 500 L LHe reservoir in the CV. From that reservoir LHe will be distributed to the other subsystems, including the LHe insulation volume and two DRs. The 50 K infrared shield can be cooled by the vapor flow from the boiling LHe or by a separate pulse-tube refrigerator. The final design of the refrigeration system is set by matching the projected heat load produced by the experimental systems to the cooling available from the helium boil-off and the DRs.

In preliminary planning, each of the experimental subsystems has been assigned a heat budget limit on the amount of heat that can be produced by a specific valve, bellows, heater, or other component. The cryogenics group is providing design guidance to help reach these limits. We have set a projected heat load of 50 W at 50 K, 3.6 W at 4.2 K (5 L of LHe/hour), 1 W at 1.5 K and 80 mW at $T_{operating} = 0.5$ K.

The type and capacity of the helium liquefier is determined by the 5 L/hr helium boil-off rate. The cooling rate at $T_{operating}$ sets the design parameters for the DRs. These numbers are based on conservative estimates of the desired LHe expenditures and the projected cooling power of the refrigerators. Because the cooling power of a DR is proportional to T^2, the cooling limit at 0.25 K is about 20 mW.

The helium liquefier is expected to be a dedicated Linde 1430 with Model RS helium compressor module. This refrigerator system can produce 45 liquid L/hr with liquid nitrogen precool and 15 L/hr with no liquid nitrogen and room-temperature gas input. At 45 L/hr and assuming 70% transfer efficiency, it would require 85 hr to fill the 1200 L experimental volume, the 1000 L storage dewar and the 500 L LHe reservoir. Based on a 5 L/hr boil-off at the CV, the 1000 L helium storage dewar would need to be refilled every four days. Refilling the 1000 L storage dewar would require 23 hr every four days. Therefore, we expect the liquefier to maintain the CV for about 150 days between scheduled 1000 hr maintenances. This exceeds our objective of a 90-day uninterrupted cryogenic operation.

Sub-4 K Refrigerators

The experimental system, which includes the helium insulation volume, experimental insert, ^{3}He collector, and ^{4}He purifier will operate at the same temperature. The lack of a temperature gradient is enforced by the requirement that the parts are connected by large-diameter (3–4 cm I.D.) tubes through which the ^{3}He can rapidly diffuse in and out of the target. The superfluid ^{4}He in the insulation volume and in the other subsystems has a thermal conductivity greater than copper at these temperatures.

A pumped ^{4}He evaporator can cool the 1200 L ^{4}He volume in about 2–3 days from 4.2 K to below the superfluid transition. Below 2 K, DRs will complete the cooling to the operating temperature. Because of the geometric phase effect and ^{3}He diffusion rates, it is envisioned that the ideal experimental temperature will be near 0.5 K, but the cryostat is being designed to vary temperature from 0.30 K to 0.55 K, to investigate experimental systematics.

The LANL group possesses a Leiden 3000 DR (Q = 1.2 mW at 0.12 K) which can be

installed in the neutron EDM CV. The CV is designed to accept another refrigerator, to be procured for this project. This system should deliver 120 mW of cooling at 0.5 K. The draft heat budget described below is designed for 2/3 of that capacity.

The refrigerators must remove heat from conduction through the insulating vacuum, conduction through mechanical supports and infrared radiation from higher temperatures. Most of these heat leaks are reduced by the selection of construction materials and maintenance of vacuum integrity. The cryogenics subgroup will work with the other subgroups to build suitable heat sinks at higher temperatures and to reduce infrared absorption. Heating due to neutron radiation is negligible.

Several experimental components produce heat from their operations as listed in Table V-1.

Table V-1.   Anticipated Subsystems Heat Sources to the Cryogenics System

Subsystem	Sources of Heating	Heat flows to
^{3}He injector	Infrared radiation from atomic beam source	Mixing chamber of DR at $T_{operating}$
	Heating due to superfluid film flow killer	Mixing chamber of DR
^{4}He purifier	Valves	Mixing chamber of DR
	Superfluid film flow killer	Mixing chamber of DR
	Displacer bellows	Mixing chamber of DR
	Charcoal pump regeneration	4.2 K
	Gas conduction heat switches	4.2 K
EDM experimental insert	Valves	Mixing chamber of DR
	Pressurization bellows	Mixing chamber of DR
	High voltage control actuators	Mixing chamber of DR
	Light pipes	Mixing chamber of DR
Magnet system	External current leads	4.2 K
	I2R loss in conventional magnet windings	4.2 K

Cryogenic Vessel Sensors and Controls

The routine operation of the cryogenics system will require temperature, pressure, vacuum, and LHe-level sensors as well as indicators of pumping-system controls and fail-safe devices. To increase reliability, duplicate sensors will be used at critical parts of the cryogenics system. It is the responsibility of the cryogenics group to specify, procure, and install each of these sensors and their readout electronics, then to provide the outputs that will communicate with the neutron EDM slow controls system. The cryogenics group will also recommend sensor choices to the other researchers so that all subsystems will use compatible, if not identical technologies. Table V-2 indicates the principal sensors and controls. Each of these components and their readout electronics can be bought commercially. Some calibration of the thermometers may be required during the assembly of the cryogenics. The cryogenics group must also document all calibrations and usages of the sensors and controls.

Table V-2.   Types of Sensors Required for Proper Cryogenic System Operation

Sensor	Description
Temperature sensors (T ≥ 4.2 K)	Silicon diode sensors located at several points on 50 K and 4.2 K shields and in the LHe reservoir.
Temperature sensors (T ≤ 4.2 K)	Resistance thermometers for refrigerator components and at several points on the LHe insulation volume.
Vacuum sensors	To measure the pressure within the vacuum insulation space of the external CV.
Pressure sensors	To measure the gas pressure in the LHe reservoir and in the LHe insulation volume. Multiple pressure sensors for the room temperature gas handling systems for the refrigerators. Several of these sensors will provide over-pressure alarms.
LHe level sensors	Several level sensors in the LHe reservoir, to monitor the filling of the LHe insulation volume, and to monitor alarm conditions.
Heaters	Several heaters are needed for the operation of the DRs and for warming the cryogenics components prior to disassembly at room temperature.
Valve position indicators	Digital indicators for positions of valves in the room temperature gas handling systems for the refrigerators and the CV.
Control valves	Cryogenic flow controls for the liquefier and refrigerators.

Cryogenic Vessel Assembly, Testing, and Operational Infrastructure

The design, construction, and testing of the CV system will be supported by the preparation of the CV infrastructure, installation of the CV support structure, assembly of tools and components necessary for operation, and authoring and collection of documentation, including safety documentation and procedures. Because the CV will not be mounted on the external shields until it arrives at the SNS, an equivalent CV support will be constructed for assembly and testing at NCSU/TUNL. Several custom fixtures will be produced for the assembly: a fixture to remove and store the external end cap and 50 K shield, a fixture for loading of the horizontal LHe insulation volume, a platform for experimenter access to the top of the CV, and a platform/walkway for experimenter access inside the horizontal space in the CV.

The group will procure and assemble the standard list of tools and devices needed for the testing of the CV. These include two helium leak detectors, a turbopumped vacuum station, and miscellaneous vacuum pumping lines and fittings. These tools and fixtures will be used throughout the assembly, integration, and operation at NCSU/TUNL and ORNL.

It is the responsibility of the cryogenics group to provide all documentation on the assembly and operation of the CV, refrigerators, and sensors. The cryogenics group must also document and disseminate information on safety hazards and safe operation of the system. The major hazards and their mitigations related to the CV are described in the accompanying Preliminary Hazard Analysis.

Testing of Cryogenic Vessel and Components

The cryogenics system will be assembled and tested at NCSU/TUNL. Because of the emphasis on reliability and the extended time needed for assembly, cool-down, and disassembly of the large CV, each component will be inserted into the CV and tested in series. The work schedule calls first for the insertion of the shields into the CV and vacuum testing at liquid-nitrogen temperature. Next, the helium liquefier will be connected to the CV and the entire system checked at 4.2 K. Then, the DRs will be installed and tested. The final stage will include the installation and testing of the LHe insulation volume at the planned operating temperature ($0.30 < T_{operating} < 0.55$ K), first without the magnets and eventually with them in place. The

objective is to characterize and to document the operation of a reliable cryogenic system before integrating the ^{3}He injector, the ^{4}He purifier, and the EDM experimental insert as each piece is added to the apparatus.

This cryogenic system is very large and will require time to assemble, cool, test, and warm up. The large volume must be pumped to a high vacuum. Leak detection and system testing should take place at 50 K and at 4.2 K. The 1200 L ^{4}He volume will take days to cool below the superfluid transition and more days to cool to 0.5 K. The necessarily large thermal mass of the CV increases the time needed to warm up the system after a cool-down. Our schedule includes three complete cool-downs for testing after the CV is assembled. This plan is aggressive and assumes that every precaution has been taken to test components before integration into the CV.

References

1.   F. Pobell, *Matter and Methods and Low Temperatures*, 2nd Ed., (Springer-Verlag, Berlin, 1996), p. 317.

VI. ^{3}He Systems (WBS 1.4)

The measurement technique proposed for this experiment employs polarized ^{3}He dissolved in ^{4}He as a comagnetometer. The ^{4}He provides mechanisms both for creating UCNs and for detecting interactions between ^{3}He atoms and UCNs. The number of unpolarized ^{3}He must be reduced to the level of 10^{10} atoms/cm^3 in order to prolong the UCN storage time. The ^{4}He must, therefore, be isotopically purified. The preparation and delivery of this mixture of polarized ^{3}He and purified liquid ^{4}He to the measurement cells is the task of the ^{3}He systems (He3S).

A block diagram of the major components of this part of the apparatus, already briefly described in Section II, is illustrated in Figure VI-1. Much of this subsystem resides in the upper cryostat, for which a conceptual design is shown in Figure VI-2.
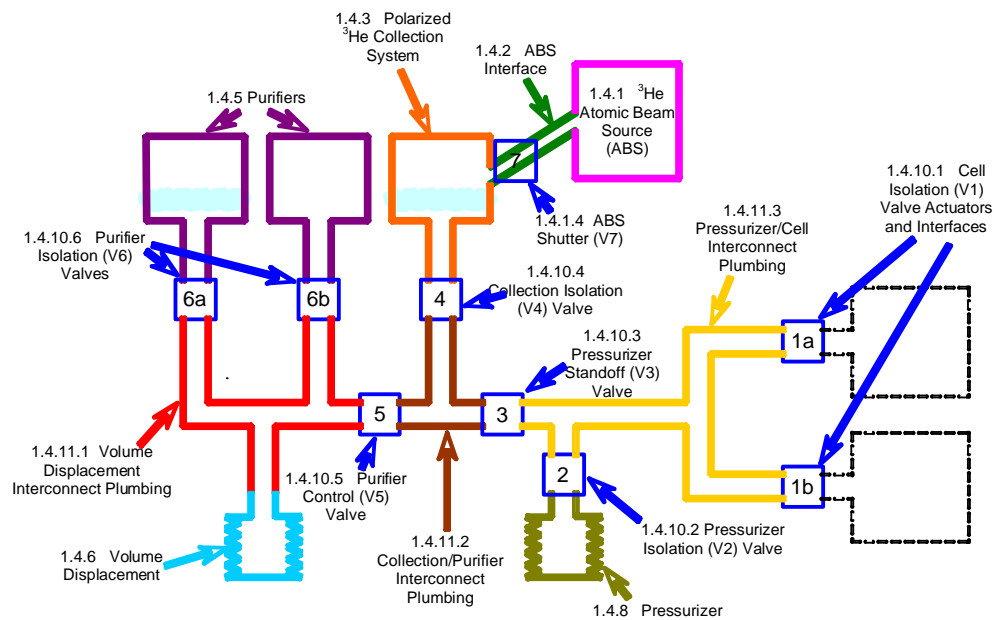

Figure VI-1. This block diagram illustrates the interconnection between the major components of the He3S subsystem. WBS identifying numbers are also noted.

The measurement cycle, during which the neutron precession rate in an electric and magnetic field is measured, is repeated many times during the course of the experiment. The cycle, listed in Table VI-1 with estimates for the durations of the individual steps (and also described with less detail in Section II), is largely controlled by manipulating the components of the He3S. This outline assumes the polarized ^{3}He relaxation time is long enough to allow transfer of the atoms to the measurement cell before UCNs are introduced.

After the completion of a number of measurement cycles, it is expected that the purifier absorption pump will require regeneration. To allow the measurements to continue during regeneration, two purifiers will be installed. A volume-displacement bellows and associated purifier isolation valves allow the absorption pump of one purifier to be regenerated while the other is in use.

The configuration of the He3S and a number of design decisions related to its components are subject to the outcome of the R&D studies described in Section III. Some of the technology, including evaporation purification, polarized ^{3}He injection, superfluid film control, and reliable 0.3 K-rated valve design, will be prototyped and attempted for the first time during those R&D studies. For this reason, we plan additional testing of the final components to ensure that they perform reliably and that they meet the necessary specifications. The long cool-down

time for the full nEDM apparatus provides additional impetus for pre-installation testing. Separate tests are planned for the polarized ³He injection, the purifiers, and the pressurization system. These will be followed by a test of the entire He3S before its incorporation into the full experiment. In the following sections, all of the components of the He3S will be described in more detail.
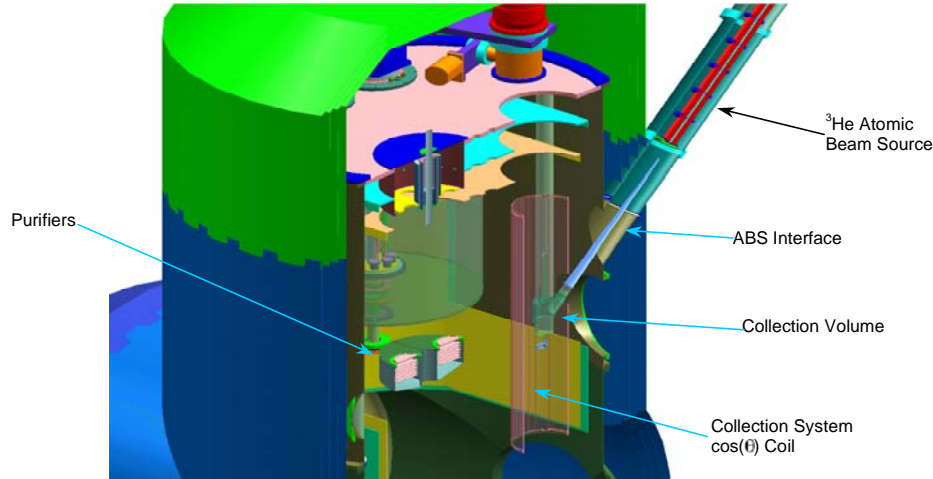
Fig. VI-2.   The upper cryostat of the entire experiment.

Table VI-1. The Measurement Cycle of the Neutron Precession Rate in an Electric and Magnetic Field[a]

Start (s)	Activity	
0	Purify LHe in purifier,	Flip spins, measure precession (1000)
885	Close V4, open V7 (10)	
895	Collect polarized 3He (100)	
995	Close V7 (5)	
1000	Reduce electric field (20)	
1020	Open V2 (5)	
1025	Decrease cell pressure (10)	
1035	Open V1a, V1b, V3 (15)	
1050	Purify "cell" LHe (200)	
1250	Close V2, V5, open V4 (10)	
1260	Load polarized 3He into cells (10)	
1270	Close V3, open V2, V5 (10)	
1280	Increase cell pressure (10)	
1290	Close V2, V1a, V1b (15)	
1305	Increase electric field (10)	
1315	Open n shutter (5)	
1320	Accumulate UCNs (1000)	
2320	Close n shutter (5)	

Repeat measurement cycle.

[a] Many of the operations that occur during the measurement cycle involve components of the He3S. The cycle begins with valves V1a, V1b, V2, and V3 closed and with V4, V5, and V6a or V6b open. The estimated durations of activities during the cycle are given in parenthesis in seconds.

A. ³He Atomic Beam Source

The motivation for the ABS is that, although the production rate for polarized ^{3}He is very small with an atomic beam compared to the usual optical pumping techniques, it is easily sufficient for the EDM experiment. Furthermore, the state selection method used in an atomic beam source can yield near perfect polarization, compared to 70% for optical pumping techniques.

The technical details of the ^{3}He atomic beam source were presented in Section V.G (pp. 136–139) of the preproposal. This source has now been constructed and tested, with the design goals slightly exceeded. Specifically, the polarized ^{3}He production rate is about 10^{14}/s, with an angular divergence of 0.008 radians (half-angle). The degree of polarization is better than 99%, with the accuracy of this result limited by the ability to discriminate a small background of unpolarized ^{3}He gas. This background can be made negligible by a straightforward inclusion of differential pumping at the source output.

The degree of polarization was determined by use of a quadrupole magnet assembly, or analyzer, identical to the polarizer, through use of radio frequency spin manipulation techniques in a 1-m-long free-flight region between the polarizer and analyzer. The ^{3}He transmitted through the analyzer was measured using a SRS RGA250 residual gas analyzer, which provided excellent signal-to-noise in measuring the ^{3}He atomic current via pressure buildup in a collection tube.

The remaining tasks are to demonstrate that the polarizer will work when tilted at 45° as is required to inject the polarized atoms into a superfluid bath by having them strike the surface at an oblique angle (see Figure VI-2). The system as-built has a horizontal beam. The polarizer support structure has been modified to allow tilting, and these tests will be completed in June 2006. In addition, a differential pumping stage for the polarizer output to eliminate unpolarized background helium gas has been designed and will be incorporated.

B. ABS Interface, ³He Injection and the Collection Volume

The ^{3}He collection volume will be made of Pyrex glass with a cesium coating to minimize depolarization of ^{3}He through interaction with the wall. The current design of the collection volume and the ABS interface is shown in Figure VI-3. Figure VI-2 shows the ^{3}He injection/collection region in the upper cryostat of the nEDM experiment. A cesium ring serving as a ^{4}He film killer is needed at the injection port to prevent a large thermal load. The injection port is oriented such that ^{3}He atoms entering from ABS will impinge directly on the superfluid ^{4}He liquid surface rather than the collection-volume wall. The interface tube will be thermally linked to the 50 K and 4 K heat shields of the upper cryostat. This arrangement will reduce the radiative thermal load from the 1 cm aperture of the ABS to only a few mW. A magnetic-field transport system will be implemented around the ABS interface tube. It will be arranged to both adiabatically rotate the ^{3}He spin direction from along the axis of the ABS to parallel to the collection volume liquid surface (horizontal) and to match the magnitude of the collection-volume holding field. A cosθ coil with a diameter of 40 cm and a length of 130 cm will be mounted around the collection volume in order to provide a magnetic holding field with a field uniformity of 0.1%. The typical holding field from the cosθ coil will be on the order of 10 mG, but the magnet will have the capability of reaching a few Gauss. This option is necessary because the injection/collection test during the installation phase of the experiment will take place before the final installation of the magnetic shields for this part of the experiment. A polarized ^{3}He "friendly" valve, the ABS Shutter (V7), will be used to separate the ABS interface region from the ^{3}He collection volume.
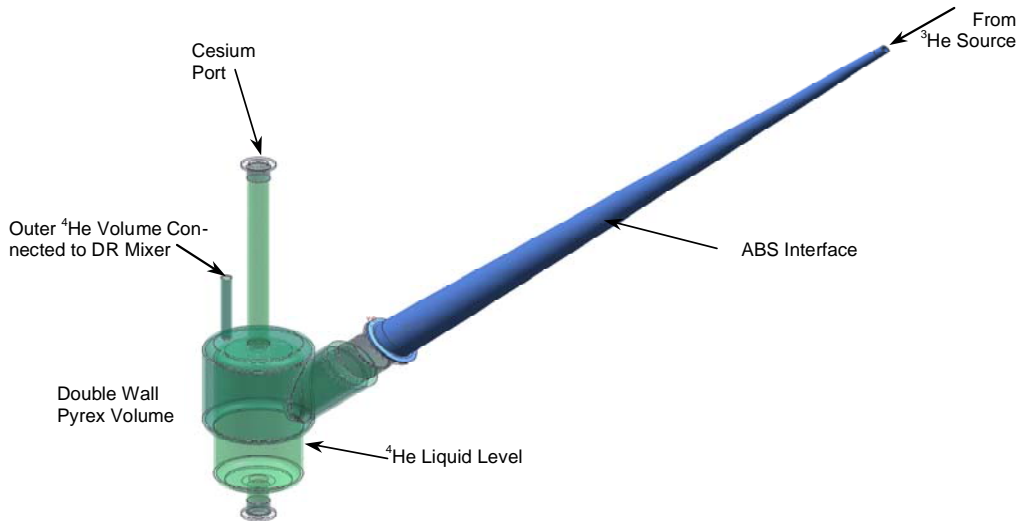
Fig. VI-3.   The current design of the Pyrex collection volume for polarized ^{3}He.

In addition to the ABS-interface port, there are two vertical ports on the collection volume. The upper one provides access to the collection volume for in situ cesium coating of the walls. A cesium ring is needed for this port in order to break the ^{4}He film and to suppress the reflux. The bottom port connects, initially, to the Collection Isolation Valve (V4), and then, via a series of interconnects and valves, to the nEDM measurement cells. This entire interconnection system must be polarized-^{3}He "friendly". With a ^{3}He flux of 10^{14}/s, the overall collection time is estimated to be of order 100 s, and the depolarization of ^{3}He during this period is expected to be negligible. The current design of the collection volume calls for a double-wall region to be filled with superfluid ^{4}He from the DR mixer. This will provide efficient cooling with good thermal contact to the poorly conductive glass collection volume.

Alkali-coated Pyrex surfaces have been shown to minimize ^{3}He depolarization at the container walls. Cesium rings are known to be effective at breaking the superfluid ^{4}He film, which would otherwise flow towards warmer temperatures. The cesium ring suppresses the reflux of the ^{4}He and helps to confine ^{3}He to the liquid or to the vapor just above the surface [1]. Therefore, cesium coating of the entire collection volume and the formation of cesium rings at the inlet of the ABS interface and at the inlet of the upper ^{4}He supply port are necessary for this experiment. However, these two procedures have only been undertaken, in the past, in much smaller and more straightforward geometries [1]. In our experiment, the collection volume where the liquid resides will be on the order of 1 L. Detachable glass seals will be mounted at all ports of the Pyrex collection volume so that the formation of cesium rings can be carried out in a separate vacuum and cesium handling system before installation. It is expected that the cesium coating of the volume will also be carried out before installation, but the design allows for the possibility of renewing this surface in situ.

R&D tests of the polarized ^{3}He injection and collection will be performed before the construction of the experiment. These tests will be carried out at Los Alamos where the working ABS is located. A cosθ coil with a diameter of 30 cm and a length of 100 cm will be built by the Caltech group for this test. A low-sensitivity NMR system will be implemented in order to measure the ^{3}He magnetization in the collection volume, thereby demonstrating the success of the injection and collection of polarized ^{3}He. The total anticipated number of ^{3}He in the collection volume will be on the order of 1×10^{16}. Based on previous low-sensitivity adiabatic fast passage (AFP) NMR measurements on ^{3}He at room temperature [2] and at 1.9 K [3] in a

holding field of about 25 G, one expects that the AFP NMR measurement for the ^{3}He injection/collection test will be feasible at similar holding field values.

C. Isotopic Purification of ^{4}He

LHe with fractional isotopic concentrations X of ^{3}He of order 10^{-12} or less is required in approximately 10 L volumes for the nEDM experiment. This specification can readily be met using purification systems that rely on the heat-flush effect. A heat-flush effect based purifier identical to the robust systems developed and refined by McClintock and collaborators [4] has been donated to the collaboration by the Hahn-Meitner Institute and will be used to provide the initial bolus of liquid (see Section VI.E).

The same methods could also be used to repurify the liquid (from $X \sim 10^{-10}$ back to $X \sim 10^{-12}$) at the end of every measurement cycle. The only drawback is that the heat-flush effect requires the liquid to be at a temperature T of 1 K or higher. This constraint adds significantly to both the cost and the complexity of the overall experiment. For this reason, we have decided to adopt one of the evaporative isotopic purification schemes proposed by Hayden, Lamoreaux, and

Fig. VI-4. Time constant for removal of ^{3}He from a 10 L volume of liquid ^{4}He by forced evaporation through a 30 cm diam free-liquid surface, as calculated in Reference [5]. At high temperatures, the extraction rate is limited by the diffusion of ^{3}He impurities in the liquid phase [6,7]. While at low temperatures, it is limited by the thermal escape probability. The dashed curve illustrates the influence of ^{3}He-^{3}He scattering when X is (relatively) large. The optimum operating temperature for a sorption-pump-based ^{3}He extraction system is expected to occur at around 0.4 K (see text).

Golub [5]. The advantage of these schemes is that the liquid can be purified at temperatures close to those at which the nEDM experiment will operate.

The principle underlying evaporative isotopic purification of LHe is simply the fact that it requires less energy to remove a ^{3}He atom from a dilute mixture of ^{3}He dissolved in liquid ^{4}He (about 3 K) than it does to remove a ^{4}He atom (about 7 K). In other words, ^{3}He is more volatile than ^{4}He, and so it can be preferentially extracted from the liquid by pumping on the vapor. Clearly, this has to be done at a temperature where the thermal escape probability for ^{3}He atoms is high enough. At the same time it *should* be done at a temperature low enough that the evaporation of ^{3}He atoms is not impeded by diffusion through the bulk liquid. A compromise between these constraints exists in the vicinity of 0.6 K, at which point remarkably fast extraction rates are expected (10 s timescales for 10 L volumes of liquid, see Figure VI-4). In practice, lowering the extraction temperature somewhat further in order to reduce ^{4}He vapor pressure is advantageous. This reduces the rate at which ^{4}He atoms have to be extracted from the liquid and hence simplifies constraints on the pumping system. A reasonable compromise is expected in the vicinity of 0.4 K, at which point it is still possible to purify sufficiently large quantities of liquid ^{4}He during the timescale set by the EDM measurement cycle and yet the ^{4}He vapor pressure is low enough that conventional low-temperature sorption pumps can be used.

Evaporative isotopic purification of liquid ^{4}He down to fractional ^{3}He concentrations X of order 10^{-9} and below has been demonstrated previously for temperatures $T > 1$ K [8]. The
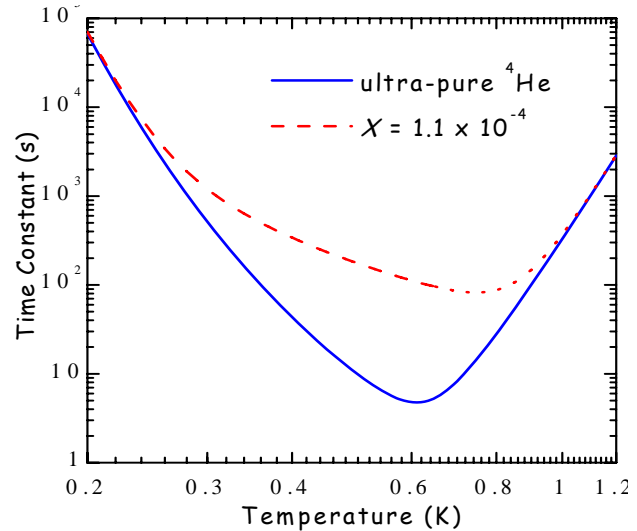
primary challenge associated with lowering the operating temperature (to take advantage of rapid ^{3}He diffusion in the liquid) is associated with the fact that the saturated ^{4}He liquid forms a Van der Waals film that tends to coat most exposed surfaces. The chemical potential of the liquid is such that this film flows from regions of low temperature to regions of high temperature. This flow is accompanied by a dramatic increase in the ^{4}He evaporation rate (the saturated vapor pressure of the liquid is an exponentially increasing function of temperature), which in turn has several deleterious effects. First of all, the hot vapor tends to condense in regions where the liquid temperature is low, imposing a demanding heat load on the refrigeration system [9,10]. Second, the evaporating film limits the base pressure and hence the ^{3}He extraction efficiency of the pumping system. Finally, the presence of a film makes it all but impossible to use a cryogenic sorption pump operating at or near the liquid temperature; the film would immediately cover the entire surface of the pump.

Several methods for impeding or eliminating the flow of a superfluid helium film exist. The traditional approach is to "stress" the film by forcing it to flow over a surface with a sharp radius of curvature (a "knife edge") [11]. This reduces the critical velocity of the fluid and hence the heat load required to "burn" the film. More recently annular rings of cesium metal (the only known substance that is not wet by liquid ^{4}He) have been employed to block film flow entirely [12]. The approach we intend to use is simpler and expected to be more robust over the lifetime of the experiment. Rather than trying to inhibit the flow of LHe toward the pump, the idea is to use a sorption pump that operates at a temperature below that of the liquid with the result that the film will tend to flow *away* from the pump. In effect, this strategy is very similar to a scheme that has been used previously to stop film flow in DRs [13].

Figure VI-5 summarizes the principal elements of the sorption-pump-based evaporative helium-purification scheme presently envisaged by the collaboration. Given the number of options that exist for restricting film flow and the fact that an equivalent purifier has never been constructed, an appropriate test of this scheme, as well as competing options, will be completed as part of the R&D program (see Section III). The outcome of these tests will determine the final purifier design.

We anticipate employing a pair of charcoal pumps, even though each pump is expected to have enough capacity for many purification cycles. This provides redundancy for a critical component of the experiment as well as a means for regenerating the charcoal in one pump without having to interrupt the measurement cycle. Each pump is enclosed within a volume into which a shallow pool of LHe (with a large surface-area-to-volume ratio) can alternately be admitted or extracted using a system of bellows and valves. The charcoal and adjacent walls are maintained at a temperature below that of the bulk liquid in order to inhibit film flow. Further detail is shown in Figure VI-6.

At the end of a measurement cycle, "dirty" ^{4}He (with fractional ^{3}He concentrations of order 10^{-10}) is manipulated into one of the sorption-pump volumes and heated to an appropriate temperature (if necessary). The preferential evaporation of ^{3}He from the liquid surface and its subsequent adsorption by the pump results in isotopic purification of the liquid on a time scale of a few hundred seconds. At this point, the liquid is extracted and moved to the polarized ^{3}He collection volume. Regeneration of the sorption pumps (after many measurement cycles) is accomplished by opening thermal heat switches than normally keep the temperature of the charcoal below that of the bulk liquid and heating the charcoal while evacuating the sorption-pump volume with external pumps.
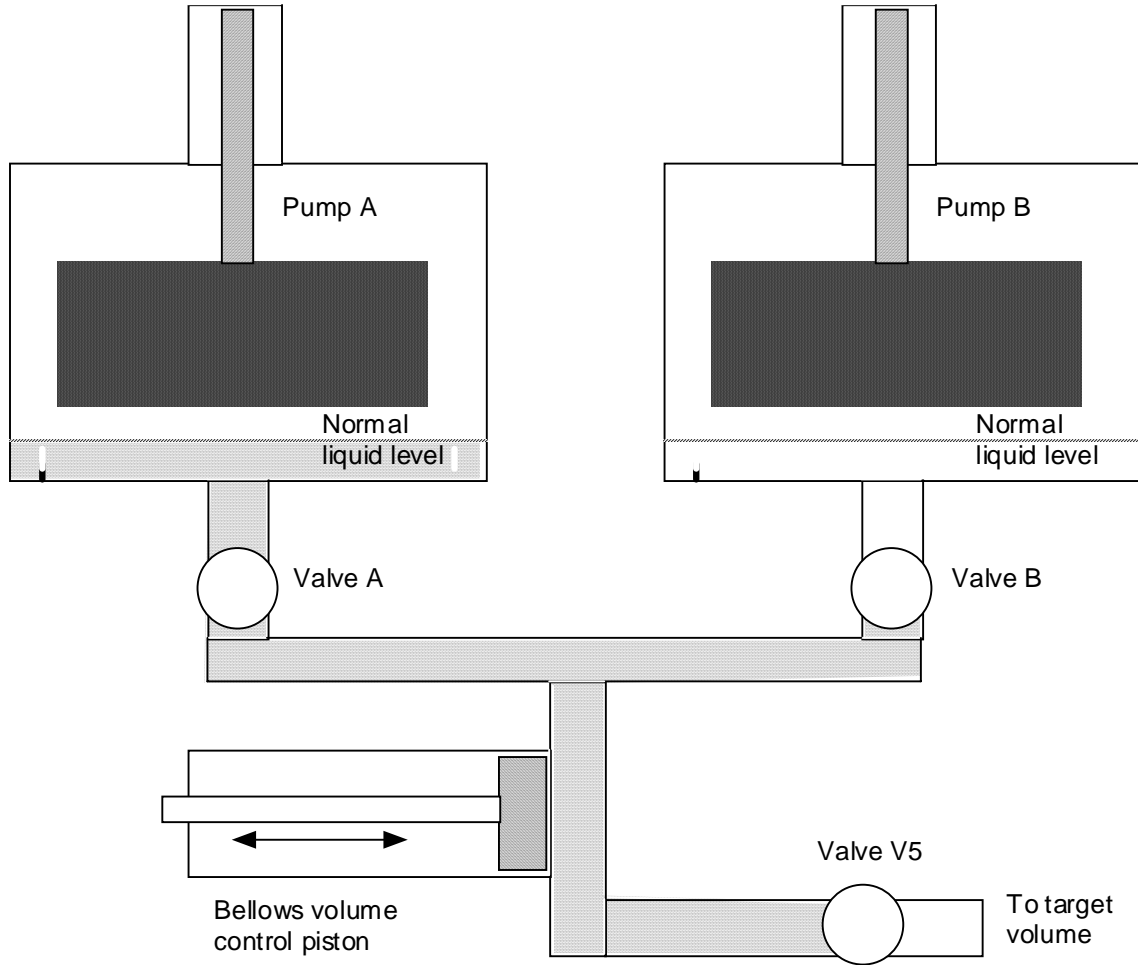
Fig. VI-5.   Schematic diagram illustrating the manner in which LHe is manipulated into one of two charcoal sorption-pump-based isotopic purifiers. Further detail of the purifier volume is shown in Fig. VI-6.

D. The Pressurization Option

The figure-of-merit of the nEDM experiment is proportional to the magnitude of the electric field that can be achieved within the measurement cells. To date, studies of the breakdown voltage in ^{4}He have achieved the required 50 kV potential only at atmospheric pressure and 4 K. Operating at lower ^{4}He temperatures has resulted in lower breakdown voltages. See Section VIII for a further discussion of this phenomenon. In order to reach 50 kV, it may be necessary to pressurize the fluid in the measurement cells. A great deal of R&D is required to determine whether pressurization needs to be employed. In the following, the extra complexity induced by pressurizing is explored in the case it is needed.

Pressurization of the 0.3 K LHe would be carried out by reducing the volume occupied by the helium while maintaining constant temperature. This process could be accomplished by compressing a bellows using an actuator driven from outside of the cryostat. The change in volume

$$\frac{\Delta V}{V} = \frac{V_{Bellows} - V'_{Bellows}}{V_{Bellows} - V_{Tube} - V_{Cells}} \tag{VI.1}$$

required to raise the pressure from the vapor pressure of [4]He at 0.3 K to 1 bar is 1.1%. For the roughly 20 L volume of the measurement cell, pressurizer/cell-interconnect plumbing, and pressurizing bellows, this implies a modest 0.22 L change. Associated with the change in volume is a heat of compression of about 0.16 mJ, which would impose a negligible heat load for reasonable pressurization times. More serious may be the heat load associated the mechanical work done to compress the bellows itself. This will depend on the choice of bellows material. It will be experimentally measured during R&D testing of the pressurizer design. The heat budget goal of 1.25 mW may limit the speed with which the compression can take place.

Draft Detail for Evaporator
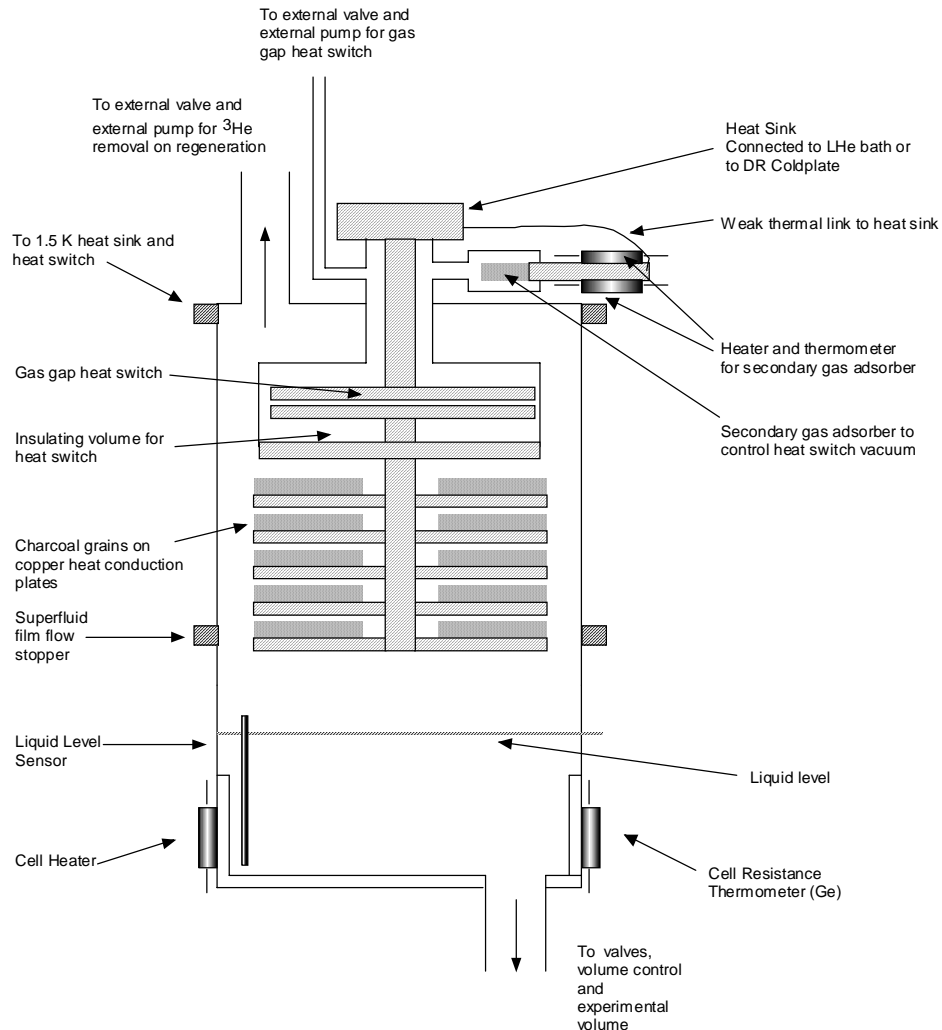
Fig. VI-6.   Detail illustrating elements of the proposed evaporative isotopic purification system.

Assuming that the pressurizing bellows will be in contact with polarized [3]He, it must be made of material that will not cause excessive relaxation. Conventional metal bellows are ruled out. One candidate material for the bellows is Teflon. It remains ductile at cryogenic temperatures, and both formed and "welded" Teflon bellows are available commercially. Low-temperature tests of the reliability of Teflon bellows and the outcome of R&D measurements of the [3]He relaxation time in the presence of Teflon will determine its suitability for this

application. Reducing the exposure of the pressurizer to polarized [3]He would allow materials with shorter relaxation times to be considered. Reduced exposure is the purpose of the Pressurizer Isolation Valve (V2), which is opened just before and closed immediately after the bellows is compressed in the measurement cycles listed in Table VI-1. Another possibility, attractive because it eliminates an actuator feed-through, is the isolation of the pressurizer bellows with a "superleak", which would allow only the passage of superfluid [4]He. Whether this is a practical solution depends on the degree to which the superleak truly stops the flow of [3]He and on its conductance of [4]He.

The force required to compress the helium by 0.22 L is negligible compared to that required to compress the bellows material. A helium pneumatic actuator, similar, if not identical, to the system planned to actuate the valves, is employed to transmit this force from 300 K to the 4-K shield. A thermally nonconductive mechanical linkage will provide the final connection to the pressurizing bellows.

E. Valves and Interconnections

In the He3S, five different types of valves are required to effect the loading of polarized [3]He into the superfluid [4]He and its removal after the measurement period. Each valve will consist of an actuator assembly at 4 K and a stem/seat assembly at the operating temperature of 0.3 K. After describing the common actuator for all the valves, the general and particular properties of each of the five types are described in turn.

The actuators must transmit a force applied at room temperature to the valve assemblies at the operating temperature. For most of the valves in the He3S located in the upper cryostat region, it is likely that the force can be transmitted from a simple rotary or linear feedthrough at room temperature (located on the top flange of the upper cryostat) via a simple mechanical linkage to the valve assembly proper. This linkage would have heat stations at 50 K, 4 K, and 1.2 K. Should the geometry prove to be too complicated for such a simple link, the force can be transmitted using [4]He gas at a maximum pressure of 0.75 atm as the working fluid in a "pneumatic" piston-and-cylinder arrangement. In this case, the room-temperature feedthrough is used to compress or expand a first bellows at 4 K (and in vacuum) but located physically near the room temperature feedthrough so that 'line-of-sight' operation is possible. The [4]He gas in the first bellows would be forced through a small tube to a second bellows at a 'remote' location (also at 4 K and in vacuum), causing it to expand or compress and activate a valve stem. A force of 40 N, for example, could be generated with a bellows approximately 8.5 cm in diameter. This arrangement provides for indirect connections from 300 K for control of the valves. The bellows system is to be used for control of the valves on the target cells (described in Section VIII), which are far from the region of the upper cryostat feedthrough plate.

The valves for the He3S proper are of five different types (valve V1 on the cell is described in Section VIII). The materials for all the valves and actuators must be nonmagnetic to prevent affecting the required field uniformity; for cold devices this requirement precludes the use of any superconducting materials as well. The valves and actuators for the He3S are placed in a region of apparatus that can be shielded from neutrons, so these materials are not restricted by activation considerations. The additional materials considerations are mainly associated with the depolarization of [3]He. For those parts of the system that do not have to be compatible with polarized [3]He, alloys such as BeCu, CuNi, and silicon-bronze are usable. Glass (either uncoated or coated with a few monolayers of cesium) or possibly acrylic (again either uncoated or coated) may be considered for surfaces wetted by polarized [3]He.

Aside from the Pressurizer Standoff Valve (V3), which has a pressure-difference specification, the maximum leak rate for these valves is set by the requirement that, in the

relatively short time these valves are "visible" before the cell valves are closed, the fluid interaction with the valve should not significantly affect the overall ^{3}He polarization, e.g., ^{3}He depolarized by the valve which leaks back into the main volume. The conductance of each valve must be consistent with that of the interconnect plumbing.

The Pressurizer Isolation Valve (V2) is used to isolate the cell pressurizer from the rest of the system. Its purpose would be to provide a polarized ^{3}He "friendly" surface for an interval after pressurization and before the cell valves are closed. The pressurizer may require materials with relatively short ^{3}He relaxation times. The leak rate need only be consistent with minimal ^{3}He depolarization during the short period when the polarized ^{3}He is transferred from the collection volume to the cells and before the cell valves are closed. There is no pressure difference across this valve.

The Pressurizer Standoff Valve (V3) is used to isolate the purification and collection parts of the system from the cells. It must sustain a pressure difference of 1 atm between the cells and (the very low pressure of) the purifier. It must be sufficiently compatible with polarized ^{3}He to cause minimal depolarization during the transfer from the collection volume to the cells.

The Collection Isolation Valve (V4) is used to isolate the collection volume. In its closed position, it must have a ^{3}He depolarization time well in excess of the anticipated time required to load the collection volume (100 s). When open, it must be sufficiently compatible with polarized ^{3}He to cause minimal depolarization during the transfer from the collection volume to the cells. There is no pressure difference across this valve.

The Purifier Control Valve (V5) is used to decouple the purifier when polarized ^{3}He is transferred from the collection volume to the cells. When closed, it must be sufficiently compatible with polarized ^{3}He to cause minimal depolarization during the transfer from the collection volume to the cells. It also provides additional protection during a switch between purifier volumes when one of the purifier pumps needs to be regenerated. There is no pressure difference across this valve. Valves V4 and V5 may be of the same type.

The Purifier Isolation Valve (V6a & V6b) allows a single purifier to be used at one time. There is no polarized ^{3}He requirement for these valves. There are no pressure differences across these valves.

The ABS Shutter (V7) controls the beam of polarized ^{3}He from the atomic beam source. Its leak rate should be such that it allows only a small fraction of a single "charge" of polarized ^{3}He into the collection volume in the (relatively longer) time between collection-volume fillings. There is no pressure drop across this valve.

As currently planned, the plumbing network, shown in Figure VI-1, which connects the various components of the He3S and the measurement cells, calls for three plumbing segments: the "Volume Displacement Interconnect Plumbing," the "Collection/Purifier Interconnect Plumbing," and the "Pressurizer/Cell Interconnect Plumbing." These transport tubes should be nonmagnetic, nonsuperconducting, and not prone to activations by neutrons. Glass and acrylic plastic will be evaluated for this application. Connections to valves at the ends of the plumbing segments must be superfluid tight. Differential thermal contraction will make this requirement challenging. A direct connection from glass to acrylic would be the most difficult from this point of view because they have the largest difference in thermal contraction rates. One possible solution, to be tested during the R&D phase of the experiment is illustrated in Figure VI-7. An "H"-shaped Nylon gasket is used to seal, in this case, copper and acrylic (fused copper glass seals are commercially available). The large coefficient of thermal contraction of Nylon ensures that during cool-down the seal is maintained on the outer surfaces, while during warm-up, it is
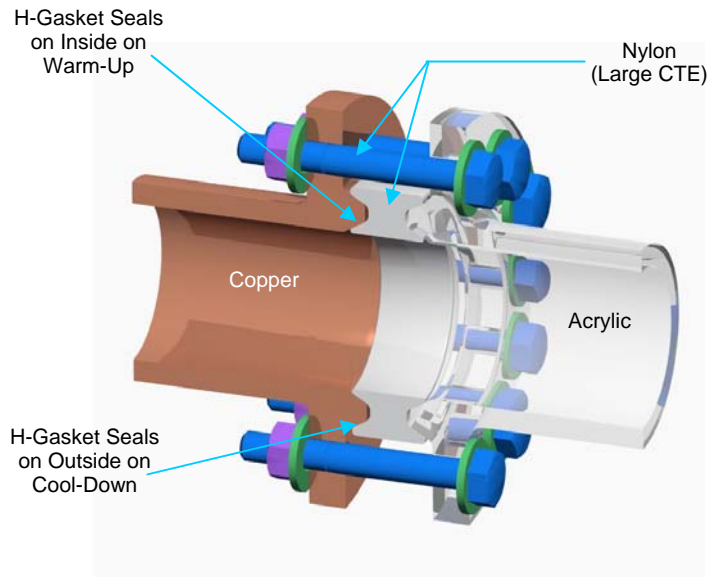
Fig. VI-7.   This figure illustrates an "H"-gasket cryogenic connection system under consideration for connections, which involve materials of dissimilar coefficient of thermal expansion (CTE).

the inner surface that remains sealed. The ^{3}He-"friendliness" of Nylon must be checked as part of the R&D program.

Because of the moderate value of diffusion coefficient of ^{3}He in superfluid ^{4}He at 0.5 K, the superfluid ^{4}He behave as a nearly perfect mechanical vacuum from the point of view of ^{3}He atoms. ^{3}He–^{3}He collisions do not hinder diffusive/ballistic flow significantly because the ^{3}He density is low. The diameter of the transport tubes is therefore determined by the requirement that conductance of ^{3}He in this pseudovacuum be large enough to result in a reasonable transit time to the purifiers and thus a reasonable purification time. Calculations suggest that a diameter of order 3.5 cm will be required to empty the measurement cells in less than 200 s.

Because the second and the third segments provide the interconnection between the polarized ^{3}He collection cell and the measurement cells, they must be constructed using ^{3}He "friendly" material (i.e., material which does not depolarize ^{3}He). Moreover, solenoid coils surrounding these two plumbing segments are required to provide the holding fields for preserving the ^{3}He polarization. An upper limit on the field homogeneity has been calculated for a transport tube of 1 cm diameter. The transit time of any particular ^{3}He atom would be approximately 2 s. Hence a T_1 relaxation time longer than 200 s is needed to limit the polarization loss to less than 1%. This implies a requirement on the magnetic field homogeneity better than 1.8 mG/cm, which can be readily achieved.

F. McClintock Purifier

As noted in Section VI.C above, evaporation purification is impractical when the initial ^{3}He concentration is that of natural helium (0.000137% atomic abundance). Therefore, the initial load of purified ^{4}He is to be generated by a separate apparatus which employs the McClintock "heat-flush" mechanism [4,14]. The heat-flush technique relies on the fact that ^{3}He atoms in superfluid helium form part of the normal fluid component. Thus, in thermal counterflow, where normal fluid travels away from a source of heat and superfluid simultaneously moves towards it, any ^{3}He atoms tend to congregate at the colder end of the apparatus. A purifier based on this mechanism has been donated by the Hahn-Meitner Institut and tested at Los Alamos in June of

2003. Using a mass spectrometer at Argonne, the purity of the resulting ⁴He has been checked and meets requirements. While the actual purification is quite rapid, it is expected that about one week (beginning from a "warm start") is needed to produce the purified ⁴He required by the experiment.

Some refurbishment and the replacement of hardware borrowed for the initial purifier test is necessary if this apparatus is to become a production facility of purified ⁴He for subsystem commissioning and for the nEDM experiment itself. The repairs includes replacement of sensors and corresponding readout controllers plus acquisition of a high-speed Roots blower pumping system, power supplies for heaters, and a compressor and associated transfer line to push purified gas to a storage tank.

References

1. D. Candela, M.E. Hayden, and P.J. Nacher, *Phys. Rev. Lett.* **73**, 2587 (1994).
2. W. Lorenzon et al., *Phys. Rev. A* **47**, 468 (1993).
3. Q. Ye et al. (to be published in *Phys. Rev. A*).
4. P.C. Hendry and P.V.E. McClintock, *Cryogenics*, **27**, 131 (1987) and references therein.
5. M.E. Hayden, S.K. Lamoreaux, and R. Golub, AIP Conf. Proc. Ser.: 24th International Conference on Low Temperature Physics (in press).
6. S.K. Lamoreaux et al., *Europhys. Lett.* **58**, 718 (2002).
7. J.J.M. Beenakker, *Physica* **18**, 433 (1952).
8. P.C. Tully, "Isotopic Purification of Helium by Differential Distillation below the Lambda-Point," U.S. Bureau of Mines Report 8054, (Washington, 1975).
9. P.J. Nacher, M. Cornut, and M.E. Hayden, *J. Low Temp. Phys.* **97**, 417 (1994).
10. M.E. Hayden et al., *Phys. Rev. Lett.* **93**, 105302 (2004).
11. See P.J. Shirron and M. DiPirro, *Adv. Cryo. Eng.* **43**, 949 (1998) for an example of a "modern" implementation.
12. D. Candela, M.E. Hayden, and P.J. Nacher, *Phys. Rev. Lett.* **73**, 2587 (1994).
13. V.S. Edel'man, *Cryogenics* **12**, 385 (1972), and P.R. Roach et al., *Jap. J. Appl. Phys.* **26–32**, 1727 (1987).
14. P.V.E. McClintock, *Cryogenics* **18**, 201 (1978).

VII.   Magnets and Magnetic Shielding (WBS 1.5)

Specifications

The nEDM measurement requires a static magnetic field surrounding the two target cells that contain the superfluid ^{4}He, the polarized neutrons and the polarized ^{3}He atoms. The applied static magnetic field, B_0, is chosen to be about 10 mG resulting in a precession of the magnetic moments for both neutrons and ^{3}He nuclei of ~30 Hz. To maintain the polarization of the neutrons and ^{3}He atoms, the magnetic field should be uniform to 0.05% averaged over each cell volume with a time stability of one part in 10^7 over the period of the precession. A separate requirement on the volume-averaged magnetic field gradient in the direction of B_0 of $\langle dB_x/dx \rangle$ < 0.01 μG/cm is necessary to minimize the false EDM signal induced by motional $\vec{B} = \vec{v} \times \vec{E}$ effects. In addition, to reduce the influence of ambient external fields an overall magnetic-shielding factor of ~10^5 is required. The basis for these requirements is summarized in this section and analyzed in detail in the systematic-error discussion in Section VII.A.

Geometry

The current design for the target volume is shown in Figure VII-1. Here a single HV electrode is flanked by two parallel ground plates that provide equal and opposite electric fields over the two cell volumes. The static magnetic field is generated by a saddle-shaped cosθ coil, which gives an iron-free configuration with a sufficiently uniform B_0 magnetic field.
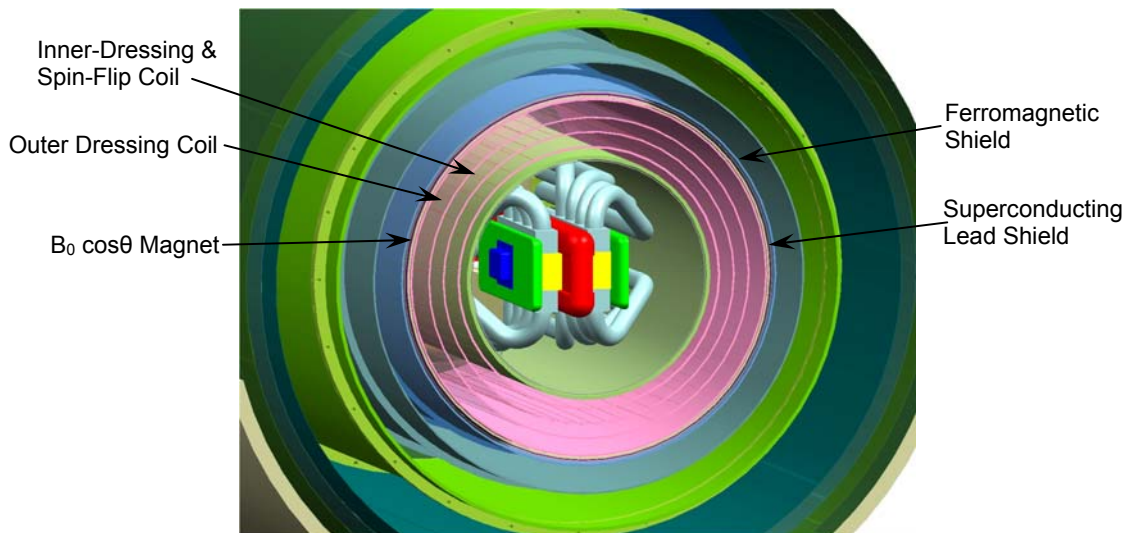
Fig. VII-1.   Schematic diagram of the measurement cell and magnetic coils.

The design also includes a cylindrical ferromagnetic shield just outside of the B_0 coil to improve field uniformity, and a cylindrical superconducting shield to exclude external fields. Interior to the B_0 coil are two additional coils that provide the oscillating B_d field to achieve the dressed spin configuration of the experiment (discussed in Section VII.B). The geometry of all of these coils and shields are listed in Table VII-1. Additional coils (not shown in the figure) include a *π/2* spin-flip coil to rotate the neutron and ^{3}He spins by 90° and several gradient coils to provide well-defined magnetic field gradients in specific directions to study various systematic effects as discussed in Section VII.A. The feasibility of incorporating some of these coils into the structures of the B_0 and B_d coils is under exploration.

Table VII-1. Dimensions of the Magnetic Coils and Low Temperature Magnetic Shielding

Component	Radius (m)	Length (m)
Inner Dressing Coil	0.37	3.96
Outer Dressing Coil	0.48	3.96
$B_0 \cos\theta$ Magnet	0.61	3.96
4K Ferromagnetic Shield	0.62	3.96
Superconducting Shield	0.65	3.96

A. Static Magnetic Field Coils

Magnetic Field Uniformity

As discussed above, there are two independent constraints on field uniformity that drive the design of the B_0 coil. The first involves maintaining the polarization of the neutron and ^{3}He as they precess about B_0. The presence of field gradients transverse to B_0 (assuming B_0 in the x direction) e.g.,

$$\left\langle \left(\vec{\nabla} B_y \right)^2 + \left(\vec{\nabla} B_z \right)^2 \right\rangle \tag{VII.1}$$

coupled with collisions with the walls or other particles introduces depolarization. Such gradients reduce T_2—the transverse relaxation time of the precessing particles. With a field uniformity of 5×10^{-4}, a temperature of 0.3 K, and a B_0 of 10 mG, the T_2 of ^{3}He is about 60,000 s; $T_2 \sim 20,000$ s for the neutrons. These conditions give a 10% loss of polarization of the neutrons during a measurement time of 500 s.

The second constraint on field uniformity comes about because of a new systematic effect identified in the latest measurements at ILL [1,2]. Basically the motional magnetic field $\vec{B} = \vec{v} \times \vec{E}$ can combine with magnetic fields perpendicular to B_0 to give a shift in precession frequency that is linear in $\vec{E}$ and thus produce a false EDM signal. Such perpendicular fields naturally arise from a gradient of the B_0 field along the field direction (e.g., $\delta B_X/dx$). Indeed as shown in References [1,2], it is the volume average of this gradient that generally leads to a false EDM for the neutron. Specifically they derive for the false EDM, d_f

$$d_f = -\frac{J\hbar}{2} \left(\frac{\partial B_x/dx}{B_x^2} \right) \left(\frac{v_{yz}^2}{c^2} \right) \left(\frac{1}{1 - \frac{\omega_r^2}{\omega_0^2}} \right), \tag{VII.2}$$

where J is the spin of the particle, v_{yz} is the particle velocity perpendicular to B_0, ω_0 is the Larmor frequency and $\omega_r = v_{xy}/R$, with R the characteristic size of the apparatus. For $B_0 = 10$ mG and a volume averaged gradient $\delta B_X/dx = 10^{-8}$ G/cm, the false EDM of the neutron is $d_f \sim 1 \times 10^{-28}$ $e\cdot$cm. There is also an effect on the faster moving ^{3}He that, according to the above formula, can be significantly larger. However References [1,2] also pointed out that this effect can be substantially reduced if collisions of the ^{3}He with phonons occur on a time scale short compared to the Larmor precession time. For temperatures of $\sim$0.4–0.6 K, it appears that the effect can be reduced below that of the neutron. Thus, for the magnetic-field design, the neutron is assumed to set the specification on the $\delta B_X/dx$ gradient.

Design of the B_0 Magnet Coil

Initial designs of the B_0 magnet [3] were performed using the ANSYS 5.7 finite-element modeling code and assumed a standard cylindrical cosθ type of magnet (see Figure VII-2). Several promising solutions were identified and discussed in the EDM preproposal. In these designs, access to the measurement cells (required for the HV electrode, [3]He and [4]He injection, the cold-neutron beam, and extraction of the scintillation light) was obtained between the turns of the magnet. More recent studies have indicated that sufficiently uniform fields can also be obtained with open ends of the cylinder with the coils in a so-called saddle-shape as shown in Figure VII-2. In this design, the coils are carried along the circumference of the endcaps of the cylinder (rather than across the endcaps), leaving open access to the interior through these endcaps. This geometry has significant advantages compared to the standard coil. Besides providing larger-area access to the measurement cells, by concentrating most of the access to the measurement cells through the endcaps, there is less of a need for penetrations in the superconducting (and ferromagnetic) shields which can dramatically perturb the magnetic field uniformity in the measuring cells.
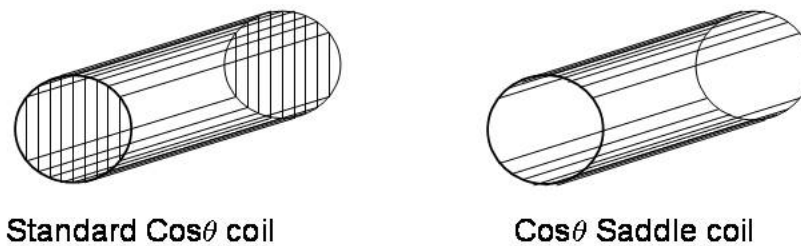

Standard Cos*θ* coil   Cos*θ* Saddle coil

Fig. VII-2.   Coil winding for a standard cosθ coil and for a cosθ saddle coil. Both coils produce a largely horizontal magnetic field.

Several approaches have been used to optimize the design of the B_0 coil. These include analytic studies to identify key dependences, direct integration of the Biot-Savart equation for bare coils and the finite element code TOSCA for calculations of the coil inside a ferromagnetic shield. In addition several small-scale prototypes have been built and tested.

The Biot-Savart integration has been used to compare the standard cosθ coil to the cosθ saddle coil. This comparison is shown in Figure VII-3 for the full-scale coil needed for the EDM experiment. In the comparison, the number of turns for each coil has been separately optimized for the two cases, resulting in $N = 22$ for the standard and $N = 34$ for the saddle coil. It should be pointed out the aspect ratio of the coils ($L/R = 6.4$) has been chosen to provide improved uniformity for the saddle coil.

The full TOSCA finite-element calculations have only recently commenced, but some preliminary results have been generated to show the improvement in the uniformity that can be obtained with a ferromagnetic shield surrounding the cosθ coil. In the original design discussed in the preproposal, a superconducting shield surrounded the cosθ coil. Unfortunately, due to the boundary conditions at the superconductor, the inclusion of a cylindrical superconductor results in mirror currents being generated in the superconductor that oppose the currents in the cosθ coil resulting in a reduction of the central field at a fixed current and a worsening of the field uniformity. In contrast, the boundary conditions for a ferromagnetic cylinder result in mirror currents that add to the field from the cosθ coil improving the uniformity.
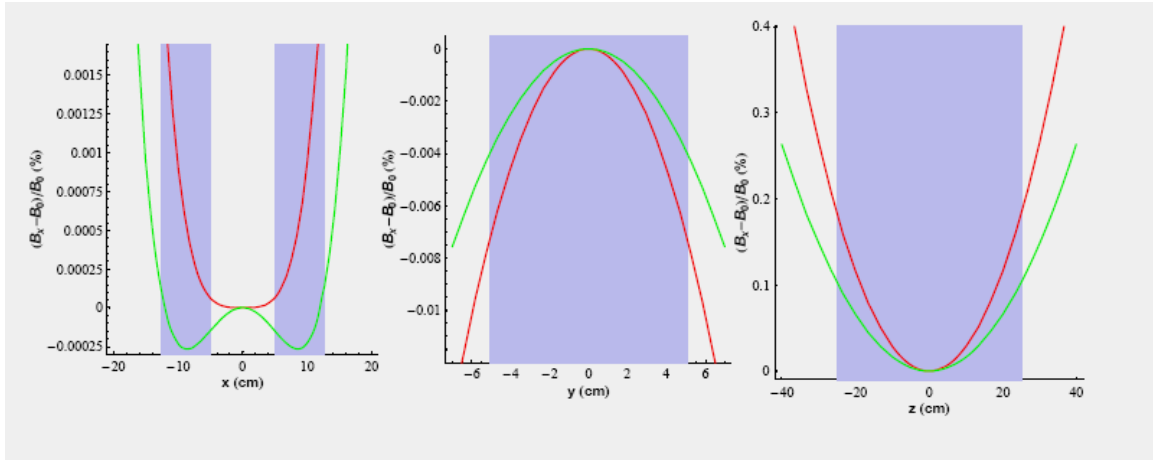
Fig. VII-3.   Comparison of a standard cosθ coil (red curve) with number of turns N = 22 and a cosθ saddle coil (green curve) with N = 34. The variation of the dominant component of the field, B_x, is plotted in each case vs x, y, and z.

   To test these concepts some initial TOSCA calculations have been undertaken. These calculations have been done for a small-scale prototype coil (~1/8 scale) that has been constructed. The implementation of the prototype coil into TOSCA is shown in Figure VII-4. The improvement in uniformity due to the inclusion of the ferromagnetic shield is shown in Figure VII-5. While there is a modest improvement in uniformity along the *x* and *y* direction, there is a significant improvement of the uniformity in the longitudinal direction (the *z* direction).

Results

   Many variations in the geometric parameters of the B_0 coil have been studied. Because of the large time required to perform the full TOSCA calculations, the focus has been on fast optimization of coil geometries without a ferromagnetic shield. The justification for this approach is based on the obvious improvement obtained with a ferromagnetic shield as shown above. Thus if a coil configuration is identified that satisfies the specifications of the EDM experiment without the ferromagnetic shield it should be further improved with the inclusion of the shield.
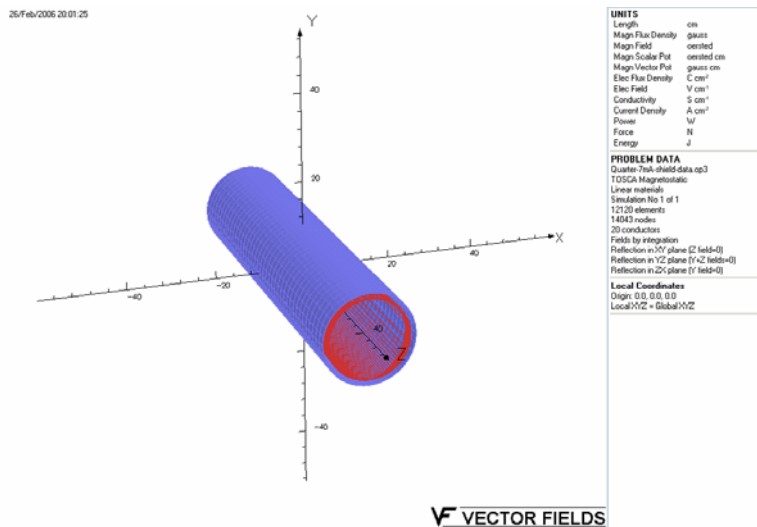

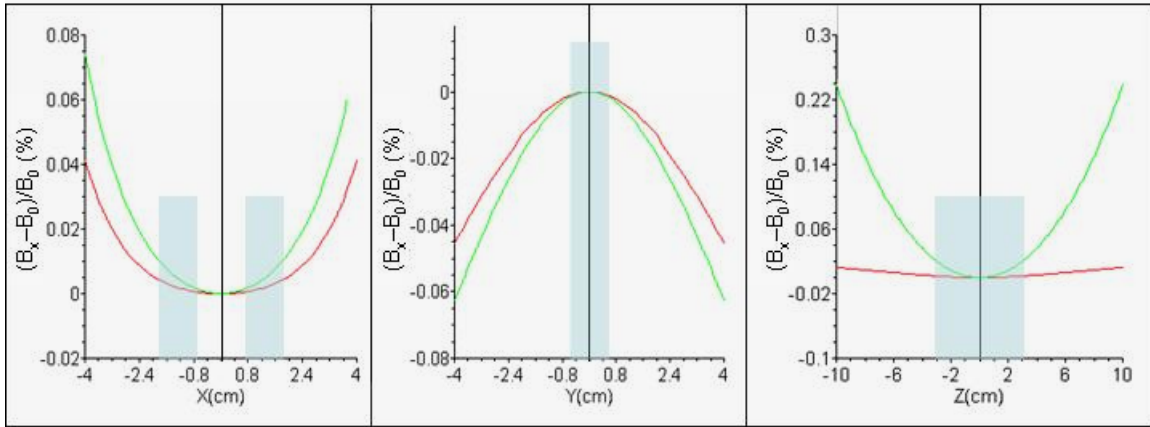Fig. VII-4.   Geometry of the prototype coil as implemented in TOSCA.

Fig. VII-5.   TOSCA calculations of magnetic-field variation for a bare cosθ coil (green line) and for a cosθ coil inside a ferromagnetic shield (red line). The calculation was performed for a prototype coil (~1/8 scale). The shaded regions represent the scaled measurement-cell volumes.

Based on this approach, we have optimized the field from a cosθ saddle coil to provide a uniformity < 0.1 % while simultaneously providing a longitudinal gradient $\delta B_X/dx < 0.01$ μG/cm. For $L/R = 6.4$ and $N = 34$ turns, we obtain a worst-case uniformity of 0.05% with a longitudinal gradient $\delta B_X/dx = 0.007$ μG/cm. The uniformity goals for the static B_0 fields adopted for this nEDM experiment have been demonstrated to be attainable. Although this design is expected to be further optimized, this study provides an existence proof that the design goals can be met.

Additional Static Coils

In addition to the B_0 coil discussed above, several other coils must also be fabricated. These are the polarized-[3]He-holding field coil and the gradient coils for B_0. For the polarized [3]He injection into [4]He, a uniform holding field is required to maintain the polarization of the [3]He before its transfer to the measurement cell. This field will be produced with another cosθ magnet that has a similar aspect ratio (L/R) to the B_0 coil. Gradient coils will also be fabricated in order to apply controlled gradients to the constant-field B_0 coil. These gradients are useful to study systematic effects associated with the false EDMs produced by the accumulation of geometric phase discussed above. A *z* gradient will be provided by a pair of anti-Helmholtz coils of similar radius to the B_0 coil. For gradient in the *y* direction, we can use several additional windings on the B_d coils that can be energized separately to create the gradient. A similar effect for the *x*-direction gradient can be achieved by additional windings on the B_0 coil.

Time Stability of the Magnetic Field

Time stability in the B_0 field is crucial to the success of the measurement. The 10 mG B_0 field generates a precession frequency of ~30 Hz. The precession frequency sensitivity from each measurement cycle is of the order of ~3 μHz. Thus, the B_0 field must be stable to less than one part in 10^{-7} over one period of the precession (~0.03 s). This type of current stability has been demonstrated recently [4].

B. Time Varying Magnetic Field Coils

π/2 Spin Rotation Coil

Following the diffusion of the polarized ^{3}He atoms into the measurement cells and production of the UCN via illumination of the cells with the polarized 8.9 Å cold-neutron beam, the neutron and ^{3}He spins will be aligned with the primary B_0 field direction along the x axis. The function of the $π/2$ coil is to apply a $π/2$ pulse to the neutron (gyromagnetic ratio γ_n) and ^{3}He (γ_3) spin ensembles that, when appropriately tuned, will simultaneously rotate both the neutron and ^{3}He spins into the perpendicular (y-z) plane for the precession frequency measurements.

An outline of the solution to the problem of determining the appropriate frequency and duration for the $π/2$ pulse is as follows. The B_0 field is clearly of the form

$$\vec{B}_0 = B_0\hat{x} \ . \tag{VII.4}$$

(For $B_0 > 0$, it is worth noting that the neutron or ^{3}He spin along the y-z plane will precess about the x axis in the *clockwise* sense at the Larmor frequency of $\omega_0 = |\gamma|B_0$.) We write the $π/2$ coil field as

$$\vec{B}_1(t) = 2B_1\cos(\omega_1 t)\hat{z} \ , \tag{VII.5}$$

which can be rewritten as

$$\vec{B}_1(t) = B_1\left[\sin(\omega_1 t)\hat{y} + \cos(\omega_1 t)\hat{z}\right] + B_1\left[-\sin(\omega_1 t)\hat{y} + \cos(\omega_1 t)\hat{z}\right]. \tag{VII.6}$$

The above can be interpreted as the sum of one field rotating clockwise about the x axis (first term on the right-hand side), and another rotating counterclockwise (second term). We then move into a reference frame rotating in the clockwise sense about the x axis at the frequency ω_1 (the so-called "rotating frame"), and define a $\left(\hat{x}' = \hat{x}, \hat{y}', \hat{z}'\right)$ coordinate system for this rotating frame, with the $\hat{y}'$ and $\hat{z}'$ axes rotating about the x axis at this frequency ω_1. The field rotating clockwise in the laboratory frame will appear static in the rotating frame, $(B_1)\hat{z}'$, whereas the field rotating counterclockwise in the laboratory frame will still appear to be rotating in the counterclockwise sense about the x axis, but now at a frequency of $2\omega_1$.

For the case of a single-particle ensemble, if the frequency, ω_1, is tuned exactly to the resonant frequency $\omega_1 = \omega_0 = \gamma B_0$, the "effective" magnetic field in the rotating frame along the x axis, $(B_0 - \omega_1/\gamma)$, will be zero. The only remaining static-field component in the rotating frame is then the $(B_1)\hat{z}'$ field component, about which the spin will precess at a frequency of γB_1. The duration of the pulse, τ, is then chosen so that $(\gamma B_1)\tau = π/2$. Here, the field rotating in the counter-clockwise sense at a frequency of $2\omega_1$ has been ignored, an approximation termed the "rotating-wave approximation", valid for $B_1 \ll B_0$.

For the more complicated case of the neutron and ^{3}He spin ensembles, because $\gamma_n \neq \gamma_3$, it is not possible to choose a frequency ω_1 that simultaneously nulls the effective magnetic field along the x axis for both species. Instead, after moving into the rotating frame, the neutron and ^{3}He spins precess at different frequencies, ω_n' and ω_3', respectively, about different effective static magnetic fields, both with nonzero $\hat{x}'$ and $\hat{z}'$ components. Written explicitly, the field experienced by the neutrons is

$$\vec{B}_n' = (B_0 - \omega_1/\gamma_n)\hat{x}' + (B_1)\hat{z}' \ , \tag{VII.7}$$

with a similar expression ($\gamma_n \rightarrow \gamma_3$) for the ^{3}He atoms. We define *tan(θ'_n)* and *tan(θ'_3)* to be the ratio of the $\hat{x}'$ and $\hat{z}'$ field components.

Determination of the appropriate parameters for the $\pi/2$ pulse is then simply a matter of geometrical considerations, as one must evaluate the precession of the spins, initially aligned along the *x* axis, about their respective effective magnetic fields. Simultaneous rotation of both the neutron and ^{3}He spins into the *y-z* plane can be achieved if a time can be found when the $\hat{x}'$-components of both spins are zero. Working through the geometry, this condition can be satisfied if there exists a time, τ, and frequency, ω_1, such that

$$\cos(\omega'_n \tau) = -\tan^2(\theta'_n) \text{ and } \cos(\omega'_3 \tau) = -\tan^2(\theta'_3) \,. \tag{VII.8}$$

Here, $\omega'_n = |\gamma_n| \cdot |\vec{B}'_n|$, with a similar expression for ω'_3. It should be noted that no solution exists if either $\tan^2(\theta'_n)$ or $\tan^2(\theta'_3) > 1$. Besides the obvious trigonometric reason for this constraint, this condition can also be understood intuitively by realizing that if either $|\theta'_n|$ or $|\theta'_3| > 45°$, the cones swept out by the spin-components perpendicular to $\vec{B}'_n$ or $\vec{B}'_3$ will never intersect the *y-z* plane. The problem then reduces to a numerical solution of the above equations for τ and ω_1 given a value for B_0, here taken to be 10 mG. A solution exists if $B_1/B_0 \geq 0.054$. At this limiting value for B_1/B_0 (weak influence of B_1 relative to B_0 and region of applicability for the rotating-wave approximation), $\omega_1 = 2\pi \times (30.66 \text{ Hz})$ is nearly equal to the average of the neutron (29.17 Hz) and ^{3}He (32.43 Hz) precession frequencies. The duration of the pulse for this choice of ω_1 is $\tau = 0.192$ s. This field will be generated by a separate cosθ-coil winding mounted on the main B_0 cosθ-coil support structure at a relative orientation of 90°.

Dressed-Spin Coils

In addition to the use of the SQUID system to monitor the polarized ^{3}He, a dressed-spin measurement system is to be implemented in the experiment [5]. In this technique, an alternating current (AC) magnetic field is introduced in addition to the constant field, B_0, the effect of which is to change the effective magnetic moments of the neutrons and ^{3}He atoms:

$$\gamma_{eff} = \gamma_0 J_0 \left(\frac{\gamma_0 B_{AC}}{\omega_{AC}} \right), \tag{VII.9}$$

where γ is the gyromagnetic ratio and J_0 is the ordinary Bessel function of zero order. Thus, the effects of variations in the ambient magnetic field can be substantially reduced by making the effective neutron and ^{3}He magnetic moments are equal

$$\gamma_{0,3} J_0 \left(\frac{\gamma_{0,3} B_{AC}}{\omega_{AC}} \right) = \gamma_{0,n} J_0 \left(\frac{\gamma_{0,n} B_{AC}}{\omega_{AC}} \right) \Rightarrow \frac{\gamma_{0,n} B_{AC}}{\omega_{AC}} = 1.19, \tag{VII.10}$$

which defines a critical AC frequency. Small random or systematic changes in B_0 dictate that the AC frequency be 100 or more times the nominal precession frequency; the value $\omega_{AC} = 2\pi$ (3 kHz) is chosen. At the critical AC frequency, the n-^{3}He capture rate decreases to zero. In practice, the AC frequency is swept about the critical value to determine the neutron precession rate separately for each state of $\vec{E} \cdot \vec{B}$. During the experiment, both methods (dressed-spin and SQUID measurements) are used to determine the EDM signal.

In order to implement the dressed-spin technique, a pair of additional cosθ coils are added to produce the required AC field perpendicular to the holding field:

$$\vec{B}_0 = B_0 \hat{x}, \qquad \vec{B}_{AC} = B_{AC} \hat{y} \,. \tag{VII.11}$$

The neutron beam axis is along $\hat{z}$.

The implementation of a pair of $\cos\theta$ dressing coils with opposite currents has been studied to reduce the heat dissipation due to eddy currents induced by the alternating magnetic field in the ferromagnetic shield, which is the largest conductor in the vicinity of the measurement cells. The currents in the coils can be tuned in such a way that the magnetic field at the surface of the ferromagnetic shield is approximately cancelled by the opposing coils while still yielding a uniform field in the volume of the measurement cells. According to the specifications discussed above, a dressing coil should produce a uniform field of $|B_{AC}| \sim 1$ G in the measurement cells. The corresponding oscillation frequency of the field is then $\omega = 2\pi = 3$ kHz.

It is important to limit the amount of heat generated in the ferromagnetic-shield volume that is at $T = 4$ K. The worst-case maximum-power dissipation in the ferromagnetic shield due to the dressing coils is estimated by calculating the effect of a magnetic field on a conductor of permeability μ. As a first approximation, the value of the field at the surface of the ferromagnetic shield is taken to be the magnitude of the net field in the absence of the shield. The time averaged power per unit area $P_{resistive}$ due to a field H_0 is then [6]

$$\frac{\mathrm{d}P_{resistive}}{\mathrm{d}A} = \frac{1}{4}\mu\omega\delta|H_0|^2 \,. \tag{VII.12}$$

where δ is the material skin depth which depends on the conductivity and the frequency. To indicate the need for careful optimization of the dressing coil design, a single 30-turn $\cos\theta$ coil of radius $R_1 = 35$ cm, length $L_1 = 225$ cm with a field $|B_{AC}| = 1$ G in the measurement cells is considered. Over the internal surface of the ferromagnetic shield, this configuration leads to $\sqrt{\langle|B_{AC}|^2\rangle} = 229$ mG, with a resulting heat dissipation of ~ 19.7 W. This load is well beyond the heat budget for the 4 K cooling capability of the experiment. The corresponding current necessary to induce the magnetic field is $|I_{AC}| = 3.56$ A.

In order to improve upon this heat load, an initial optimization of the coil design for the dressing coils has begun. As an example, for a dressing-coil pair, the power dissipation for a pair of 40-turn $\cos\theta$ coils with radii $R_1 = 34$ cm, $R_2 = 47$ cm and length $L_{1,2} = 396$ cm is estimated. In this configuration, the field is uniform up to 0.08% inside the measurement cells as required to maintain a reasonable T_2 for the neutrons and ^{3}He (see discussion above). Because of the high frequency of the dressing-coil oscillations, it is likely that the geometric phase effects will not significantly limit the longitudinal gradient from these coils. The resulting power dissipation over the internal surface of the ferromagnetic shield is ~ 1.7 W for an average field $\sqrt{\langle|B_{AC}|^2\rangle} = 66.1$ mG. The currents required for such coil configuration are $|I_{1\,AC}| = 5.62$ A and $|I_{2\,AC}| = 4.04$ A. This power dissipation is barely tolerable, thus additional optimization would be prudent in order to reduce the power level to < 0.5 W.

For the same reason, the AC fields also set limits on the (minimum) resistance of the conductive coating for the electric field electrodes ($T = 0.3$ K) at about 1 Ω (or a resistivity of ~ 100 m$\Omega\cdot$cm). The conducting coating on the electrodes cannot, in any case, have very low resistance because of the thermal magnetic field noise requirements of the SQUIDs. This combination of coils and shields will preserve both the SQUID method and the dressed field method for measuring the neutron spin precession in a controlled magnetic-field environment.

C. Magnetic Shields

Room-Temperature Shields

The experimental apparatus is enclosed within a 4-layer conventional magnetic shield (μ-metal) designed to shield the experiment from the Earth's magnetic field and other (possibly time-varying) background fields. A schematic diagram of the 4-layer structure is shown in Figure VII-6. As indicated there, the shielding surrounding the lower cryostat will consist of two assemblies of 9 and 8 cylindrical panels, each spanning 40° and 45° in the circumferential direction, for the two outermost and two innermost layers, respectively. The size of these panels is constrained by the dimensions of the commercially available material sheets (3' × 12') and the size of the annealing oven (5' diam × 12' depth). The shielding for the lower and upper cryostats will be joined via a connecting "tee", shown in this figure as an assembly of 8 such panels, with this "tee" comprising most of the shielding structure for the upper cryostat. The end-caps are shown as "conical snouts" (i.e., not flat surfaces at 90°), for purposes of magnetic continuity. The material thickness for each layer has been chosen to be 0.062".
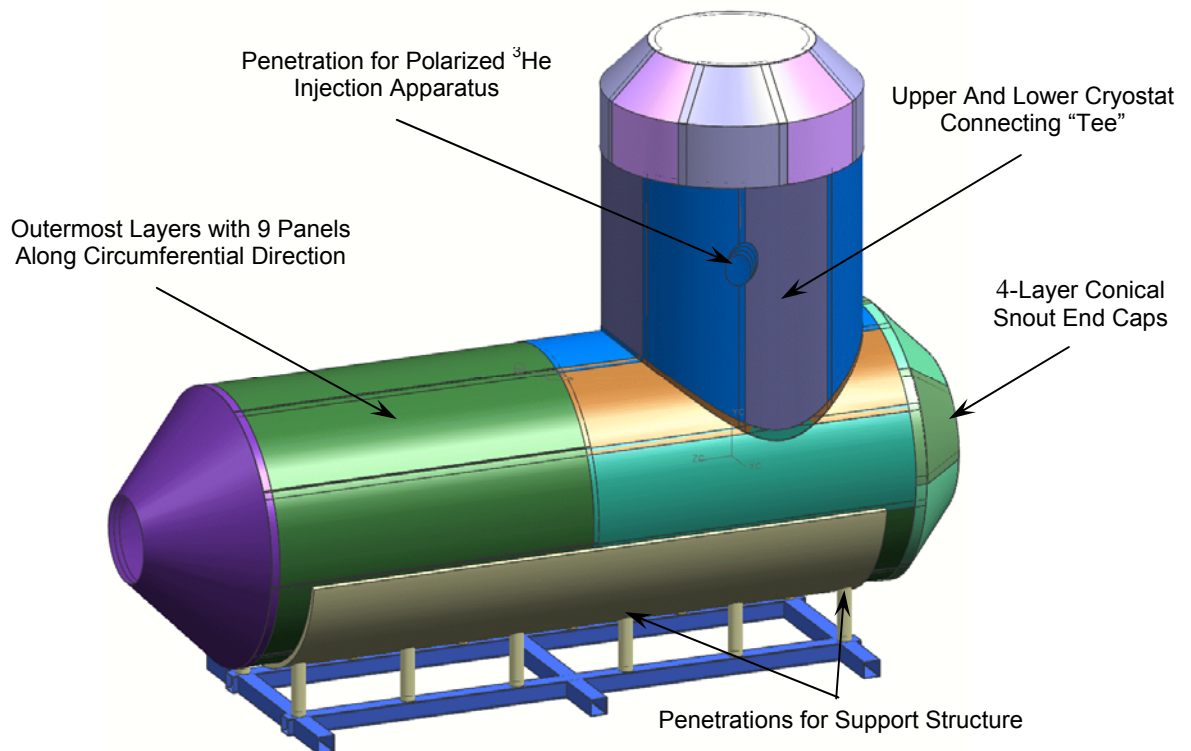
Fig. VII-6.   The four-layer conventional magnetic shielding structure.

Several penetrations through the shielding structure are necessary. In addition to the penetration required for the incident cold-neutron beamline, penetrations through the lower cryostat shielding are required for the experimental support structure (as shown in Figure VII-6), and a penetration through the upper cryostat shielding is required for the polarized ³He injection apparatus. To minimize the impact of these penetrations, multilayer μ-metal tubes, and possibly solenoidal windings, will surround the openings.

A support structure (fabricated from aluminum) integrated with the support structures for the lower and upper cryostats is required to minimize stress on the μ-metal panels, as stress or strain on the material will degrade its shielding performance. Cylindrical aluminum or other

nonmagnetic material spacers will fill the regions between the layers and will be fabricated in a modular fashion similar to that for the μ-metal panels.

The shield and the support structure will be designed so that they can be assembled in a modular fashion. For example, the lower cryostat shielding surrounding the measurement cells may be assembled and installed before the rest of the shielding. Following installation of the lower cryostat and magnet infrastructure, the rear portion of the lower cryostat shielding, the connecting "tee", and the shielding for the upper cryostat may be installed as separate pieces. The design will also have to accommodate the need to remove the rear end-caps in a safe manner to provide access to the lower cryostat and measurement cell regions when necessary. Finally, battens tightened with aluminum screws and/or clamps will be used to provide overlapping magnetic seals across the seam lines between the many panels.

Inner Cryogenic Shields

The magnets surrounding the measurement cells will be mounted within a 4 K shielding enclosure consisting of a superconducting shield and a ferromagnetic shield. As described earlier in this document, the superconducting shield is needed to isolate the SQUIDs from residual background fields. The superconducting shield will consist of a thin lead sheet ($T_c = 7.2$ K) cast onto a support structure frame fabricated from aluminum.

The ferromagnetic shield as mounted within the superconducting shield provides the necessary boundary conditions for the main B_0 field. In particular, the boundary conditions for a superconducting shield demand that the entire field vanish at the surface of the superconductor. In contrast, the boundary conditions at the interface between a high-permeability ($\mu \gg 1$) ferromagnetic material and vacuum demand that the perpendicular component of the field be continuous, whereas the parallel component must vanish (suppressed by a factor of $1/\mu$); therefore, a ferromagnetic shield nested within a superconducting shield is much more suitable for obtaining the requisite B_0 field uniformity. As discussed above, preliminary FEA calculations carried out with the TOSCA code have suggested that mirror currents in a ferromagnetic shield (without end-caps) induced by the currents in the $B_0 \cos\theta$ coil windings will improve the field uniformity along the relevant x-coordinate direction.

A likely material to construct the 4 K ferromagnetic shield is Cryoperm, a proprietary high-nickel-content alloy that is hydrogen annealed according to a special temperature cycle to provide a high shielding factor at cryogenic temperatures. Unlike μ-metal, which is well-known for its decreasing permeability with decreasing temperature, the magnetic properties of Cryoperm at 4 K are similar to those at room temperature. Another promising material is Metglas an amorphous metal that also maintains very high permeability at low temperature.

The ^{3}He spin-holding $\cos\theta$ coil mounted within the upper cryostat will also be enclosed within a low-temperature ferromagnetic shield. This shield will serve to improve the field uniformity from this coil, and also to increase the total shielding factor for the volume within the ^{3}He injection and transport regions to a level similar to that for the regions surrounding the measurement cells.

Shield Degaussing System

For optimal shielding performance, the four-layer conventional magnetic shield and the inner ferromagnetic shields must be degaussed after any changes in the ambient background fields or the inner magnetic fields (e.g., a power cycling of the main $B_0 \cos\theta$ coil). Degaussing of a magnetic shield is customarily done by applying an alternating field with sufficiently large amplitude to drive the material to saturation, and then slowly decreasing the amplitude to zero. A degaussing system similar to those employed and described by a past neutron-antineutron oscillation experiment [7] and a past nEDM experiment [8] will be installed, with AC current

supplied by computer-controlled high-power power supplies driven through toroidal coils wound around sections of the shielding layers. It should be noted that because the skin depth decreases as $1/\nu^{1/2}$, a 60-Hz degaussing cycle may need to be followed by a low frequency (~1 Hz or less) degaussing cycle, similar to the procedure described in [7].

Estimated Shielding Factors

Very preliminary estimates of shielding factors for the lower cryostat and upper cryostat shielding have been carried out with analytic [9] and FEA (TOSCA) techniques. These calculations considered the shielding for the lower and upper cryostats separately, and ignored the presence of the superconducting shield, the connecting "tee", the end-caps, and all penetrations. The transverse shielding factors estimated by both techniques are on the order of a few $\times 10^5$. In the future, a full-model of the shielding structure (i.e., end-caps, penetrations, etc.) will be built within TOSCA.

References

1. M. Pendlebury et al., *Phys. Rev. A* **70**, 032102 (2004).
2. S.K. Lamoreaux and R. Golub, *Phys. Rev. A* **71**, 032104 (2005).
3. R. Mischke, Report on ANSYS Model Results, February-March, 2002, [http://p25ext.lanl.gov/~mischke/edm/edm_ppt.html].
4. C. Ciofi et al., *IEEE Trans. Instrum. Meas.* **47**(1), 78 (1998).
5. R. Golub and S.K. Lamoreaux, *Phys. Rep.* **237**, 1 (1994).
6. J.D. Jackson, *Classical Electrodynamics*, 3rd Ed. (John Wiley and Sons, New York, 1999).
7. T. Bitter et al., *Nucl. Instrum. Methods Phys. Res. A* **309**, 521 (1991).
8. I.S. Altarev et al., *Phys. Atom. Nucl.* **59**, 1152 (1996).
9. T.J. Sumner, J.M. Pendlebury, and K.F. Smith, *J. Phys. D* **20**, 1095 (1987).

VIII. The Central Detector Systems (WBS 1.6)

The central detector system (CDS) is situated at the heart of the experiment, and includes the measurement cells, the scintillation-light transport and detection system, the SQUID magnetometers, the beam stop and neutron shield, and the HV system. A schematic is shown in Figure VIII-1. Two measurement cells are placed in the gaps between the HV and ground electrodes, as shown in Figure VIII-2. Each cell is a rectangular acrylic tube of a dimension of 7.62 cm × 10.16 cm × 50 cm. The 8.9 Å neutron beam enters parallel to the long axis of the cell and is absorbed outside the cell in a beam stop made of a neutron-absorbing material such as boron nitride. Connected to the side walls of the measurement cells are the light guides, which transport signal light from the measurement cells through the cryogenic feedthrough on the end cap to the photomultiplier tubes (PMTs). The HV electrode is connected to the HV gain capacitor, which is supported by the end cap. Mechanically, the CDS is supported by the end cap, which houses all the services and feedthroughs. The CDS is enclosed in a cylinder that serves as the return electrode; the cylindrical insert slides into the lower cryostat. The end cap is the part of the container that seals the 300 mK LHe volume.

The measurement cycle is described in detail in Chapter VI. Here, the steps that are relevant for discussing the CDS are briefly described. The measurement cells are initially filled with isotopically pure superfluid ^{4}He at ~300 mK. Then polarized ^{3}He atoms are injected into the measurement cells by opening the ^{3}He valve on the cell wall to the ^{3}He injection system. The spin of the ^{3}He is parallel (or antiparallel) to the electric and magnetic fields. The cells are irradiated with the 8.9 Å polarized neutron beam and polarized UCNs are produced via the superthermal process inside the measurement cell. The spin of the UCN is parallel (or antiparallel) to the electric and magnetic fields. After the beam is turned off, an RF pulse is applied to rotate the spins of the UCN and ^{3}He atoms by 90° so that they precess in the plane perpendicular to the electric and magnetic field. Then a measurement begins. The spin precession of the ^{3}He atoms is monitored by the SQUID magnetometers. Note that there are ~10^{12} ^{3}He atoms/cm^3, whereas there are 150 UCNs/cm^3. Therefore, the SQUID signal is dominated by the signal due to ^{3}He magnetization. The UCN spin precession is measured using the spin-dependent UCN/^{3}He capture process. When UCNs are captured on ^{3}He, scintillation light in the extreme ultraviolet (the spectrum is centered at ~80 nm) is produced. This light is converted to visible wavelengths and transported through the light guides to PMTs. The measurement is continued for ~500 s until the UCN density in the cells decays due to capture on ^{3}He, wall loss, and β decay. Then, the ^{3}He valve is opened to the ^{3}He purifier system to remove ^{3}He atoms by diffusion to the purifier.

During this process, a high electric field (50 kV/cm) is maintained between the electrodes. The electric field is generated by the variable capacitor that is placed in parallel with the main electrodes. The variable capacitor is charged by an external HV power supply when the capacitance is large. Then the connection to the external HV power supply is disconnected and the voltage is amplified by increasing the separation between the electrodes of the variable capacitor, thus lowering the capacitance of the variable capacitor.

When the measurement cells are irradiated by the 8.9 Å neutron beam, only a small fraction (~10^{-5}) of the incident cold neutrons get down-scattered and become UCNs. While most of the neutrons just pass through the measurement cells and get absorbed by the beam stop, a large number of neutrons get scattered at the beam window, the cell walls, and the helium volume. The scattered neutrons are captured by the various materials that make up the apparatus, activating the materials and turning them into a source of background. Although it is important to avoid, as much as possible, using materials that get activated by exposure to a neutron field, it is

also important to remove unwanted neutrons that may activate the surrounding materials. For this purpose, neutron shielding will be installed at appropriate places.
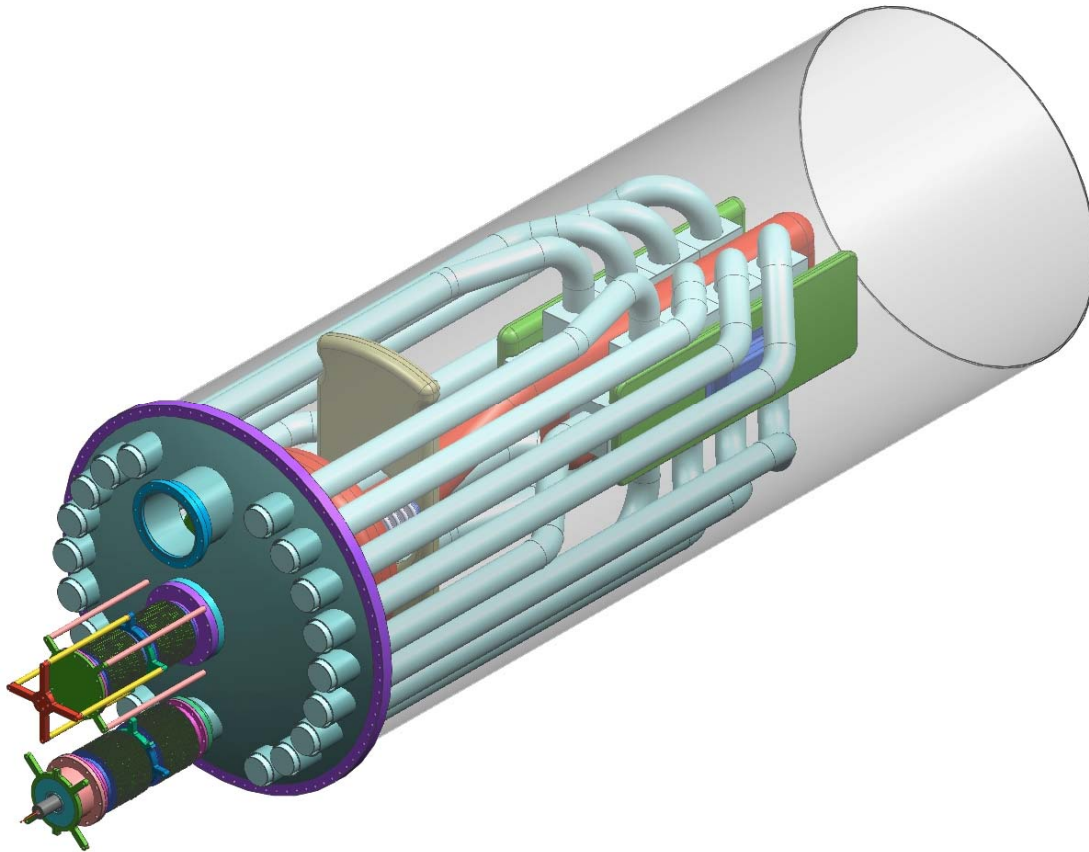
Fig. VIII-1. Schematic of the central detector systems

In addition to the ^{3}He/neutron-capture events, other classes of events give rise to an emission of scintillation light in LHe, such as neutron β decay, radiation from the material around the measurement cells activated by neutrons, and cosmic rays. While it is possible to reduce background events due to the activation and to externally veto cosmic-ray-induced events, it is not possible to reduce or externally veto β decay events. Therefore, an ability to distinguish different types of events or to identify the types of particles that generated the scintillation (PID) is imperative in achieving the maximum sensitivity. We plan to utilize the afterpulsing of the LHe scintillation [1]. A charged particle traveling through LHe generates exited helium molecules in the singlet and triplet states. The de-excitation of these molecules is responsible for the scintillation light. The singlet and triplet states have significantly different decay time: molecules in the singlet state decay in about 1 ns whereas the radiative lifetime of the triplet state molecule is much longer. The relative population of the singlet and triplet states depends on the ionization density. The afterpulsing (single photon events due to the de-excitation of the triplet states) is significantly weaker for electrons than that for α particles or neutron captures on ^{3}He. Therefore by detecting the afterpulses following the prompt scintillation, one can distinguish the neutron capture on ^{3}He from both neutron β decay and events due to γ rays from activated material around the measurement cells (see Figure III-5). In order for this method to work optimally, we will need ~40 photoelectrons per event.
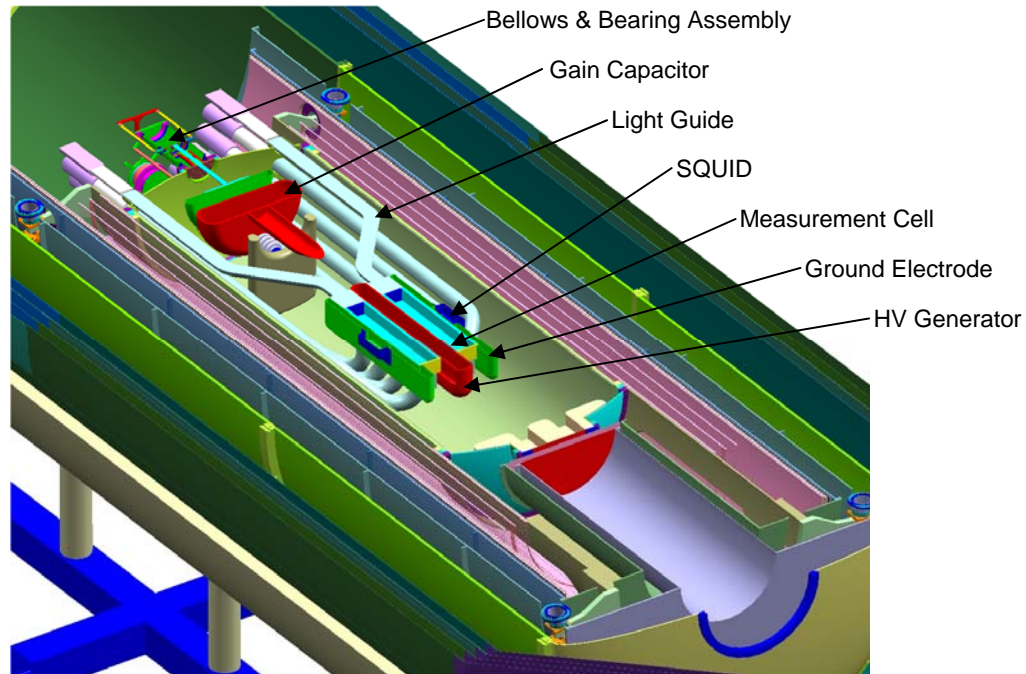
Fig. VIII-2.   Reference design for the electric field plates and gain capacitor.

A. Measurement Cells and ^{3}He Valves

The measurement cells serve various functions: they hold the superfluid LHe in which UCN are produced from the 8.9 Å neutron beam via the superthermal process. They store the produced UCNs, maintaining their polarization. At the same time, they allow injection of polarized ^{3}He atoms into the superfluid LHe volume, and store the ^{3}He atoms, maintaining their polarization. In addition, they serve as a detector for the neutron/^{3}He-capture events by down-converting extreme ultraviolet scintillation light from LHe into visible light and then transmitting it to the light guide that is attached to the cells. These lead to a number of stringent requirements for the cell design:

(1) The cell walls must be coated with a material that has a low UCN loss rate, a low UCN depolarization rate, and a low ^{3}He depolarization rate.
(2) The cell wall coating must serve as a wavelength shifter for hard ultraviolet light.
(3) The cells must have a valve to allow injection of polarized ^{3}He atoms and the valve must be ^{3}He tight as well as UCN tight.
(4) The cells must be made of material that is transparent to visible light so that the visible light from the down conversion of the extreme ultraviolet light can be transmitted to the light guide.
(5) The cells must be made of material that allows the neutron beam to pass through with minimum activation due to neutron capture.
(6) The cells must be made by materials that satisfy the cryogenic requirements.
(7) The inner cell walls adjacent to the electrodes must be able to bleed off electric charge.

Based on the experience from the NIST Neutron Lifetime Experiment [2], we plan to use UVT acrylic as the cell wall material. We plan to coat the cell wall with deuterated polystyrene (DPS) doped with the deuterated wavelength shifter, dTPB (deuterated 1,1,4,4-tetraphenyl buta-1,3-diene).

The application of DPS as a wall-coating material for UCN storage dTPB is described in Reference [3]. Reference [3] also discusses some properties of DPB as a wall-coating material

for UCN storage, including the effective potential which that has been measured to be 165 neV. Cells made of DPS-coated acrylic are expected to provide a UCN storage time approaching the neutron lifetime (in the absence of ^{3}He) and to preserve the UCN polarization upon reflection from the wall. In Chapter III, preliminary storage-time measurements are described.

The wall-coating material must also be compatible with a long relaxation time for the spin of the ^{3}He atoms. The wall relaxation time of the DPS coating for ^{3}He is expected to be sufficiently long, but tests are required to demonstrate it. Tests have been carried out down to 1.9 K by the collaboration, and a relaxation time of about 2000 s has so far been achieved with an acrylic cell coated with dTPB-loaded DPS as noted in Chapter III. Tests at lower temperatures are planned for the near future.

dTPB converts the LHe scintillation light emitted in the extreme ultraviolet wavelength (~80 nm) to visible wavelengths. This material is used in the NIST Neutron Lifetime Experiment [2], and a conversion efficiency of ~0.3 has been measured [4].

There must be a valve for each cell, which opens to inject ^{3}He atoms into the cell and to remove ^{3}He after each measurement. Many considerations enter into the valve design. The ^{3}He and UCN depolarization rates should not be affected by the presence of the ^{3}He lines connected to the cells. This requirement implies that the valve is located on the cell wall and that part of the cell wall act as a "door" so that, when the valve is closed, there is no hole on the cell wall. In order for the presence of the valves not to disturb the static electric field, the valves must be on the wall that is attached to the ground electrode. Furthermore, part of the ground electrode must also act as a "door." The "door" part of the ground electrode opens when the valve is open, and forms part of the electrode when the valve is closed. When in the closed position, it should make electrical contact with the rest of the ground electrode. The actuator for the V1 valves is described in Section VI.

B. Light Guides and PMT's

The visible light emitted from the conversion of extreme ultraviolet light in the dTPB in the coating of the measurement cells is transported through the light guides to the PMTs. In order for the PID scheme to work optimally, at least 40 photo-electrons are needed for events with a 780 keV energy deposition in LHe. The NIST lifetime experiment provides valuable experience. They used an acrylic cell coated with TPB coupled to light guides that transported the light to the room temperature PMTs. They obtained 6.0 photo-electrons for a 360 keV energy deposition [2], which corresponds to 12 photo-electrons for a 780 keV energy deposition. A three to four fold improvement is needed over what the NIST Neutron Lifetime Experiment achieved.

Currently various light-collection/-detection schemes are under consideration. One possible scenario is described here to achieve the necessary improvement. For the NIST experiment, the light guide has three vacuum gaps to transmit the light from the cryogenic environment to the room-temperature environment: one at the transition from 250 mK to 4 K, one at the transition from 4 K to 77 K, and a final one at the transition from 77 K to 300 K. These gaps were a major contributor to the light loss: each gap caused a loss of about 20% [5]. By operating the PMTs at 4 K, we will be able to eliminate two of the gaps, improving the light collection by a factor 1.6.

It has been demonstrated that PMTs can be operated successfully at 27 K in liquid neon [6]. In order for the PMTs to be operated at cryogenic temperatures, the photocathode needs to have a flash of metal such as platinum so that the photocathode does not lose its electrical conductivity at cryogenic temperatures. Tests are planned to see if PMTs can be operated at 4 K. R7725, a high-gain, low-noise PMT with an effective area of 2" from

Hamamatsu Photonics K.K. is the first candidate PMT. The manufacturer has experience modifying this model for cryogenic use.

Another factor-of-two improvement is expected to come from the way the light guide is coupled to the measurement cells. In the NIST Neutron Lifetime Experiment, the measurement cell was a cylinder of 3.8 cm diam with 3.1 mm wall thickness, and a 3.8 cm solid light pipe coupled to the back end of the measurement cell cylinder. We expect to improve on the collection of the light emitted from dTPB by coupling additional light guides to the measurement cells on the front end of the measurement cells or on the sidewalls, thereby increasing the area to collect the light from. A preliminary study shows that by having additional light guides coupled to the front end of the measurement cells or to the sidewalls of the measurement cells, a gain of a factor two can be obtained. When the light guides are coupled to the front end of the measurement cell or to the sidewalls, the guides need to be bent so that the light is guided to the end cap where the light is transported through the gap to the 4 K light guides. In order to minimize the loss due to the bend, we plan to use bundles of thin (~3 mm diam) acrylic fibers (See Figure VIII-3). A detailed study including Monte Carlo simulations is under way.

This scenario has a few added advantages. First, because the PMTs are at 4 K instead of 300 K, the head load will be reduced. Also, using bundles of thin acrylic fibers makes it easer to cool the light guides with the 300 mK bath than if they were made of bulk acrylic because of the larger surface-to-volume ratio.
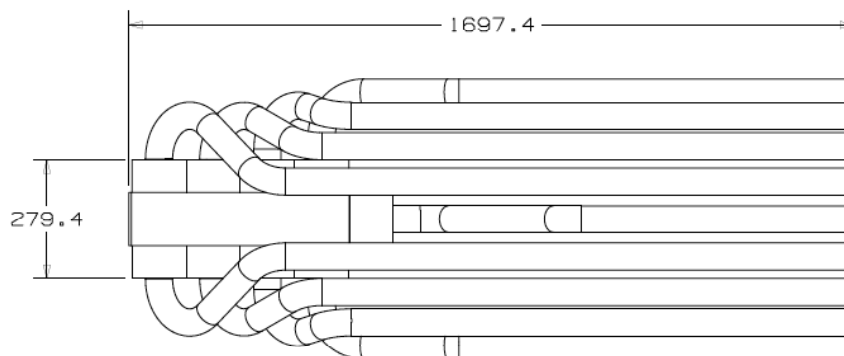

Fig. VIII-3.   Schematic of the light system. The light guides are made of bundles of thin acrylic fiber. The PMTs are placed in the 4 K environment.

C. Electric Field Configuration and Generation

The static electric field in the EDM experiment should be as strong as possible, consistent with stable operation, to give the largest possible shift in the precession frequency. The target field for minimal performance of the experiment is 25 kV/cm [7]. To prevent spurious EDM signals generated by stray magnetic fields from leakage currents, the electric field should remain as stable as possible. The target stability for minimal performance is 1% over the course of a measurement cycle, corresponding to a leakage current of 1 nA [8]. To prevent systematic effects associated with motional magnetic fields, the electric field must be parallel to the static magnetic field and maintain its magnitude on reversal. For minimal performance, the target angle between the electric and magnetic fields is 50 mrad [7], and the reversal asymmetry limit is about 5% [8,9].

In the current reference design for the EDM CDS, a single HV electrode is flanked by two parallel ground plates that provide equal and opposite electric fields over the two cell volumes (see Figure VIII-2). The HV electrode measures 30 cm × 77 cm and is 10 cm thick. The ground electrodes measure 25 cm × 77 cm and are 5 cm thick. The spacing between the HV and

either ground electrode is 7.6 cm, so the voltage requirement for the minimum target field is 190 kV. Commercially available feedthroughs suitable for the experiment are rated to 100 kV, so while it might be practical to attempt bringing this voltage into the apparatus from an external source, it is not straightforward for any higher voltage. Therefore, the experiment uses an amplification mechanism in which a variable capacitor is connected in parallel with the capacitors formed by the cell electrodes. A small (50 kV) initial potential from an external source is used to charge the HV electrodes when the variable capacitance is large. The capacitors are then isolated and the voltage is stepped up by reducing the variable capacitance. The variable capacitance is designed to range from 1 to 1000 pF and is suitable for attaining an amplification factor of 7 [8].

To reduce contamination of the scintillation and SQUID signals, the electrodes must be composed of materials chosen to avoid activation and thermal noise. Superconducting materials must also be avoided to preserve the uniform magnetic field environment. While the final choice of materials has yet to be decided, the electrodes in the current reference design are fabricated from a graphite-coated dielectric such as acrylic.

The dimensions of the fixed electrodes were chosen after a series of electric-field simulation studies [10]. The simulation used a rectangular acrylic cell with walls recessed into the HV and ground electrodes. While the final dimensions of the electrodes are expected to be further optimized, the dimensions listed above resulted in a maximum variation in the electric field of 1% over the cell volume in the simulation.

In the CDS, the fixed ground electrodes flanking the cells are supported by coated spacers anchored to the return electrode cylinder. The HV electrode between the cells is connected to the HV electrode of the gain capacitor by a cylindrical conductor of the same material (see Figures VIII-1 and VIII-2). The radius of the connecting line is matched to the radius of curvature of the HV cell electrode edge to keep the surface electric fields comparable to the field across the cells. The entire HV electrode assembly (cell and gain capacitor electrodes plus connecting line) is supported by ceramic insulators attached to the gain capacitor and anchored to the vertical spacer in the return electrode cylinder. The initial voltage on the HV electrodes is established by bringing them in contact with a small, moveable charger electrode connected to an external power supply. The positions of the charger and the moveable ground electrode of the gain capacitor are adjusted by rods exiting the CDS via standard bearings and welded bellows mounted to the end cap (see Figures VIII-1 and VIII-2). The charger is connected to the external supply with a conducting wire (which can be a thin-walled tube for low thermal conductivity) leading out of the CDS by way of a standard ceramic feedthrough mounted in the bellows cap, and then out of the EDM cryostat via a similar feedthrough.

During the operation of the experiment, the gain capacitor is charged by putting the charger electrode in contact with the HV electrodes and applying a potential of a few tens of kV. The charger is then retracted about 10 cm, leaving the HV electrodes isolated. The capacitance of a single pair of electrodes (HV plus one ground) flanking the cells is about 55 pF, as is that of the connecting line. During charging, the ground electrode of the gain capacitor is within close proximity (~1 mm) of the HV electrodes and the gain capacitance is about 1000 pF, so that the total capacitance of the system is about 1165 pF. To ramp the electric field, the ground electrode of the gain capacitor is moved out about 10 cm (over about 10 s), reducing its capacitance to a few pF. In this configuration, the capacitance of the system is about 170 pF, for a net voltage gain factor of 7. The ground electrode of the gain capacitor can be moved back in close proximity to the HV electrodes to reduce the field when necessary, and the plates can be discharged through the charger electrode.

The R&D program for the HV system involved the construction of a chargeable gain-capacitor prototype. The voltage-amplification results are described in Chapter III. Other results from the HV test apparatus show that the small commercial feedthroughs used to bring in the initial voltage exceeded their maximum rating in air (40 kV) by at least 25% when immersed in LHe and should be sufficient for the experiment. The proposed mechanisms for control of the moveable electrodes in the variable capacitor (including the welded bellows well removed from the central apparatus, and standard bearings encased in plastic lubricated solely with the LHe itself) performed as designed.

The degraded performance of the system at the lowest temperatures attained, as described in Chapter III (Figure III-4), raises concern about the voltages achievable at the operating temperature of 0.5 K. It is likely that some of the resistance against breakdown observed near 4 K can be recovered by pressurizing the superfluid helium in the EDM experiment; however, pressurization introduces a variety of engineering challenges discussed in Chapter VII.

D. Electric Field Monitoring System

The Kerr HV monitor is a system for monitoring the electric field inside the measurement cells and inside the gain capacitor. As described in Chapter III, the Kerr effect may be used to determine the electric field from the polarization ellipticity induced in the initially linearly polarized laser beam by the LHe. The Kerr relationship is expressed in Equation III.3.

The measurement setup for the nEDM experiment is shown in Figure VIII-4. The polarimeter consists of a diode laser light source, a polarizer, followed by a photo-elastic modulator (PEM), and an analyzer. The PEM modulation axis is parallel to the dark axis of the polarizer, and the analyzer is nearly crossed with the polarizer, the decrossing angle is chosen to optimize signal-to-noise ratio. The signal detected by the photodiode contains harmonics of the modulator frequency, measured by the lock-in amplifier, with the first harmonic proportional to
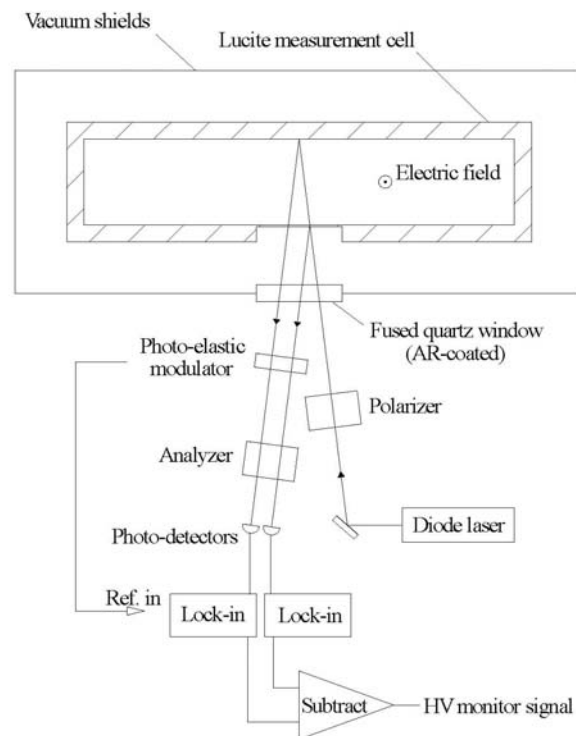

Fig. VIII-4.   A schematic Kerr HV monitor setup.

polarization ellipticity. This polarimeter setup is identical to that used in [11], where its operation is described in more detail. As demonstrated in [12], the sensitivity of this polarimeter is
10^{-7} rad/√Hz.

In addition to the Kerr-effect-induced ellipticity signal, the polarimeter also sees a much larger ellipticity contribution due to window and Lucite-cell-wall birefringence. The window birefringence, for example, can create polarization ellipticity on the order of 0.1 rad. To eliminate the noise and drift due to this stray birefringence, a differential measurement is set up in Figure VIII-4. The laser beam splits into two at the inner wall of the measurement cell (for the gain capacitor setup the split occurs at the inner face of the innermost window). The beam that returns straight back has not traveled inside the measurement cell, and thus its polarization ellipticity is due only to stray window and Lucite birefringence. The beam that is reflected off the back wall of the measurement cell, however, has made a double pass through the cell, and its polarization ellipticity is the Kerr-effect-induced signal on top of the stray window and Lucite birefringence. We obtain the Kerr-effect-induced ellipticity by subtracting the polarimeter signals from the two beams. The goal is to suppress the stray window and Lucite—induced ellipticity to below the 10^{-6} rad level.

Given the electric field inside the measurement cells of E = 50 kV/cm, the laser light wavelength of λ = 632 nm, and the path length L = 20 cm (double pass through the cell), the expected polarization ellipticity signal is $\varepsilon = 4 \times 10^{-5}$ rad. With stray ellipticity suppressed to 10^{-6} rad, the Kerr HV monitor measures electric field with 1% accuracy.

Integration of the Kerr-effect-based electric-field monitoring system into the EDM apparatus raises some issues. The most serious concern is getting the laser light in and out of the apparatus. This could be achieved either with a polarization-preserving optical fiber, or with a set of window ports, combined with mirrors inside the experimental volume to guide the light to the cells and the gain capacitor. Also, the thin window must be compatible with pressurization of the LHe and must not distort the electric field.

The PMT's for the detection of the LHe scintillation will be turned off during the operation of the Kerr HV monitor system.

E. SQUIDs

The signal-to-noise requirements for various aspects of the full SQUID system are discussed in Section V.H of the preproposal. The SQUIDs can be used to observe directly the ^{3}He precession by measuring the bulk sample magnetization as a function of time. Such direct observation serves as the principal measurement technique, pending solution of a number of difficult technical problems associated with the originally proposed dressed-spin technique.

Further analysis shows that the expected magnetic-induction signal for a SQUID pickup loop at the location given in Figure V.F.1 of the preproposal is about 1/10 of the ^{3}He sample magnetization, so $B_P = 2 \times 10^{-11}$ G. The calculation in V.H.1.B implies that the SQUID pickup loop area must be 10 cm^2, assuming the sensitivity of a Conductus-1020 SQUID. A recent test of a Quantum Design SQUID demonstrates a factor of at least a factor-of-two lower noise. However, a working design with a 10 cm^2 area ensures adequate signal to noise.

Also, given the small size, these measurements are to be performed with pickup coils in a gradiometer configuration, which is possible because the sample magnetization field falls off roughly as the inverse of the distance from the cell. This arrangement allows discrimination of shifts in the background applied magnetic field from the magnetization signals.

At present, we are planning for eight SQUID channels, four per cell, two of which will monitor the initial ^{3}He magnetization as the cells are filled with polarized ^{3}He (sensitive along

the applied field), with the other two arranged to pick up the precessing magnetization signal, as shown in Figure V.F.1 of the preproposal.

The SQUIDs themselves will be located outside the sensitive magnetically shielded region, with signals brought out with superconducting niobium wire twisted pairs inside of superconducting lead tubing. Inside the sensitive region, the twisted niobium pairs will be shielded by a low-electrical-conductivity material, such as phosphor bronze, and the superconducting pickup loops will be contained in phosphor bronze (or similar) conducting boxes. The low electrical conductivity material will allow the relatively low-frequency magnetic fields of interest to penetrate to the pickup loops, but shield the high-frequency electromagnetic pulse energy due to sparks or microdischarges from the sensitive SQUIDs and their associated electronics. In order to minimize Johnson noise, we will need to eliminate any material with good conductivity from the region around the measurement cells.

F. Neutron Shielding and Beam Stop

The primary source of background is expected to arise from the interaction of neutrons with materials in the apparatus. During the filling phase of the experiment, large numbers (10^{11}–10^{12}) of neutrons will be introduced into the apparatus to produce the UCN. These neutrons will interact with various materials in addition to the ^{4}He. If such an interaction results in the storage of energy in a metastable state (such as a radioactive isotope or a color center), then the release of that energy can result in a background event once the beam is off.

As many as possible of these unwanted neutrons are to be absorbed by placing neutron shielding at appropriate locations to be determined by Monte Carlo studies of the neutron-beam transport and scattering inside the apparatus. Both the beam stop and the neutron shielding need to be made of material that absorbs neutrons but does not get activated itself. Following the experience of the NIST Neutron Lifetime Experiment, we plan to use boron nitride in a light-tight package.

References

1. D.N. McKinsey et al., *Phys. Rev. A* **67**, 062716 (2003).
2. C.R. Brome et al., *Phys. Rev. C* **63**, 055502 (2001).
3. S.K. Lamoreaux, ILL report 88LA01T (1988).
4. D.N. McKinsey et al., *Nucl. Instrum. Methods Phys. Res. B* **132**, 351 (1997).
5. S. Williamson, "Simulation of EDM Lightguides using GuideIt," presented to the EDM Collaboration, Urbana, IL, December 2004.
6. D.N. McKinsey, "PMT Test at LNe temperature," presented to the EDM collaboration, Raleigh, NC, March 2, 2006.
7. M. Cooper, "EDM Specifications," presented to The EDM Collaboration, Oak Ridge, TN May 25, 2006 [http://www.phy.ornl.gov/nuclear/neutrons/May2006EDMCollabMeeting/CollabMeetingAgenda.htm].
8. EDM Collaboration, "A New Search for the Neutron Electric Dipole Moment," Los Alamos Report 2002, LA-UR-02-2331, 1–179.
9. .   S.K. Lamoreaux, *Phys. Rev. A* **53**(6), R3705–R3708 (1996).
10. R. Mischke, "Report on ANSYS Model Results," (Parts 1 & 2), February–March 2002, [http://p25ext.lanl.gov/%7Emischke/edm/edm_ppt.html].
11. A.O. Sushkov et al., *Phys. Rev. Lett.* **93**, 153003 (2004).
12. J.C. Long, et al., [http://arxiv.org/abs/physics/0603231].

IX. Slow Controls, Data Acquisition, Simulations, and Data Analysis (WBS 1.8)

The purpose of this group of work packages is to develop slow-control and data-acquisition (DAQ) systems for the EDM apparatus, and to develop software to simulate as many features of the EDM experiment as feasible.

EPICS (Experimental Physics and Industrial Controls System) is the proposed control system standard. EPICS software is now universally adopted for use at the major accelerator facilities (including the APS and the SNS). It supports many off-the-shelf commercial devices in a distributed-network environment, and is freely available to interested users. It also supports remote operation and control of systems, a valuable feature as the experiment moves from commissioning to production mode.

The DAQ system will be built around coincidence-triggered wave-form digitizers, capturing the prompt and after-pulse signals associated with neutron/^{3}He capture events as well as the SQUID signal. Many terabytes of data can be expected to be accumulated over the lifetime of the experiment, and techniques for rapidly evaluating the data will need to be developed, along with reliable archival storage systems.

Simulation of all aspects of the experiment will be important to understanding the ultimate sensitivity of the apparatus, from neutron transport into the measurement cells, to optimization of the measurement cycle, to light production and efficient transport through light guides to the PMTs. Of particular interest, and unique to the EDM experiment, are modeling of the neutron and ^{3}He trajectories and their spin interactions in the magnetic and electric fields of the apparatus, and simulation of background suppression via detection of after-pulsing.

A. Slow Controls (WBS 1.8.1)

The complexity of the EDM apparatus indicates a need for extensive and redundant diagnostic monitoring. The measurement sequence—from neutron fill to application of *E* and *B* fields to ^{3}He purge—is also very complicated and must be reliably controlled.

We estimate up to of order 1000 parameters and status values will need to be monitored, controlled, and regularly archived during the course of the experiment. An alarm system for parameters away from their bounds will be required. In addition to monitoring, the EPICS system will control the state of the apparatus by sending signals to change valve positions, ramp voltages, etc. The slow controls will implement the measurement cycle.

Five individual subsystems will be built and tested at different sites, and thus five independent control systems of varying complexity are envisaged: cryogenics, magnets, ^{3}He, the central detector insert (includes the HV), and the neutron splitter/polarizer (includes the UCN flux monitors). As a distributed-control environment, EPICS is ideally suited for our application because the individual subsystem developers can proceed independently up until the integration step at final assembly and testing at Oak Ridge.

The basic architecture of each system will consist of an operator interface (OPI) consisting of a Linux computer, or equivalent, and display monitors connected over a network to an input-output controller (IOC) made up either of VME crate(s) with commercially available modules running under VxWorks, or an equivalent real-time operating system and hardware complement. Extensive libraries of device drivers are maintained at the Argonne APS EPICS site, and to facilitate the integration step, subsystem managers will be asked, where possible, to purchase hardware compatible with these existing device drivers and software. A central database of process variable (PV) definitions and equivalent control parameter records, will be developed as the construction project progresses, and communicated to all subsystem developers.

A rough estimate (2 bytes/parameter, 1000 parameters/s) indicates of order 0.06 terabytes

of control information is stored per year, a manageable amount. The data will be archived locally and off-site. We will utilize SNS-developed software and expertise for accessing and organizing the information.

B. Data Acquisition (WBS 1.8.2)

The EDM signal consists of light pulses associated with the capture of a polarized neutron on polarized ^{3}He as seen by an array of PMTs. Event rates are expected to be of order 1 kHz. Background events associated with neutron β decay, higher-energy β decay (i.e., from neutron-activated ^{28}Al), and Compton-scattered γ rays will have a similar rate, and the DAQ system needs to be able to record the information needed to identify these two types of events from the EDM signal.

An attractive method for discriminating between good events and background events on the basis of after-pulse characteristics has been discussed in the literature and elsewhere in this CDR. One expects the after-pulses to be reflected in the distribution of the number of single-photoelectron events that are detected during a short (few µs) time window following the initial scintillation pulse when plotted as a function of the total area of the main scintillation pulse.

The DAQ will be triggered by prompt coincidence signals from the PMT array, and will consist of 1 GHz 8-bit wave-form digitizers to capture the prompt and after-pulse signals for of order a microsecond after the trigger event. Double buffering will be implemented to minimize readout dead-time. The data will be spooled to disc storage and archived locally and off site on a RAID array and on a terabyte tape-storage system. Because reading back and analyzing wave forms is an intrinsically slow process, a duplicate DAQ system will also be implemented, using fast discriminators and scalers to provide rapid diagnostic information on the performance of the detection system.

The EDM scintillation signal as a function of time is a measure of the beat frequency between the neutron and ^{3}He precession rates. As noted earlier, the signature for a nEDM is a shift in this beat frequency when an electric field is applied, with no corresponding change in the ^{3}He precession frequency. The DAQ must therefore also record a time-stamped ^{3}He magnetization signal from the vertical and horizontal SQUID pickup coils. The ^{3}He precession rate will be of order 10 Hz. Reading the SQUID signals at 1 KHz with a 10-bit sampling ADC, will therefore yield sufficient samples. While this task could be part of the slow-control system, it appears more logical to include it with the DAQ work package, given the close real-time connection between the ^{3}He signals and the neutron-scintillation signals.

The cells have a combined area of 700 cm^2 leading to a cosmic-ray rate in the detector volume of about 12 Hz. While low compared to the true event rate, it will be better to veto the DAQ following a muon passage, particularly in the early stage of testing where the full true event rate is not yet realized. A veto system close to the cells is not feasible, but a large-area (multi-m^2) plastic-scintillator cosmic-ray suppression system can be implemented external to the whole apparatus, preferably below (for mounting simplicity), but also above if necessary. Neutrons are produced in hadronic showers, but these are typically only 1% of the total events. Even accounting for the larger volume of the apparatus, these would give a negligible contribution to the overall background.

Assuming 10 kb of data per event, an event rate of 1 kHz, and a 1000 s measurement cycle, the amount of data will be of order 10 Gb/cycle. Over the course of a year at 30% live time, this would amount to 100 Tb of data. This is a substantial amount, indicating a clear need for a data-compaction preprocessing-analysis step once the experiment moves into production mode.

C. Simulation and Data Analysis (WBS 1.8.3 and 1.8.4)

Simulations have been or will be initiated to model all aspects of the experiment: beam transport into the measurement cell; ^{3}He injection and removal; experiment cycle optimization; magnetic- and electric-field configurations; neutron-cell dynamics (trajectories, spins, and interactions between n and ^{3}He); light production and propagation; and neutron-capture-event wave-form digitization. Results from this work are discussed in more detail in earlier sections. Where possible, simulations will be carried out using GEANT4, particularly for neutron and γ-ray background calculations for the fully engineered apparatus. The ray-tracing simulation code GuideIt is being used to design the light-collection system and Monte Carlo codes have been used to model neutron transport from the SNS moderator to the end of the 8.9 A beamline. Some of the other more specialized features of the EDM experiment which are not compatible with GEANT4 (modeling UCN and ^{3}He cell dynamics, optimizing the measurement cycle, simulating event identification from main-pulse and after-pulse events) will also be modeled separately.

Substantial work on Monte Carlo simulation of the neutron-beam transport has already been carried out by the FNPB project group. The original baseline design of 33 m, $m = 3.5$ straight guide with a 12 cm 14 cm cross section, has been superseded by a ballistic guide consisting of a 7 m curved diverging horn plus a 19 m straight section plus a 7 m curved converging horn. The new design gives a 75% increase in the transmitted neutron flux. Initial proof-of-principle modeling of neutron transport through the remaining polarizing supermirror has been performed, but detailed calculations remains to be carried out on this geometry and to model the transport into the measurement cells. GEANT4 simulations of the neutron and γ-ray backgrounds due to scattered beam are also required.

A detailed simulation of the magnetic-field configuration is critical for addressing two issues: depolarization of neutrons and ^{3}He due to field gradients, and elimination of a false EDM signal for neutrons and ^{3}He due to the geometric phase systematic. In-house codes and the vector field, 3-D finite element code TOSCA have been used to generate precise magnetic-field models of EDM coil configurations, and show good agreement. Extensive work on analytic models of the geometric phase effect have been developed and applied to the expected conditions in the EDM apparatus. Results are discussed in previous sections. A full-scale Monte Carlo simulation of the geometric phase build up will be necessary to fully understand the ultimate limits on the sensitivity of the apparatus. The simulation will follow the neutron and ^{3}He spin dynamics in the cell, along with their trajectories, and will model electric- and magnetic-field effects in the presence or absence of a true nEDM. Simulations of the absorption rate will provide input to the simulations of the detection system and the analysis software. As mentioned above, development of a data-compaction protocol will have a high priority as the experiment moves from commissioning to longer term data taking.

Efficient visible-light production and transport are essential for achieving good signal-to-background ratios. GuideIt is based on an earlier CERN Fortran code and has capabilities for following light reflections and refractions at boundaries, and specular reflections from mirrored or metallic surfaces. Modifications to the code have allowed for simulation of the energy down-conversion process from the dTPB coating of the measurement cell. Preliminary simulations using standard light guides attached to the ends of the cell indicated about 12 photo-electrons per prompt event, which is suboptimal for PID. Fiber-optic bundles attached to the sides, in addition to the edges, could potentially yield a higher number of photo-electrons/event; detailed simulations will be required to confirm that these geometries are practical in the full apparatus.

The measurement sequence has a number of steps and optimizing the counting efficiency has been considered under a number of different scenarios. Under one scenario considered, a

measurement sequence involving 1000 s of live DAQ takes 2325 s, including loading and emptying ^{3}He, loading and emptying the UCN, ramping the electric field up and down, and allowing for settling times of the various valves and shutters. Simulation efforts will continue to explore ways of maximizing the live time in order to utilize the neutron beam time as effectively as possible.

Given the large number of tasks in the DAQ, the wide variety of simulations being undertaken, and the length of time over which the experiment will be carried out, standards for computer operating systems, code management, and programming documentation will need to be implemented. The expertise of the PHENIX and STAR collaborations at RHIC will be exploited; both groups have extensive experience in this area and have developed documentation and standards that may be appropriate to the EDM project.

X.   Infrastructure (WBS 1.8)

This section of the CDR covers areas of the EDM experiment having to deal with support systems; mechanical platforms, the electrical plant, the required plumbing—water, air, cryogenic supply lines, the mechanical supports for different elements of the experiment, assembly jigs, and the counting house. Because the infrastructure for the experiment relies on input from the various subsystems, working closely with the other subsystem managers as well as the Chief Engineer and SNS personnel is a necessity. These interactions will keep current requirements up to date.

Mechanical Platforms

Mechanical platforms will be needed for EDM personnel to have access to the experimental apparatus. As can be seen in the overall picture of the detector system, its size precludes safe access to various components without special platforms being fabricated. Some components, like the ABS, are located 6 m in the air. Using 3-D CAD capabilities that include a very detailed model of both the experimental apparatus and the proposed building at the SNS in which it will be located, mechanical platforms can be developed to allow access to all the required areas of the experiment as needed. These platform models can be translated into other CAD platforms and used to obtain estimates from vendors for their fabrication. One proposed vendor is Bustin Industrial. The large PHENIX experiment at Brookhaven National Laboratory has made exclusive use of this vendor for the fabrication and engineering of several access-platform assemblies. These were designed to allow scientists and technicians easy access to almost every aspect of this very complex collider experiment. It is important that a chosen vendor has professional engineering capabilities as well as familiarity with all OSHA regulations concerning the design of platforms/scaffolding. Bustin Industrial meets these qualifications. The final design for all mechanical platforms must be approved by the EDM Chief Engineer. These platforms will be incorporated into the overall EDM experiment CAD model.

Electrical Plant

The SNS facility will be providing the EDM experiment with a new building, attached to the target hall, in which the experiment will be located. An agreed-upon quantity of 3-phase power will be provided to the EDM experimental team by the SNS, it is currently estimated to be 250 kW. A list of some of the larger items that are a part of this experiment and their power requirements, are listed in Table X-1. Information will be provided to the SNS physical-plant engineering team, with details of where the main distribution panels and transformers should be located. Once the panels are installed, the EDM engineering team will create a schematic for the distribution of power inside the hall along with specific interconnect requirements to equipment on the floor. The costs for the distribution of power inside the EDM facility is the responsibility of the EDM experiment.

In order to have the best-quality detector signals, planning for proper power distribution is important. Separation of clean and dirty power, as well as planned grounding and shielding, will be needed for this experiment to be successful. The installation of electrical services will be coordinated by the EDM Chief Engineer and the SNS physical plant engineering group. The work may either be performed by SNS crafts or contracted to outside vendors. During the assembly phase at NCSU, every attempt will be made to duplicate the conditions at the SNS so that the electrical plant can be reused. This would include electrical disconnects on components, long flexible cords with plugs, as examples.

Table X-1. Major Power Requirements in the UCN Guide Hall at the SNS

Item	Power (kW)
DRS 3000 dilution-refrigeration system	
Edwards EH 4200	7.5
Edwards EH 1200	3.0
Edwards EH 500	1.5
Edwards EH IL 70 dry pump (2×)	2.2
Gas Carts (2X)	10.0
Linde 1440 helium-liquefier system	
RSS compressor	40.0
Liquefier	5.0
Auxiliary power	5.0
^{3}He polarized source	
RDK 415D cold head	9.0
Varian V2000 turbo pump	2.0
Varian V1000 turbo pump (2×)	3.0
Edwards XDS 10 scroll pump (3×)	3.0
Pfeiffer Unidry 050 pump	4.0
Gas cart and instrumentation	
Miscellaneous	
Leak detector	2.0
High voltage power supply	2.0
Universal pumping system for roughing cryostat before precool, Edwards IH600	15.0
Varian V1000 turbo or equivalent	2.0
EDM beamline pumping	
Edwards scroll pump (2×)	2.0
CTI Cryotorr (2x)	2.0
Other	30.0
Total	**175**

Plumbing

The EDM experiment will require cooling water at 24 °C and 200 Lpm, for an estimated heat load of 250 kW. Some of the major heat sources have been listed in Table X-1. The helium liquefier and its compressor, large vacuum blowers, etc. The SNS facility will supply the cooling water from their system to the UCN hall. The costs for the engineering design, layout, parts, and installation are part of the EDM experimental costs. The layout will be developed in a CAD model that will be integrated into the experimental model by the Chief Engineer. The installation will either be performed by SNS crafts personnel or contracted to outside vendors. Approval of work will be handled by the SNS physical plant engineering group. Additional elements of the plumbing system will include compressed air, provided by SNS, and pluming lines run outside the building to transfer helium gas from a tube trailer, and liquid nitrogen from a fixed dewar.

The helium gas line from the tube trailer should be stainless steel and certified for 500 psi. Cryogenic lines will be needed inside the hall running from the helium liquefier to the large cryostat, as well as cold-gas return line. These lines will be special vacuum jacketed

cryogenic transfer lines, to limit cryogen loss during transfer. A vacuum-jacketed line to supply liquid nitrogen will be needed to run from the external nitrogen dewar to the location of the helium liquefier in the hall. Again, the infrastructure used during the assembly at NCSU will be done to make the parts reusable at the SNS, including these cryogenic transfer lines.

Mechanical Support

Mechanical supports for various parts of the EDM experiment are a part of the infrastructure. Some of these include the main support for the upper and target cryostats, the ABS, the rail system for the installation and removal of the inner measurement-cell region, support for the magnetic shield before installation—to name just a few. There will also be a number of special jigs and fixtures to aid with the assembly, testing, installation, and maintenance of various components, some of these include; assembly of the ^{3}He source sled, jig to interface the ^{3}He source with upper cryostat, alignment jig for the DR insert and its maintenance, jigs and fixtures for the assembly of the HV system in the target cryostat, fixtures for the installation and removal of the $\cos\theta$ coil. These items are a few that have been identified at this time. These fixtures and jigs will be requested from the subsystem managers, will be designed using a CAD program, and brought into the EDM model by the Chief Engineer, who will approve final designs before fabrication.

A proposed counting house is suggested to be installed inside the UCN experimental hall at a location off the floor, along the wall that is common to the SNS target hall. Access to the counting house may be made from the experimental hall floor via a stairway or from the mezzanine walkway in the SNS target hall; see Figure X-1. The counting-house dimensions will be 8' w × 9' h × 20' l. A quotation for a modular structure this size and suitable support structure (needed because the planned location is 5 m off the floor) has been obtained from General Electric Modular. It is proposed that the counting house has access from both ends, both to the floor and the adjoining SNS target building.
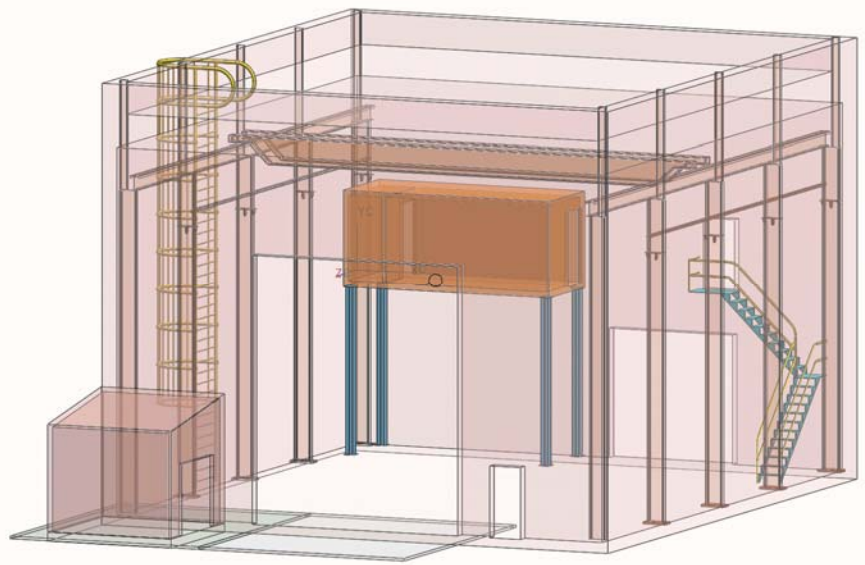

Fig. X-1.   EDM experimental building indicating Counting House location.

XI. Assembly and Commissioning (WBS 1.9)

The scope of this work package is to bring together the tested components from the individual work packages and integrate them to form a complete apparatus and to demonstrate completion of the CD-4 delivery specifications. Numerous integration plans were considered, and the one chosen attempts to minimize the number of cool-down cycles, the movement of equipment, and the total duration of the project. This plan is based on the assumption that one senior cryogenic physicist will be hired by ORNL, and one to two postdoctoral fellows will be hired through a university to oversee this effort.

Subsystem Integration

The individual subsystems are being constructed at various sites across the country and must be integrated together to form the experimental apparatus. The apparatus is unique in that a large fraction of the subsystems operate at low temperature and therefore reside inside of the cryogenic vessel. This integration requires the expertise of an on-site cryogenic physicist in order to oversee the thermal integration with the refrigeration system and to balance cryogen flow rates as the heat loads change. Because of the means by which the cryogenic subsystems are connected, the failure of one subsystem—for instance, a vacuum leak in the cryogenic vessel (CV)—can preclude testing the remainder of the systems. Extreme care and expertise are required at all times during the integration process. Quality control needs to exceed the standards usually applied in projects within the community. The remaining subsystems, on the other hand, are less coupled to the vessel and thus have reduced overall integration concerns. Beneficial occupancy of the FNPB is well matched to the nEDM construction schedule.

Cryogenic Vessel Integration

The CV will be constructed and tested at ORNL as part of the cryogenics work package. Upon completion of this subsystem, integration of components from three other major work packages will begin. These packages include the measurement-cell insert system (including the HV system), the magnetic-field coils and cryogenic magnetic shields, and the ^{3}He injection/transport/purification system. In addition to all of the complexities associated with the construction of the individual subsystems, these pieces must operate by generating a minimal amount of heat.

Based on prior experience with cooling smaller cryostats and discussions with individuals at institutions such as Louisiana State University who have built and operated cryostats of a similar size as the nEDM system, we estimate that it will take six to eight weeks to assemble, cool, test, and then warm the system back to room temperature. All subsystems that reside in the cryostat must therefore be carefully designed and fully vetted before integration to minimize the number of cool-downs of the entire system during integration.

Each subsystem is also sufficiently complicated that they must be integrated independently into the CV. This choice is based on experience in assembling and cooling cryogenic apparatuses. During each test cool-down cycle, detailed measurements of the temperatures and associated heat loads from each component installed must be performed. The components will need final testing, and interactions between subsystems will need to be characterized and optimized as well. If too many items are integrated at once, one would not be able to efficiently perform this optimization.

The first package to be integrated into the CV is the measurement-cell insert and HV package. This system primarily resides inside the 1200 L helium volume, and as such, operates at mK temperatures. A significant number of mechanical connections between this low-temperature region and room temperature are required; movement actuators, temperature monitoring, the

light-collection system, etc. Heat loads from the insert must be characterized, minimized, and then balanced with the refrigeration system. The measurement cells require final calibration using radioactive sources and the HV system must be fully vetted.

The magnetic-field coil system and internal magnetic shields comprise the second work package to be integrated. The 4 K shields that surround the 1200 L LHe volume cool this system. Uniformity tests of the fields and gradients must be performed in addition to quantifying the associated heat loads from these coils and shields through resistance heating, conduction, and eddy-current heating. Cooling tests of the cryogenic ferromagnetic shields must be performed to optimize the cooling from one end and to minimize stresses during cool-downs.

The third work package is the ^{3}He insertion, transport, and removal system. Again, this system operates at mK temperatures and has extensive integration requirements. The polarized ^{3}He ABS must be attached to the cryogenic vessel with its beam terminating in the collection volume. The transition between this room-temperature source and the low-temperature collection volume must be carefully designed to minimize heat loads. The operation and performance of the valves and associated plumbing connecting the ^{3}He collection volume, measurement cells, and ^{3}He removal system must be demonstrated. In addition, the ^{3}He removal system must be tested as well.

Three cool-downs are budgeted for the coil package and shields work package and four for the measurement cells and HV insert work package. Upon completion of the CD-4 acceptance requirements, we anticipate that an additional four cool-downs will be needed to optimize the ^{3}He systems and an additional four to six cool-downs to optimize the complete system. Overall, we are estimating that a total of 14–16 cool-downs are required to complete construction and optimize operations. As one would expect, the integration defines the latter stages of the project and is thus on the critical path.

Integration of Other Subsystems at ORNL

Alongside the integration of the above work packages into the CV, numerous activities will take place in parallel both at ORNL and offsite. These shields will be assembled and tested offsite to verify their performance. These shields will then remain off-site and serve as a low-field testing facility until they are ready to be assembled around the cryogenic vessel. Our present design allows for the shields to be installed in parallel with the final testing stages of the apparatus; the shields will be designed such that they can be rolled under the apparatus. Because the shields are fragile and that one must remove them (or a significant portion) before opening the apparatus, is both risky and time prohibitive to have the shields installed during the testing phases. We anticipate installing the shields once the ^{3}He system testing is complete.

The neutron beam line work package will be delivered and installed by the vendor. Final testing of these components will be performed by measuring both the flux and polarization of the neutron beam.

A small facility to house the user interface to the DAQ will be installed in the target room. In addition, the assembly of the infrastructure required to accept the shields and CV in the external building will occur.

The integration and testing of the DAQ for the entire system will be performed during the assembly and commissioning tests.

Personnel

The required personnel to perform the assembly and commissioning at ORNL is one full-time senior cryogenics expert, one or two postdoctoral fellows with cryogenic expertise, half-time from S. Penttilä, two full-time technicians, and expertise from elsewhere in the collaboration. Funding is included in the project budget for the technicians. Negotiations

amongst LANL, ORNL, and DOE NP are underway regarding the cryogenics expert. Funding for the other staff is assumed to come from the existing operations budgets of the collaborating institutions. Cryogenic expertise from around the collaboration, especially from NCSU, will play a significant but part-time role at ORNL in the assembly and commissioning process.